InGaAs/InAlAs single photon avalanche diodes at 1550 nm and X-ray detectors using III-V semiconductor materials

Xiao Meng

The University Of Sheffield.

A thesis submitted for the degree of Doctor of Philosophy

Department of Electronic and Electrical Engineering
The University of Sheffield

August 2015

Acknowledgement

Firstly, I would like to express my deepest gratitude to my supervisors, Dr. Jo Shien Ng and Prof. Chee Hing Tan, for giving me an opportunity to pursue a PhD degree and their invaluable guidance on this work. I really appreciate for their constant support and encouragement, particularly during difficult times of my research. I also would like to thank Prof. John David for his expert comments and suggestions on my work. My gratitude also extended to Dr. Shiyong Zhang for growing high quality wafers.

I am grateful to Dr. John Lees from University of Leicester and Dr. Anna Barnett from University of Sussex for providing useful experimental data and giving critical comments on my publications from this work. I would like to acknowledge Prof. Alberto Tosi and his group members for the cross-measurement results on parts of my work.

I sincerely thank Simon Dimler and Dr. Rajiv Gomes who shared their insights on single photon avalanche diodes and semiconductor X-ray detectors, respectively, during the first year of my PhD. Thanks also go to other impact ionisation group members, past and present, Dr. Ian Sandall, Dr. Shiyu Xie, Dr. Perter Vines, Dr. Pin Jern Ker, Dr. Jingjing Xie, Dr. Rajiv Gomes, Dr. James Green, Dr. Jennifer Ong, Dr. Siewli Tan, Dr. Rahman Mohmad, Dr. Matthew Hobbs, Dr. Xinxin Zhou, Akeel Auckloo, Jeng Shiuh Cheong, Benjamin White, Zhize Zhou, Liang Qiao.

Finally, I would like to thank my parents and girlfriend for their endless love and support.

Abstract

This thesis describes the experimental research carried out on avalanche photodiodes (APDs) for single photon detection. The work covered (i) 1550 nm wavelength single photon detection using InGaAs/InAlAs single photon avalanche diodes (SPADs), and (ii) soft X-ray detection using III-V semiconductor photodiodes or APDs.

SPADs for 1550 nm single photons detection have numerous applications in scenarios where 1550 nm wavelength light detection at very low intensity is essential. InGaAs/InAlAs SPADs with mesa structure are designed and fabricated. The first batch of SPADs showed a temperature coefficient of breakdown voltage ⩽ 7 mV/K, for the temperature range of 260 to 290 K. When operated in gated mode, the SPADs exhibited *SPDE* of 10 and 21 % at room temperature and 260 K, respectively. However, the dark count rates are high, possibly due to BTB tunnelling current in the avalanche layer. Efforts were then made to design and fabricate SPADs with thicker avalanche and absorption layer, resulting in the second batch of SPADs. At 210 K, the highest *SPDE* of 36 % are achieved. Observing activation energy values deduced from the dark count rates, it is likely that tunnelling current persists at the high overbias voltage (required to reach the highest *SPDE*), which could be reduced by increasing avalanche layer thickness. Hence, the data from the two batches of InGaAs/InAlAs SPADs show that they can be practical alternative to InGaAs/InP SPADs, but with the proven advantage of better temperature stability and the promise of greater *SPDE* potential from impact ionisation properties in InAlAs.

The second part of the thesis describes the investigations of InAs avalanche photodiodes (APDs) as X-ray detectors. Combining narrow band gap semiconductor materials (lower Fano-limited energy resolution) and avalanche gain (to reduce the undesirable effect of pre-amplifier's noise in energy resolution), the work focused on InAs APDs for X-rays detection. The liquid nitrogen-cooled InAs APD achieved its best Full width at half maximum (*FWHM*) of 401eV at 5.9 keV. The optimum operation voltage was 10 V, which gave an avalanche gain of 11. The minimum *FWHM* achieved is largely dominated by the measurement system noise and APD leakage current. The influence of the APD structure (p-i-n versus n-i-p) on minimum *FWHM* values was also

studied in detail to experimentally prove that InAs APD with p-i-n structure is more advantageous for small *FWHM*.

The X-ray detector work extended to a study of leakage currents using GaAs mesa p-i-n diodes for X-ray photon counting. Different wet chemical etching solution and etch depth are used in the fabrication of these mesa diodes. Low and uniform leakage currents are achieved when the diode fabrication used (i) a combination of main etching solution and finishing etching solution for the etching, and (ii) partially etched mesas. The diodes fabricated using these methods show well-defined X-ray peaks when illuminated with a ^{55}Fe radioisotope source.

List of publications

Journal publications:

1. **X. Meng**, X. Zhou, S. Zhang, J. Lees, C. H. Tan and J. S. Ng, "InAs X-ray avalanche photodiodes," submitted to Journal of Instrumentation.

2. X. Zhou, **X. Meng**, A. B. Krysa, J. R. Willmott, J. S. Ng, and C. H. Tan, "InAs photodiodes for 3.43 µm radiation thermometry," IEEE Sensors Journal, **15**. 5555-5560 (2015).

3. **X. Meng**, C. H. Tan, S. Dimler, J. P. R. David, and J. S. Ng, "1550 nm InGaAs/InAlAs single photon avalanche diode at room temperature," Optics Express, **22.** 22608-22615 (2014).

4. J. S. Ng, **X. Meng**, J. E. Lees, A. Barnett and C. H. Tan, “Fabrication study of GaAs mesa diodes for X-ray detection,” Journal of Instrumentation, **9**. T08005 (2014).

5. R. B. Gomes, C. H. Tan, **X. Meng**, J. P. R. David and J. S. Ng, “GaAs/$Al_{0.8}Ga_{0.2}As$ avalanche photodiodes for soft X-ray spectroscopy,” Journal of Instrumentation, Journal of Instrumentation, **9**. P03014 (2014).

6. **X. Meng**, S. Xie, X. Zhou, N. Calandri, M. Sanzaro, A. Tosi, C. H. Tan, and J. S. Ng, “InGaAs/InAlAs Single Photon Avalanche Diode with 36 % detection efficiency,” in preparation for submission.

Conference publications:

7. **X. Meng**, S. Xie, X. Zhou, C. H. Tan, and J. S. Ng, “InGaAs/InAlAs single photon avalanche photodiodes for 1550 nm photon counting,” Single Photon Workshop 2015, Geneva, 2015.

8. X. Zhou, **X. Meng**, J. S. Ng, and C. H. Tan, “Si single photon avalanche photodiode for photon-counting thermometry,” Single Photon Workshop 2015, Geneva, 2015.

9. **X. Meng**, J. E. Lees, A. M. Barnett, C. H. Tan, and J. S. Ng, “X-ray spectroscopy with GaAs p-i-n Diodes,” 41st International Symposium on Compound Semiconductors (ISCS), Montpellier, 2014.

10. **X. Meng**, C. H. Tan, R. B. Gomes, I. Sandall, P. J. Ker, and J. S. Ng, “Gamma-ray spectroscopy using InAs photodiodes,” 41st International Symposium on Compound Semiconductors (ISCS), Montpellier, 2014.

11. **X. Meng**, C. H. Tan, and J. S. Ng, "InGaAs/InAlAs Single Photon Avalanche Photodiode for 1550 nm photon counting," 41st International Symposium on Compound Semiconductors (ISCS), Montpellier, 2014.

12. **X. Meng**, C. H. Tan, S. J. Dimler, and J. S. Ng, "InGaAs/InAlAs Single Photon Avalanche Diode at 1550 nm," Semiconductor and Integrated Optoelectronics Conference (SIOE), Cardiff, 2014.

13. **X. Meng**, J. Xie, J. S. Ng, and C. H. Tan, "Comparison of partially and fully etched GaAs p-i-n Diodes for Soft X-ray Detection," UK compound semiconductors conference, Sheffield, July 2013.

14. I. Sandall, X. Zhou, **X. Meng**, A. Krysa, S. Zhang, C. H. Tan, "Development of High Efficiency and uniform InAs APDs for Imaging Applications," 41st International Symposium on Compound Semiconductors (ISCS), Montpellier, 2014.

Glossary of terms

α	Electron ionisation coefficient
α_{abs}	Absorption coefficient
α_T	Fitting parameter for BTB tunnelling
β	Hole ionisation coefficient
ε	Electron hold pair creation energy
ε_s	Permittivity of the semiconductor
ρ	Density
σ	Standard deviation
$\sigma_{p.e.}$	Probability of occurring photoelectric effect
$\sigma_{Compton}$	Probability of occurring Compton scattering
$\sigma_{Rayleigh}$	Probability of occurring Rayleigh scattering
σ_{total}	Total probability X-ray photon interaction
η	Quantum efficiency
η_{cp}	Coupling efficiency
φ	Mass attenuation coefficient
θ	Deflection angle
τ	Generation carrier lifetime
$\mu\cdot\tau(e)$	Electron mobility-lifetime product
$\mu\cdot\tau(h)$	Hole mobility-lifetime product
f	The repetition frequency
f_F	Fano factor
f_{max}	Maximum amplitude of the Gaussian peak
hv	Photon energy
$<i^2>$	Noise current spectral density
k	Ionisation coefficient ratio
k_b	Boltzmann’s constant
n	Ideality factor
$\bar{n}$	Average number of photon per light pulse

n_d	Average number of carriers in a voltage pulse
n_i	Intrinsic carrier concentration
pdf	Probability density function
q	Electron charge
t_{dead}	Dead time
$t_{recovery}$	Recovery time
t_{on}	Pulse width of the AC voltage pulse
t_{reset}	Reset time
w_{abs}	Width of absorption layer
w_{ava}	Width of avalanche layer
w_c	Charge sheet thickness
A	Area
AC	Alternating current
APD	Avalanche photodiode
AQC	Active quenching circuit
BTB	Band-to-band
C	Capacitance
C_{bd}	Temperature coefficient of breakdown voltage
C_f	Feedback capacitance
C_t	Total capacitance
CMOS	Complementary metal oxide semiconductor
CQC	Capacitive quenching circuit
C-V	Capacitance-voltage
CW	Continuous wave
DC	Direct current
DCR	Dark count rate
DUT	Device under test
DMM	Digital multimeter
DNA	Deoxyribonucleic acid
E	X-ray photon energy

E_c	Centroid energy of the energy peak
E_{bind}	Binding energy of the electron
E_R	Energy resolution
E_{th}	Impact ionisation threshold energy
EBT	Electron beam testing
EHP	Electron hole pair
F	Excess noise factor
FET	Field effect transistor
$FWHM$	Full width at half maximum
$FWHM_{EN}$	$FWHM$ due to electronic noise
$FWHM_f$	Fano-limited $FWHM$
FPA	Focal planar array
GBP	Gain bandwidth product
HPGe	High purity germanium
HV-CMOS	High voltage-complementary metal oxide semiconductor
I_0	Intensity of incident photons
I_s	Saturation current
I_{diff}	Diffusion current
I_F	Forward current
I_{g-r}	Generation-recombination current
I_{ava}	Avalanche current
I_{ph}	Photocurrent
I_{pr}	Primary photocurrent
I_{tunn}	Band-to-band tunnelling current
IC	Integrated circuit
I-V	Current-voltage
LADAR	Laser detection and ranging
LIA	Lock-in amplifier
MBE	Molecular beam epitaxy
MCA	Multi-channel analyser

MOCVD	Metal organic chemical vapour deposition
M	Mean avalanche gain
M_e (M_h)	Avalanche gain initiated by electron (hole) injection
M_{mix}	Avalanche gain initiated by electron and hole
NIM	Nuclear instrument module
NIR	Near infrared
N_c	Charge sheet doping density
N_d	Number of measured dark count per second
N_0	Doping concentration of depletion width
N_t	Number of measured total counts per second
P_{abs}	Absorption efficiency
P_{ave}	Average power
P_b	Breakdown probability
P_d	Dark count probability
P_{loss}	Probability that carriers are lost before entering the avalanche layer
P_{ph}	Probability of a light pulse triggering an avalanche
P_t	Total count probability
PCR	Polymerase chain reaction
PECVD	Plasm-enhanced chemical vapour deposition
PICA	Picosecond imaging circuit analysis
PMT	Photomultiplier tube
PQC	Passive quenching circuit
QKD	Quantum key distribution
R_s	Series resistance
R_b	Biasing resistor
R_B	Ballast resistance
R_d	Diode resistance
R_f	Feedback resistor
R_{load}	Load resistance
RIE	Reactive ion etching

RTA	Rapid thermal annealing
SAMAPD	Separate absorption multiplication avalanche photodiode
SI	Semi-insulating
SMU	Source-measurement unit
SNR	Signal-to-noise ratio
SNSPD	Superconducting nanowire single photon detector
SPAD	Single photon avalanche diode
SPDE	Single photon detection efficiency
SSPD	Superconducting single photon detector
T	Temperature
TAT	Trap-assisted tunnelling
TCSPC	Time correlated single photon counting
TEC	Thermoelectric cooler
TES	Transition edge sensor
UV	Ultra-violet
V	Voltage
V_R	Reverse bias voltage
V_{AC}	AC bias voltage
V_b	Bias voltage
V_{bd}	Breakdown voltage
V_{bi}	Built-in potential
V_{DC}	DC bias voltage
V_{out}	Output voltage
V_p	Punch-through voltage
V_t	Total voltage
VOA	Variable optical attenuator
W_d	Depletion width
Z	Atomic number

Contents

Acknowledgement i

Abstract ii

List of publications iv

Glossary of terms vi

Contents xi

1 Introduction 1

1.1 Single photon detection 1

1.1.1 Applications for single photon detection 1

1.1.2 Photomultiplier tubes 4

1.1.3 Superconducting single photon detectors 5

1.1.4 Single photon avalanche diodes 8

1.1.5 Review of single photon avalanche photodiodes 8

1.1.6 Motivations 15

1.2 X-ray detection 16

1.2.1 Applications for X-ray detection 16

1.2.2 Gas-filled detectors 17

1.2.3 Scintillation based detectors 18

1.2.4 Semiconductor detectors 19

1.2.5 Review of semiconductor X-ray detectors 19

1.2.6 Motivations 22

1.3 Thesis organisation 23

1.4 References 24

2 Background theory 33

2.1 Impact ionisation 33

2.2 Avalanche gain and excess noise 34

2.3 SPAD principle of operation 35
2.3.1 Operation mode of APDs 35
2.3.2 Single Photon Detection Efficiency 38
2.3.3 Dark count rate 39
2.3.4 Afterpulsing 40
2.3.5 Timing jitter 41
2.4 Background of radiation detection 42
2.4.1 Interaction of X-rays with matters 42
2.4.2 Photoelectric effect 43
2.4.3 Energy resolution 44
2.4.4 Absorption efficiency 44
2.4.5 Fano factor 45
2.4.6 APD X-ray detector 46
2.5 References 47
3 Experimental methods 49
3.1 I-V measurement 49
3.2 C-V measurement 50
3.3 Photomultiplication measurement 52
3.4 Single photon counting 53
3.4.1 Experimental setup 53
3.4.2 Dark count probability and DCR 56
3.4.3 Single Photon Detection Efficiency 57
3.4.4 Modified CQC for measurements at cryogenic temperature 60
3.5 X-ray spectroscopy 60
3.5.1 Radioactive source 61
3.5.2 Preamplifier 61
3.5.3 Post shaping amplifier 64

3.6 References 67
4 InGaAs/InAlAs single photon avalanche diodes 68
4.1 SPAD device detail 68
4.1.1 Wafer structure 68
4.1.2 Device fabrication 70
4.2 Device characterisation 71
4.2.1 I-V results 71
4.2.2 C-V results 73
4.2.3 SPDE 74
4.2.4 DCR 77
4.2.5 Afterpulsing 79
4.3 Summary 79
4.4 References 80
5 InGaAs/InAlAs SPADs with improved performances 81
5.1 Design criteria 81
5.2 Growth and fabrication 84
5.3 Characterisation results 85
5.4 Comparison with other reports 90
5.5 Summary 91
5.6 References 91
6 InAs APD X-ray detector 93
6.1 Introduction 93
6.2 Device detail and electrical characterisation 95
6.3 X-ray response 96
6.4 Noise analysis 100
6.5 Comparison of InAs p-i-n and n-i-p diodes 101
6.6 Summary 105

6.7 References 105

7 GaAs mesa diodes for X-ray photon counting 107

7.1 Introduction 107

7.2 Device structures 108

7.3 Results 111

7.3.1 C-V results 111

7.3.2 Dark current distribution 112

7.3.3 X-ray spectrum 115

7.4 Summary 116

7.5 References 117

8 Conclusions and future works 119

8.1 Conclusions 119

8.2 Future work 121

8.3 References 123

Appendix A: single photon counting measurement 124

Appendix B: X-ray spectroscopy measurement 127

Appendix C: X-ray noise measurement using test pulser 130

1 Introduction

In this thesis, two types of APDs, namely SPADs and X-ray APDs, are investigated. Hence this chapter will present separate literature reviews relevant to them.

1.1 Single photon detection

1.1.1 Applications for single photon detection

Single photon detectors have drawn increasing interest from a wide range of fields due to its versatility in applications requiring low light level detection. Typical applications relying on or taking advantage of single photon detectors include quantum key distribution (QKD) [1], quantum computing [2], integrated circuit (IC) analysis [3], optical time-domain reflectometry [4], fluorescence lifetime spectroscopy [5], DNA sequencing [6] and laser detection and ranging (LADAR) [7].

As the most well-known example of quantum cryptography, QKD has been intensively investigated since it was firstly proposed by Bennett and Brassard in 1984 [8]. QKD utilises the quantum mechanics effect to ensure secure communication between authorised users. Security of classical cryptography relies on the complexity of chosen mathematical functions (such as factorising the product of two very large prime numbers [1]) which is not perfectly secure since this method always faces threats from ongoing increase in computing ability. The schematic of a basic QKD system is shown in Figure 1-1. Unlike the classical cryptography, QKD allows the authorised users to share a secret key which is used to encrypt and decrypt the message sent between the users. The key is a string of qubit, usually polarised photons, thus the security is ensured by the no-cloning theorem which states that quantum mechanics forbid the replication of an unknown arbitrary quantum state [9]. The experimental QKD was implemented by Bennett *et.al.* from IBM in 1989 [10]. Afterwards, the performances of QKD, such as distribution distance and key generation rate, have significantly improved owing to the efforts from many research groups. Two notable examples are: researchers from Toshiba in Cambridge have demonstrated a QKD system with record high key rate of 1 Mbit/s using an InGaAs/InP SPAD [11] and the QKD system with longest distribution distance of 148.7 km has been achieved by a collaboration research between Los Alamos National Laboratory and National Institute Standards and Technology using a transition edge

sensor (TES) detector [12]. Since 2004 there have been several companies providing commercial QKD systems [13-16].

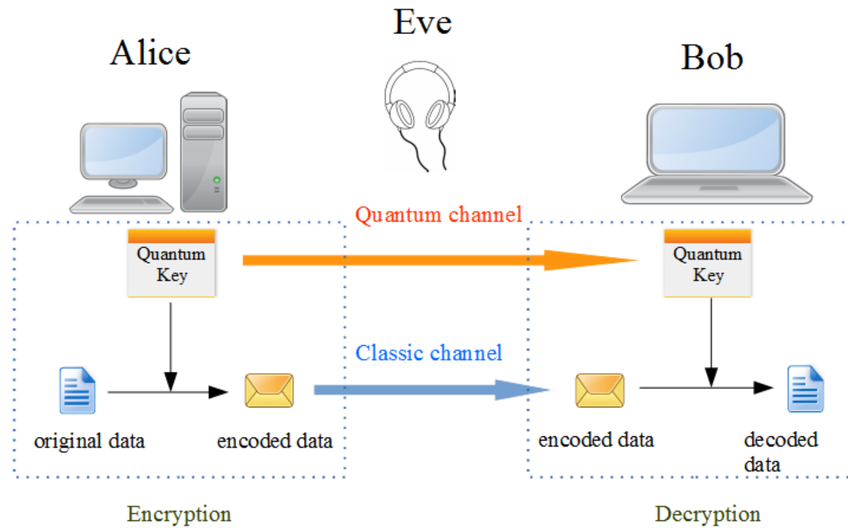

Figure 1-1 Schematic of basic QKD. The sender (Alice) send information to the receiver (Bob) through two channels: quantum channel sending secret quantum keys and classic channel sending encoded information. Eavesdropper (Eve) cannot tap without alerting Alice and Bob.

As the CMOS circuit becomes increasingly more compact and complicated, more advanced methods for IC debugging and analysis are required. For example, Electron Beam Testing (EBT) which is one of the conventional IC failure analysis techniques is struggling to cope with increased metal layers and flip-chip packaging that significantly reduce its efficiency [17]. Fortunately photon emission effect in the CMOS ICs [18] has been utilised to assess the performance of the circuit with the so called picosecond imaging circuit analysis (PICA) technique [19]. NIR photon are emitted when the transistor is switching on and off [20]. PICA acquires the timing information of the emitted photons using time-correlation single photon counting (TCSPC) technique. Meanwhile the position can also be recorded thus a scanning of the whole circuit will generate a circuit image showing location of the failures. Since the intensity of the emitted photon is ultra-low and transistors in the circuit have fast switch speed and high repetition frequency, a single photon detector with high single photon detection efficiency (*SPDE*), low timing jitter and fast response is required. Several types of single photon detectors have been applied in the PICA system including photomultiplier tube (PMT) [19], SPAD [3] and superconducting single photon detector (SSPD) [21]. The first two types can provide sufficient gain but they suffer from low detection efficiency

at NIR wavelength range and low counting rate [22]. The third one has presented the best overall performance including GHz counting rate, 5% detection efficiency at 1300 nm, and timing jitter of 35 ps [21].

In biomedical applications, detection of ultra-low fluorescence has been a useful tool to carry out analysis in single molecule level. Two typical examples are: DNA sequencing and single molecule detection, both of which can benefit from the advent of single photon detectors. DNA sequencing is a technique used to determine the order of nucleotides in a piece of DNA. The basic operation principle of a DNA sequence rely on the identification of the fluorescence light emitted from the fluorescent labels attached to specific nucleotides [23]. Amplification process, such as polymerase chain reaction (PCR), is usually used to generate a large quantity of DNA molecules since conventional detection technique is not sensitive enough for fluorescence from a single molecule. However, the PCR process involves complex preparation steps. This could be eliminated by employing single photon counting technique. The most commonly used single photon detector in commercial DNA sequencers is Photomultiplier Tube (PMT), which offers high sensitivity, low noise and fast response [24]. Owing to the ultra-high gain of single photon detectors, they have also been applied to the single molecule detection [25, 26]. Instead of measuring the average characteristics of a bulk collection of molecules, single molecule detection technique using single photon detector is sensitive enough to measure the properties of a single molecule. Apart from the intensity of the fluorescence, more information can be extracted by conducting TCSPC measurement (e.g. lifetime) which can reflect the environment surrounding the fluorophore [5]. PMTs were the first single photon detector used to detect single molecule due to its good timing resolution [27]. Later SPADs were demonstrated in single molecule detection technique with higher detection efficiency, smaller size and lower operating voltage although they have relatively small active area [26].

As a remote sensing technique, LADAR has been applied to a broad range of fields such as aerial mapping, 3D imaging, gaming industry and robotics. Working in a similar principle with radar, a LADAR instrument deduces the distance of the target by shining laser to the target and measuring the time lapsed at the return signal. The distance between the source and the target is given by the product of the speed of light and half of the time lapsed. TCSPC technique is also employed to enable detection of single-photon

level light (long ranging distance) and picosecond timing resolution (millimetre depth resolution) [28]. The operation wavelength of was initially ~ 900 nm mainly due to the combination of powerful GaAs-based laser and sensitive Si APD [29]. However high power laser at this wavelength causes eye damage concern necessitating an upper limit of the laser power and hence the ranging distance. This problem could be solved by using longer wavelength laser (>1400 nm) at which human eyes are not sensitive hence called eye-safe wavelength. This has driven the researchers to investigate the feasibility of using InGaAs/InP SPAD for eye-safe LADAR with notable results of sub-centimetre depth resolution at kilometre scale ranging distance [30]. LADAR system with SSPDs have also been reported owing to its low *DCR* and low timing jitter [31] although bulky cooling system for the SSPDs is still a major disadvantage.

1.1.2 Photomultiplier tubes

Photomultiplier tubes are the first detectors used to detect light at single-photon level and convert it to an electrical signal [32]. Although emerging SPADs have shown superior performances in some applications, PMTs are still widely applied in fields such as medical diagnosis, chemical analysis, high energy physics experiments and industrial measurement [23]. A conventional PMT is a vacuum tube which houses a photocathode, focusing electrodes, several dynodes (secondary emission electrodes), and an anode, as shown in Figure 1-2.

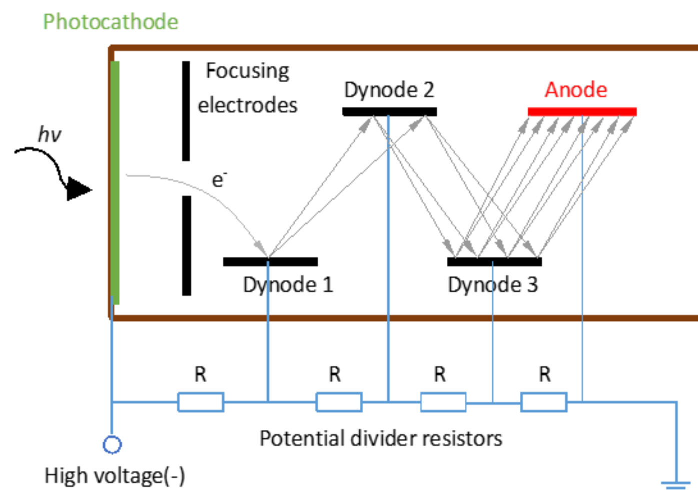

Figure 1-2 Schematic to illustrate the principle of operation for conventional PMTs.

Principle of operation of the PMTs is based on two physical phenomena, namely photoelectric effect and secondary electron emission. When the radiation photons strike on the photocathode, electrons could be emitted to the vacuum as the result of the photoelectric effect, provided the photon has larger energy than the work function of the photocathode. Photocathode are generally made of materials with low work functions such as alkali metals and alkali metal-activated (e.g. Cesium) III-V semiconductors [33]. A high negative voltage in order of 1 kV is applied to the photocathode. A potential divider circuit is used to create successively lower voltages for a series of dynodes. The photoelectron emitted from the surface of the photocathode is accelerated by the electric field towards the first dynode. The process is repeated as the electron moves from the first dynode to the second and then the next until the electron is finally collected by the anode. Crucially, when the accelerated electron hits a dynode, part of its kinetic energy is transferred to some electrons in the dynode. Those electrons with a lower energy could then escape from the surface of the dynode and be emitted to the vacuum, resulting in secondary electron emission. If a gain of 4 is obtained at each dynode, a PMT with 10 dynodes will provide an overall gain of 4^{10} (~ 10^6), which is high enough to generate a detectable current pulse when single photon level light is incident on the photocathode.

PMTs offer large photo-sensitive area (diameter > 10 mm), high gain (> 10^6), and low gain fluctuation [22]. In addition, there exist different PMTs to cover a broad spectral range from UV (~ 115 nm) to NIR (~ 1700 nm). Nevertheless, compared with emerging single photon detector based on semiconductors, PMTs have several drawbacks including bulky size, very high operating voltage, and sensitivity to magnetic field. For example NIR PMTs with InGaAs/InP photocathode commercially available from Hamamatsu have spectral response up to 1700 nm [34], but they require moderate cooling (-60 ^{o}C) reduce the dark count rate and a low quantum efficiency of 2 % is obtained at 1550 nm.

1.1.3 Superconducting single photon detectors

Over the past two decades, superconducting devices have emerged as a promising candidate for single photon detection. These devices can be used to sense light at single-photon level by utilizing their very sharp superconductivity transition at temperatures near their critical temperature. Below the critical temperature, superconductors consist of bonded pairs of electrons, Cooper pairs [35], which can flow without any scattering

meaning that the superconductors have essentially zero resistance. The binding energy of the Cooper pair is in the order of meV. Then the absorption of a photon with enough energy (i.e. photons in visible wavelength with energy of ~ 2 eV) will break the bonds of hundreds to thousands Cooper pairs resulting in a non-superconducting region. Two common types of superconductor-based single photon detectors are Superconducting Nanowire Single Photon Detectors (SNSPDs) and Transition Edge Sensors (TESs).

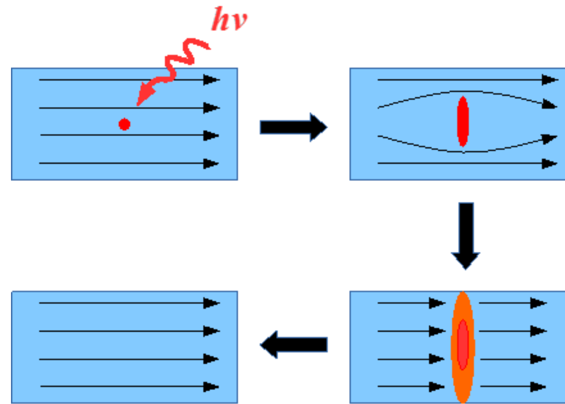

Figure 1-3 Schematic of operation of a SNSPD.

Superconducting Nanowire Single Photon Detectors (SNSPDs) based on NbN were first developed by Gol' tsman *et al.* in 2001 [36]. Generally the detector consists of an ultra-thin (~ several nm) and narrow (~ several hundred nm) superconducting wire. The wire is arranged in a compact meander pattern to maximise the photo-sensitive area and the coupling efficiency from the optical fibre (which delivers the photons) to the detector. NbN is the most popular superconducting material for SNSPD due to its fast response time and relatively high critical temperature (~ 16 K [37]).

SNSPDs operate at a temperature just below its critical temperature and are biased with a DC current slight lower than its critical current. As shown in Figure 1-3, when a photon is incident on the nanowire, absorption of the photon results in a non-superconducting region termed as “hotspot”. As the DC current flows through this resistive region, Joule heating effect further increases the temperature around the hotspot and hence size of the hotspot. As a result, the actual conducting area is shrunk, increasing the local current density. Once the current density is higher than the critical current density a resistive barrier is formed across the whole width of the nanowire, causing a sudden drop of the bias current, which can be sensed by a readout circuit generating a voltage output. At the same time, the hotspot starts to cool since Joule heating effect is

removed by the reduced bias current. Then the hotspot shrinks and the nanowire is restored to the superconducting state.

SNSPDs have demonstrated very promising performance including high detection efficiency of 93% [38], *DCR* below 100 c/s [39], timing jitter of 18 ps [40] and reset times of a few of nanoseconds [41]. However, SNSPDs must operate at cryogenic temperatures so they are not compatible with applications that cannot tolerate the typical size and weight of cryogenic cooling systems.

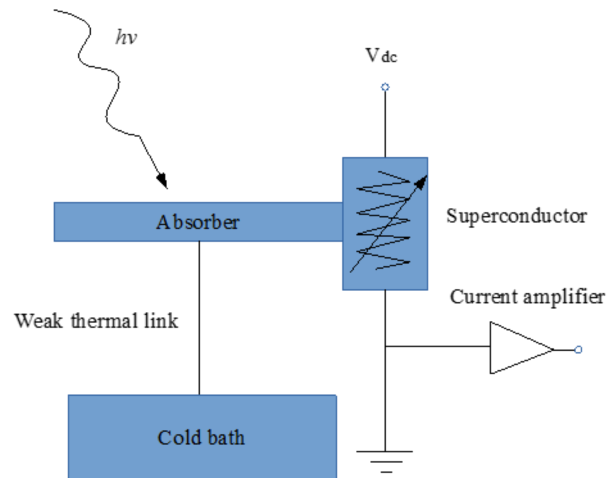

Figure 1-4 Illustration of operation principle of a TES.

Transition Edge Sensors (TESs) depicted in Figure 1-4 are thermometers that consist of an absorber, a thermometer and a weak thermal link connected to a cold bath. These detectors are operated on the sharp edge of the transition between the superconducting state (with zero resistance) and normal state (with finite resistance) of the superconducting material. This very sharp transition enables the sensor to detect temperature change due to very weak radiation absorption, such as a single photon. When an incident photon is absorbed in the absorber, the photon's energy is converted into thermal energy, which can be sensed by the thermometer resulting an increase in the resistance. In order to detect this change in resistance the sensor is normally biased with a DC voltage, so that a change of current due to the photon absorption can be measured with a sensitive current amplifier circuit. Meanwhile, the amount of Joule heating is reduced due to the increase of resistance, causing the sensor to be cooled back to its superconducting state through the thermal link. The thermal conductance of the thermal link must be low, ensuring that the heat from photon absorption is sensed by the thermometer rather than being conducted through the thermal link to the cold bath.

Amongst single photon detectors, optimised TESs exhibited the highest detection efficiency. Lita *et al.* reported detection efficiency at 95% at wavelength of 1556 nm using a fibre-coupled TES [42] and 98% at 850 nm with a titanium TES [43]. Another advantage of TESs is that these sensors are capable of resolving the number of photons because the output signal of a TES is proportional to the total absorbed radiation energy, which is unmatched by most other single photon detectors. Similar to SSPDs, the low operating temperature is also the biggest weakness of TESs. The most common material for TESs, tungsten, has a critical temperature of ~ 100 mK [44], which can only be achieved by sophisticated cooling system (e.g. adiabatic demagnetization refrigerators). Furthermore, TESs suffer from poor timing performance with large timing jitter of 100 ns and long thermal recovery time of 4 μs [45] limiting the maximum count rate and the fidelity of time-correlated photon counting measurement.

1.1.4 Single photon avalanche diodes

SPADs are essentially APDs operated above the breakdown voltage. They are also called Geiger-mode APDs due to analogy to Geiger counters (gaseous detectors for ionising radiation). At voltage above the avalanche breakdown voltage, the very high electric field causes a strong positive feedback effect on the impact ionisation process resulting a self-sustaining avalanche current, whose magnitude grows to become sufficiently large to be detected by an external readout circuit. However, the avalanche current could result in excess heat which will damage the device, necessitating the use of a quenching circuit. Operation principles of different types of quenching circuits will be discussed in chapter 2. Different materials could be used to fabricate SPADs depending on specific applications and a detailed review of SPADs will be presented in section 1.1.5.

1.1.5 Review of single photon avalanche photodiodes

Single photon detection using solid state detector was firstly investigated by researchers in Shockley Laboratory in the 1960s, in particular Haitz. In order to study the physics of avalanche breakdown they designed a Si SPAD with planar technology [46] as shown in Figure 1-5. This design uses a shallow $n^{+}p$ junction surrounded by a guard ring to define the active area and prevent edge breakdown. However the lateral diffusion of the guard ring could reduce the doping in the active area and causes non-uniform *SPDE* across the device. Moreover, this design suffers from long diffusion tail in the photon arrival time distribution, because carriers generated by the photon absorption in neutral

region below the active pn junction could diffuse back to the depletion region with a fluctuating delay. Despite these disadvantages such designs offer low operating voltage and monolithic integration with electronic circuits.

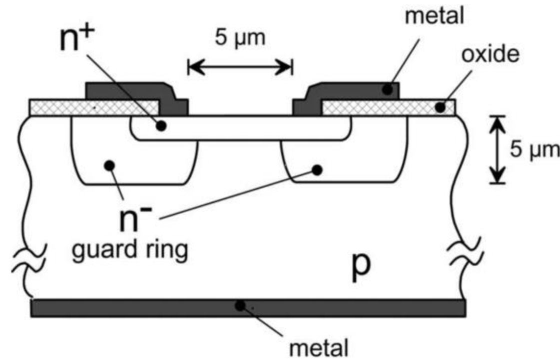

Figure 1-5. Cross-section of the planar Si SPAD devised by Haitz et al. (Image from [47])

In order to overcome the drawbacks of the early planar Si SPAD many efforts have been made [7, 48]. The planar epitaxial devices developed by Lacaita *et al.* [48] have been continuously improved and are now found in PDM series photon counting modules from Micro-Photon-Devices (MPD) [49]. The typical structure of the planar epitaxial devices is shown in Figure 1-6(a). Firstly a p^+/p^- double epitaxial layer is grown on top of an n-type substrate. The junction between the p^+ epitaxial layer and the substrate will prevent the photo-generated carrier from diffusing to the active pn junction at the top, reducing the long diffusion tail. Photon timing distribution peak with *FWHM* of 45 ps and time constant of the diffusion tail of 270 ps has been achieved [48]. Then unlike the lightly doped n-diffusion guard rings used in the early planar devices, a highly p-doping region is formed below the n^+ region to define the active area of the device. This ensures higher electric field in the central region than in the peripheral region, suppressing edge breakdown. Commercial PDM series detectors now exhibit best-in-class timing accuracy of 35 ps, *SPDE* of 49% at 550 nm and *DCR* from 1 to 500 Hz, depending on the diameter of the detector (20 to 100 μm) [49].

Another type of Si SPAD, Si SPADs with non-planar structure shown in Figure 1-6(b), have been developed and produced into commercial devices [51, 52]. The C3092SH series SPAD from EG&G (now Excelitas), with a reach-through geometry firstly developed by McIntyre and Webb in 1970s, has been extensively characterised as a SPAD. A custom-made single photon detector based on C3092SH by Kim *et al.* [53] used a four-stage TEC to cool the detector down to -80° and achieved *SPDE* of >50% at

806 nm and *DCR* of < 5 Hz. The SLiK^{TM} device fabricated with a modified reach-through structure was subsequently released from EG&G and employed in single photon counting modules. Instead of using a separated absorption and avalanche layer, SLiK^{TM} devices have a high electric field across its whole structure. Thicker depletion region reduces the electric field ensuring that the ionisation coefficient ratio, *k*, is as low as possible. Very low value of k (i.e. 0.002) has been obtained which will result in a higher breakdown probability (i.e. P_b, which is defined as the ratio of number of carriers triggering breakdown to number of injected carrier) and higher *SPDE* compared with the reach-through structure (*k* of 0.02). *SPDE* of 50% at 830 nm, *DCR* <1500 Hz and diameter of 180 μm have been achieved at room temperature [51]. However, SLik^{TM} devices have some inherent disadvantages such as high operating voltage, high power dissipation and large timing jitter. Also the non-planar fabrication are complex and cannot be used to integrate the SPAD with circuits.

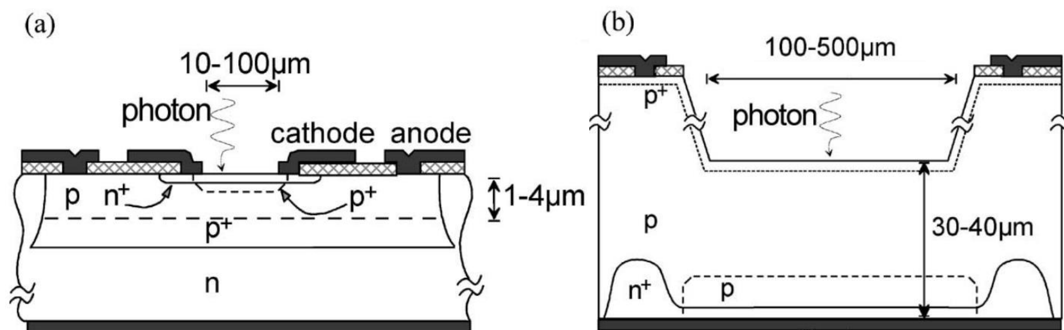

Figure 1-6 (a) Schematic of planar epitaxial structure reported in [48]. (b) Slik^{TM} devices with reach-through structure. (Images from [50])

Si SPADs are also produced by CMOS technologies used in silicon industry due to their potentials of low production cost and achieving complex system on chip. The CMOS technologies explored are High-Voltage CMOS (HV-CMOS) and Standard Deep-Submicron CMOS. HV-CMOS have drawn more attentions in the fabrication of SPAD for red and infrared wavelength due to their thick junction and higher voltage. Si SPADs using HV-CMOS technology were reported by ([54] with 0.8 μm technology and [55]with 0.35 μm technology). Example performance are *SPDE* of 35% at 450 nm (droping to 15% at 600 nm) and an average *DCR* of 750 Hz [55]. Through monolithic integration of the detector and the quenching circuit, the parasitic capacitance across the detector is significantly reduced [56]. This is expected to reduce severity of afterpulsing since the total amount of charge during the avalanche event is reduced [57]. The reduced

parasitic capacitance also decreases the recharging time when a simple passive quenching circuit is used increasing the maximum counting frequency.

CMOS technology with deep-submicron resolution has been used to produce large-format dense SPAD arrays integrated with electronic circuits [58-62]. Early results indicated problems of lateral diffusion of the guard ring limiting the minimum active area of the device [58]. Later efforts employed shallow-trench isolation instead of guard ring [60, 61]. *SPDE* of 25% at 560 nm and <100 Hz *DCR* were obtained for an 8 μm diameter SPAD at room temperature [61]. SPADs produced using 90 nm CMOS, as shown in Figure 1-7, also achieved high performances [62] through moving the high field region to the junction formed between the deep n-well and the p-type epitaxial layer. *SPDE* of 44% at 690 nm and 20% at 850 nm were obtained because the active junction is buried deeply at which more photons at longer wavelength are absorbed.

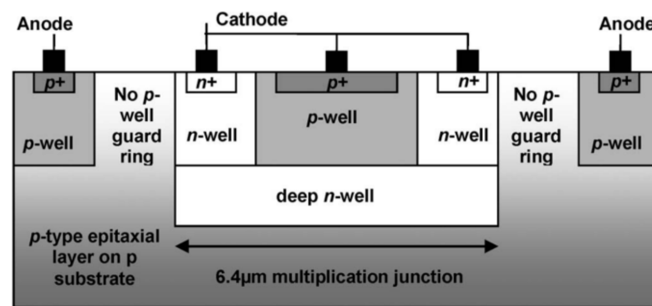

Figure 1-7 A Si SPAD with 90 nm CMOS technology [62].

Driven by the demands from applications such as LIDAR, 3-D imaging and fluorescence lifetime imaging, development of SPAD arrays fabricated with CMOS technology have been made significant progresses. The first large SPAD array (32×32 pixels) implemented with 0.8 μm HV-CMOS technology was reported by Niclass *et al.* [63]. However, the sequential addressing scheme allows only one pixel to be processed at a time limiting the read-out rate. Later efforts were made to overcome this limitation resulting in 35% *SPDE* at 450 nm and *DCR* of ~ 1000 Hz from a SPAD array of 32×32 pixels implemented with 0.35 μm HV-CMOS technology [64]. Each pixel in this array can detect the photon, digitise the signal and temporarily store the data. Recent advances in SPADs implemented in 130 nm technologies allow more functional circuits (e.g. picosecond resolution time-digital-converter) to be integrated on a pixel [65, 66].

Alternatively, custom technologies have been also used to fabricate SPAD arrays. Those devices were used in applications such as protein microarray detection [67] and single molecule fluorescence [68]. Since the samples under test in these applications are extremely small, SPAD arrays with large-area pixels are preferred to make the alignment of the SPAD array easier. *SPDE* of 50% at 550 nm and *DCR* in order of 1000 Hz were achieved with the 50 μm diameter pixel detectors [67].

Despite excellent performance at visible region, Si SPADs are not suitable for NIR wavelength because absorption coefficient of silicon from 1 μm onwards are low. Si SPADs therefore cannot be used at 1300 nm and 1550 nm, the important fibre based telecommunication windows. Germanium, which has a narrower bandgap, is able to detect up to 1600 nm wavelength at room temperature. Therefore research has been carried out to investigate performance the Ge-based SPADs [4, 69, 70]. But Ge-based SPADs require cooling to cryogenic temperature (77 K) in order to manage the dark count rate, but cooling shifts the SPADs detection cutoff wavelength to 1450 nm, resulting in very low *SPDE* at 1550 nm telecommunication wavelength. More recently, progress in growing Ge on Si has resulted in Ge-on-Si APDs with very impressive performances [71]. Ge-on-Si APDs use SAM structure, in which Ge and Si are used in absorption and multiplication layer respectively. These detectors are capable of detect single photons at wavelength of 1310 nm [72, 73].

InP based heterostructure APDs, especially the widely used InGaAs/InP SAMAPD structure, have been the most promising candidate for practical single photon detectors at telecom wavelengths due to its excellent performances at those wavelengths. The SAMAPD structure uses a narrow bandgap material InGaAs(P) as the absorption layer and a wide bandgap material InP as the multiplication layer, which was first developed by Nishida *et al.* [74] and later improved by Campbell *et al.* [75]. This design ensures that the electric field in absorption layer is low enough to avoid tunnelling current while keeping the electric field in avalanche layer high enough to result in high gain. Commercial APDs have been available since 1990s. Early research on InP-based SPAD were focused on characterisation of commercial InGaAs/InP APDs as SPADs [76-79]. Epitaxx-APD was found to yield best performances such as dark count probability in order of 10^{-5}, *SPDE* of 10% and timing jitter of 500 ps at -60 ºC although the maximum counting rate was limited by the afterpulsing effect [79]. Later, instead of relying on

selecting the suitable commercial linear APDs, researches began optimising the device design for SPADs [80-83]. Donnelly *et al.* established a model to predict the *SPDE* and *DCR* versus overbias and temperature for InGaAsP/InP SPAD with different thickness of avalanche and absorption layers. Their results indicate that SPADs with thicker avalanche layer tend to have lower *DCR* for a given *SPDE*, because thicker avalanche layer breaks down at a lower electric field, and hence lower *DCR* induced by tunnelling effect [80].

The first specifically designed planar InGaAs/InP SPAD shown in Figure 1-8 were reported by Pellergrini *et al.* [81]. In anticipation of decreasing breakdown voltage with cooling, this device was designed to have enough difference between punch through voltage and breakdown voltage to allow operation at 200 K. Double zinc-diffusion and floating guard rings were used to suppress the edge breakdown. Although the performances of the SPAD (*SPDE* of 10%, *DCR* of 100 kHz and timing jitter of 470 ps) did not exceed those of selected linear APDs, the work provided valuable insights into specific design and fabrication criteria for InGaAs/InP SPADs. Another InGaAs/InP SPAD with similar design was reported by Itzler *et al.* [82] which has been constantly improved [83] and is now available from Priceton Lightwave. In addition to the design features used in [81], this SPAD also uses back illumination with anti-reflection coating to improve the *SPDE* (*SPDE* of 20% with *DCR* ~ 1 kHz at 218 K).

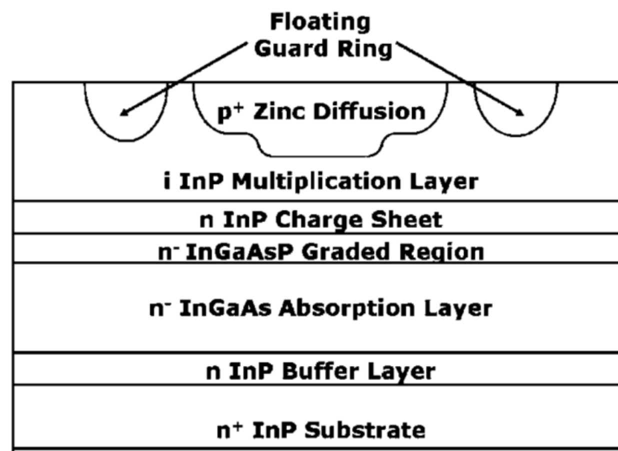

Figure 1-8 Schematic cross section of a planar InGaAs/InP SPAD [81].

As the wafer growth of InGaAsP material system is less matured than that of silicon, afterpulsing problem has limited the maximum counting rate of InGaAs/InP. Several

approaches have been proposed to reduce the severity of afterpulsing effect. The first successfully strategy is rapid gating technique used by Namekata *et al.* [84] in which the SPAD was gated by a very high frequency sinusoidal (instead of square) voltage signal (800 MHz) to reduce the total charge during the avalanche event hence the afterpulsing effect. InGaAs/InP SPADs operated at GHz frequency with very low afterpulsing probability of 0.63% and *SPDE* of 10.9% are now used in commercial QKD systems [85]. However, applications such as TCSPC prefer ungated operation for more efficient data acquisition [86]. Instead of trying to decrease the "on" time, researchers started to reduce the quenching time by monolithically integrating a resistor with the SPAD. The parasitic capacitance will be significantly minimised, therefore, a SPAD with fast self-quenching is achieved (so called Negative Feedback Avalanche Diodes [87]). Furthermore research on ungated operation, which uses the very fast quenching (either passive [88] or fast gate [89]) to reduce the avalanche charge, have been investigated and subsequently commercialised [90, 91].

InGaAs/InP SPAD in large array format which can be used in 3-D imaging was first investigated by researchers in Lincoln lab [92]. The technique was later licensed to two companies: Princeton Lightwave [93] and Spectrolab [94]. 3D Lidar cameras with 32×32 InGaAs/InP (1550 nm) and 128×32 InGaAsP/InP (1064 nm) SPAD FPA are commercially available [93].

A number of groups reported photon counting experiments using APDs with InAlAs, instead of InP, as the multiplication layer [95-99]. InGaAs/InAlAs APDs operated in sub-Geiger (or linear) mode has been characterised in [95, 96]. *SPDE* of 14% with *DCR* of 850 kHz were obtained at 175 K, moreover, no afterpulsing was observed at upto 48 MHz count rate [96]. However the photon counting performances were still limited by the amplifier noise and excess noise of the APD. InGaAs/InAlAs SAPDs have also been reported [97-99]. The first InGaAs/InAlAs SPAD, reported by Karve *et al.* [8], exhibited *SPDE* of 16% at 130 K. Nakata *et al.* [9] achieved better overall performance with *SPDE* of 10% at 213 K, which was probably partially due to the much smaller SPAD diameter (20 μm, typical in recent SPADs) than that in Karve *et al.* (160 μm). A self-quenching InGaAs/InAlAs SPADs operated in sub-Geiger mode was also demonstrated with *SPDE* between 6 and 14% at 240 to 120 K [10].

In recent years, the interest on single photon detection at wavelength >1600 nm is increasing. Therefore some new designs have emerged including GaSb-based InGaAsSb/AlGaAsSb SAMAPD [100] and InP-based SAMAPD using InGaAs/GaAsSb Type-II superlattice as the absorption layer [101].

1.1.6 Motivations

Although InGaAs/InP APDs have been widely applied to NIR applications, InAlAs has become an attractive alternative as the multiplication layer [102]. The main reason is that InAlAs has more dissimilar ionisation coefficient than InP [103] which leads to lower excess noise. Another advantage of InAlAs over InP is that it can withstand higher electric field before significant tunnelling effect appears due to its slight higher bandgap [103]. Furthermore, the temperature stability of APD using InAlAs as multiplication layer was reported to be better than that using InP [104]. Because of the advantages mentioned above numbers of research on InGaAs/InAlAs APDs have been carried out and high performances (e.g. GBP of 240 GHz and dark current of 1.24 nA [105]) have been achieved [105-109]. For imaging applications, InGaAs/InAlAs APD arrays have been fabricated and characterised by several groups [96, 110, 111]. Uniformly good performances have been demonstrated, i.e. variation of breakdown voltage is less than 2.5 V and dark current at gain of 10 ranges from 1.5 nA to 2.5 nA, in a InGaAs/InAlAs APD array with 256×256 pixels across 1.5 cm×1.5 cm area [96]. As InGaAs/InAlAs APDs becomes more mature, currently large format arrays are commercially available from two companies (i.e. 1k×1k array in Voxtel [112] and 256×256 in OptoGration [113]).

These advantages brought by InGaAs/InAlAs APD still holds for SPAD. For example, a SPAD with a 2.5 μm absorber and a 1.0 μm avalanche layer (as from [81]) has a temperature coefficient of avalanche breakdown voltage, C_{bd}, of 151 or 57 mV/K, depending on whether the avalanche layer is made of InP or InAlAs, as predicted using equations 1 and 2 from [104]. Moreover, InAlAs SPADs have potentially higher *SPDE*, which is directly proportional to avalanche breakdown probability, P_b, than InP SPADs. It is well established that P_b rises more rapidly with overbias ratio, defined as $(V - V_{bd})/V_{bd}$, in InAlAs than in InP [114-116]. Using 1.0 μm avalanche layer as an example, P_b at 5 % overbias ratio is 0.72 and 0.58 for InAlAs and InP, respectively, with larger differences at smaller overbias ratio [114].

Therefore, in this thesis, InGaAs/InAlAs SPADs for 1550 nm detection have been developed in order to take advantage of the benefits associated with InAlAs avalanche layer.

1.2 X-ray detection

1.2.1 Applications for X-ray detection

X-rays were firstly discovered and systematically investigated by German physicist Wilhelm Rontgen [117]. X-rays are high energy electromagnetic radiation with photon energy in the range of 100 eV to 100 keV [118]. They can penetrate opaque objects and image the inside with an X-ray detector. So they find significant applications in medical imaging, industrial radiography and security scanning. X-ray are also used in other applications such as X-ray crystallography and X-ray spectroscopy. X-ray applications can be roughly divided into three categories, namely medical applications, industrial applications and scientific research.

Medical applications include radiography and radiotherapy. Medical radiography is an imaging technique which uses X-ray detection to generate images of internal parts of a patient. This is used to assist the doctors in diagnosing diseases (e.g. dental radiography for detecting cavities) or injuries (e.g. X-ray imaging for diagnosing broken bones). When X-rays pass through the part to be examined, denser objects (e.g. bones and teeth) attenuate more X-rays than soft tissues resulting in a radiograph captured by a photographic film or a digital detector. X-ray Computed Tomography is a type of advanced radiography which can generate a 3-D image of the inside of a patient giving more details than a conventional radiography. In X-ray radiotherapy, X-rays are used to kill tumour cells, as part of cancer treatment. Similar to medical radiography, industrial radiography makes use of the penetrating property of X-rays to inspect the hidden flaws or failures of commercial products which otherwise could not be seen easily. Commercial X-ray inspection systems for food quality control are available in [119]. The third category of applications is scientific research. A typical example is X-ray crystallography which can be used to determine the crystal structures using the diffraction pattern produced by X-rays striking on the crystal. A notable example of this application is the discovery of DNA molecule by J. Watson and F. Crick in 1953 using X-rays [120].

1.2.2 Gas-filled detectors

A gas-filled detector is an ionising radiation detector that usually consists of a cylindrical container filled with noble gases (e.g. argon), a positive electrode along the central axis of the cylinder, a negative electrode on the sidewall of the cylinder, and a window at the end. When an X-ray photon passes through the gas, the gas atoms or molecules could be ionised and electron-ion pairs will be created. External voltage applied to the electrodes will then drive the generated electrons and ions to anode and cathode, respectively, resulting in a current signal which could be detected by the readout circuit. The number of collected carriers, thus pulse height of the resulted current signal, varies with the voltages, as shown in Figure 1-9. Three regions have been utilised in three different gas-filled detectors namely ionisation chamber, proportional counter and Geiger-Muller counter.

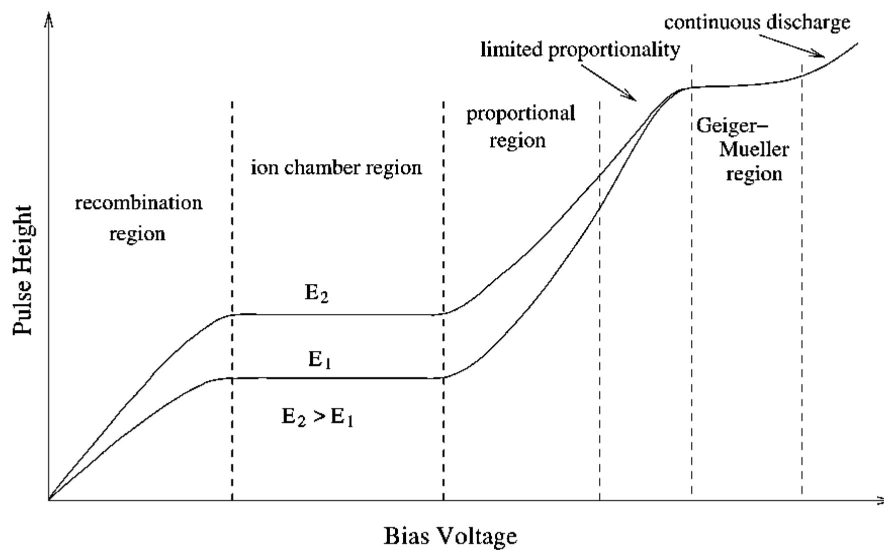

Figure 1-9 Different regions of operation of a gas filled detector. The two curves correspond to two different energies of incident radiation.

In an ionisation chamber, all the generated electron-ion pairs are collected and pulse height does not vary with the bias voltage. They are widely used in applications such as intensity measurement in X-ray crystallography, high dose rate radiation monitoring and smoke detectors. However, they require a low noise amplifier, when used to detect low energy ionising radiations.

With higher bias voltage, the gas-filled detector can operate in the proportional region in which pulse height is proportional to the bias voltage. The primary charges gain

enough energy from high electric field to ionise more gas atoms, creating secondary charges, which can initiate further ionisations, finally resulting in an avalanche multiplication of the primary charges. Owing to the multiplication in proportional counter, there will be less stringent requirements on low-noise amplifier to detect low energy ionising radiation.

If the bias voltage is increased further, the gas-filled detector will be operated in Geiger-Muller region where it is called Geiger-Muller counter. Unlike the ionisation chamber and proportional counter which have a pulse height proportional to the radiation energy, Geiger-Muller counter will output the same pulse height regardless of the radiation energy. The reason is that avalanche events in a Geiger-Muller counter could emit UV photons due to the relaxation of atoms. The emitted UV photons can hence generate new electron-ion pairs which is accelerated under very high electric filed and could trigger more avalanches. The new avalanches will in turn produce more UV photons. This positive feedback will result in a huge amount of avalanche spreading throughout the whole detector. After the avalanches reach a certain size the collective effect of ions which have lower mobility than electron will terminate this positive feedback effect. This saturation effect makes Geiger-Muller counter not suitable for applications requiring energy resolving capability (e.g. X-ray spectroscopy). However, due to its ultra-high multiplication the need of amplifier is minimised or even eliminated making Geiger-Muller counter an ideal candidate for portable instrument to monitor ionising radiations.

1.2.3 Scintillation based detectors

Scintillation based detectors use a scintillation material to convert high energy photon to visible photons which can be detected with a PMT or APD. The conversion is a result of photoluminescence in which the incident high energy photons interact with the atoms in the scintillation material, bringing some of the electrons to an excited state, and then visible photons are emitted during the de-excitation of the atoms. The visible photons will be detected by a photodetector giving the energy of the incident radiation. Due to this two stage process, detection techniques using scintillation based detectors are sometimes termed indirect detection techniques as opposed to direct detection techniques in which semiconductor can convert the high energy photons into electrical signal directly. The scintillation materials can be divided into organic (e.g. anthracene $C_{14}H_{10}$)

and inorganic (e.g. NaI(Tl)). The emission time of inorganic scintillator is much longer than that in organic materials, however, inorganic materials have higher density which gives higher efficiency in the detection of high-energy radiations. Since visible light emitted from the scintillator is very weak, a photodetector with amplification (i.e. PMTs or APDs) will be required to generate a measurable electrical signal.

1.2.4 Semiconductor detectors

In a semiconductor detector the passage of radiation create electron-hole pairs (EHPs) which are swept to the electrodes under electric field generating an electrical signal. The process is analogous to that in the gas-filled detectors except that the carriers are electrons and holes instead of electrons and ions. The main advantage of semiconductor detectors over other radiation detectors is their high energy resolution in X-ray spectroscopy. This is a result of smaller average EHP creation energy which reduces the statistical broadening of the peak in an energy spectrum. For example, average electron-ion pair creation energy is 26 eV for Ar, energy loss for creation of one photon in NaI is 25 eV, EHP creation energy is 3.6 eV for Si. Therefore, for a certain incident radiation energy, number of charges generated in semiconductor is more than other X-ray detectors reducing the lower limit of the energy resolution placed by Fano noise (i.e. a type of noise in energy spectroscopy caused by statistical fluctuation in number of generated charges). Other advantages of semiconductor X-ray detectors including compact size, insensitive to magnetic field and high detection efficiency make them suitable for most of applications in radiation detection. However, in some applications, semiconductor detectors suffer from small active area and degradation due to radiation damage. Different types of semiconductor X-ray detectors in terms of material will be detailed in section 1.2.5.

1.2.5 Review of semiconductor X-ray detectors

Si and Ge detectors have been the work-horse in almost all radiation detection applications due to the maturity in their growth and fabrication techniques and good carrier transport properties. Early Si and Ge detectors use the depletion region of a reverse biased PN junction as the active region to absorb incident radiations and generate electrical signals. One main limitation of this configuration is that the wide depletion width, and hence high detection efficiency, relies on very low doping density of the wafer. For example, the maximum depletion width is about 1 mm for PN junction detectors and

Schottky barrier detector. But in order to get a good detection efficiency at high energy X-ray range (>20 keV) at least several mm thick Si is needed. One solution is to make use of Lithium ion drifting process to compensate the residual doping achieving an "intrinsic" region which could increase the depletion width up to ~ 1 cm. This technique has been successfully applied to both Si and Ge X-ray detectors known as Si(Li) and Ge(Li) respectively. However at room temperature the drifted lithium tends to redistribute making the detectors unusable. Hence they are usually cooled to liquid nitrogen temperature continuously. Moreover the dark current of lithium drifted detectors is much higher than thinner detector, which again requires the detector to be cooled down to cryogenic temperature to reduce the leakage current related noise. Alternatively, more advanced techniques capable of achieving impurity concentration as low as 10^9 atoms/cm^3 have been developed for germanium, which is the so called High Purity Germanium (HPGe). These detectors still need to be cooled to liquid nitrogen temperature in order to reduce the thermal dark current, but only when they are operated. For applications in hard X-ray or Gamma-ray range, HPGe detectors are preferred than Si(Li) detectors since Ge has a higher atomic number than Si (32 for Ge, 14 for Si) meaning a better detection efficiency at the same radiation energy.

Table 1-1 Summary of properties of common materials used as radiation detectors [121-123].

Material	Si	Ge	CdTe	$Cd_{0.9}Zn_{0.1}Te$	InAs	GaAs
Atomic number	14	32	48,50	48,30,52	49,33	31,33
Density (g/cm^3)	2.33	5.33	6.20	5.78	5.68	5.32
Bandgap (eV)	1.12	0.67	1.44	1.57	0.35	1.43
Pair-creation energy (eV)	3.62	2.96	4.43	4.6	1.6	4.2
Fano-limited energy resolution @ 5.9 keV (eV)	118	112	142	145	86	129
Resistivity (Ω·cm)	10^4	50	10^9	10^{10}	0.2	10^7
$\mu\cdot\tau(e)$ (cm^2/V)	>1	>1	10^{-3}	10^{-3}-10^{-2}	0.1	10^{-5}
$\mu\cdot\tau(h)$ (cm^2/V)	~1	>1	10^{-4}	10^{-5}	10^{-5}	10^{-6}

Although Si and Ge are still dominating the radiation detector market, Si suffers from low detection efficiency (due to low atomic number) and Ge cannot work without cryogenic cooling (due to narrow bandgap). So many efforts have been made to develop radiation detector using compound semiconductors. Compound semiconductors which

have been investigated as radiation detector are main from group II-VI such as CdTe and CdZnTe, group III-V such as GaAs and InP. Table 1-1 shows the comparison of common materials used as radiation detectors.

CdTe is one of the most popular compound semiconductor radiation detector. It has bandgap of 1.44 eV which is large enough to permit room temperature operation. Moreover, its high atomic number (48 for Cd, 52 for Te) and high density (5.85 g/cm^3) results in high detection efficiency than Si and Ge. Takahashi *et al.* [124] have demonstrated *FWHM* of 1.8 keV at energy of 59.5 keV obtained from a CdTe Schottky detector. However this device suffer from temporal instability resulted from polarisation effect. This polarisation effect is basically due to the accumulation of trapped carrier forming space charges and making the electric field finally collapse. It has been shown that this effect could be reduced by applying higher bias voltage and lowing the operating temperature. Low carrier mobility-lifetime product is one main disadvantage of CdTe detector, and this is mainly caused by the relatively high density of impurities and defects which trap the photo-generated carriers. In X-ray spectroscopy applications, low carrier mobility-lifetime product will result in low carrier collection efficiency and low energy tail (i.e. poor energy resolution). CdTe detectors with epitaxial PIN structure have been investigated by several groups in order to obtain wafer with low leakage current. High performance CdTe PIN detectors giving *FWHM* of 270 eV at 5.9 keV were achieved by Khusainov *et al.* [125]. This detector was cooled to -45 ^{o}C at which temperature no polarisation effect was observed after 10 hours operation. Currently commercial radiation detection instruments using CdTe detectors are available in several companies such as portable gamma-ray detector from Amptek [126] and dental imaging system from AJAT [127]. CdZnTe is a ternary compound which has close atomic number to CdTe and higher bandgap (1.44 keV-2.2 keV depending on percentage of Zn). Apart from the higher band gap, addition of Zn is also believed to reduce the dislocation density thus the polarisation effect [128]. Both of those two effects will increase the resistivity of the material giving lower leakage current. *FWHM* of 240 eV at 5.9 keV at -40°C was reported from a 2×2×2 mm^3 CdZnTe detector by Niemela *et al.* [129]. However, CdZnTe still suffer from low energy tail caused by low hole mobility-lifetime product at higher energy [130]. Several methods focusing on single carrier sensing techniques have been developed to solve the hole trapping problem [121].

As a radiation detector, GaAs has several promising features including relatively high average atomic number (Z = 32) and bandgap (1.43 eV). Additionally the growth and fabrication techniques of GaAs is more developed than other compound semiconductors owing to their broad range of applications in high speed electronics and optoelectronics. GaAs detectors are generally realised in two methods: Schottky diodes using semi-insulating (SI) GaAs and epitaxially grown p-i-n diodes. Early researches have shown that SI GaAs detectors have good room temperature capability, however, they suffered from high defect density and non-uniform electric field [131]. A typical example is the 130 μm thick bulk GaAs detector reported by McGregor *et al*. which demonstrated room temperature *FWHM* of 8 keV at 59.5 keV[132]. Later, with the emerging of Medipix1 chip (CMOS readout chip designed by Medipix collaboration) an X-ray imaging array with 64×64 SI GaAs pixels has been reported [133]. Images from various objects were obtained using X-ray with energy in the dental imaging range. Leakage current density of 2.7 μA/cm^2 was measured. More recently, X-ray imaging detectors using chromium (Cr) compensated SI GaAs have been demonstrated by several groups [134, 135]. High resistivity in order of 10^9 Ω has been achieved. More notably, *FWHM* of ~ 3 keV was obtained at near room temperature (280 K) at 59.5 keV [135]. GaAs p-i-n detectors with high quality epitaxial GaAs was fabricated by Owens *et al*. [136, 137]. These detectors were produced by growing 40 μm epitaxial layer (with 10 μm p$^+$ deposited on top) on n$^+$ substrate by chemical vapour phase deposition. Typical leakage current density of 4 nA/cm^2 at 100V reverse bias was obtained. With improved ultra-low noise charge ampfiler design, the best energy resolution (*FWHM* of 266 eV and 487 eV at 5.9 keV and 59.5 keV respectively) has been achieved. An array detector with thicker epitaxial GaAs (140 μm) was reported by Kostamo *et al*.[138]. This array detector which has 256×256 pixels with p-i-n structure and a total area of 1.4×1.4 cm^2 was bump-bonded to the Medipix2 readout chip for X-ray imaging applications.

1.2.6 Motivations

Although Si and Ge are still dominating the radiation detector market, they are showing limited performances in various applications due to their intrinsic properties. An ideal radiation detector will simultaneously satisfy following requirements: large active volume, good carrier transport properties, good detection efficiency, capability of room temperature operation and high energy resolution. Both Si and Ge perform well in the first two aspects, however, Si suffers from low detection efficiency at higher energy

and Ge requires cryogenic cooling. Therefore it is necessary to develop radiation detector using compound semiconductors which could offer a wide range of candidates with properties suitable for almost any application. Cd(Zn)Te are very promising materials for X-/γ- ray detector at room temperature, however, difficulties in their growth hindered the widespread use of them.

In contrast, III-V semiconductors have mature growth and processing technologies, which motivates me to explore the X-ray performances of III-V semiconductors. InAs, is an interesting candidate for high-energy resolution semiconductor X-ray detector since it can potentially give better energy resolution (narrow band gap) and higher detection efficiency (large atomic number) than Si and Ge. Apart from the interest on this material, creating InAs APDs with optimised structure giving the best spectroscopic performances is also the aim of this work.

Another section focuses on study of X-ray detectors using GaAs, which can be used as room temperature X-ray detectors and GaAs-based APD X-ray detectors. Previous work on GaAs detector have shown promising results in applications such as X-ray spectroscopy and X-ray imaging. In these applications, dark current of the diodes play a significant role since high dark current will degrade the energy resolution and variation of dark current from diode to diode will result in poor image quality. However very limited progress in reducing and managing dark current in GaAs has been reported. The main motivation of this work is to investigate the effect of wet chemical etchants and etch depths on the dark currents of GaAs diodes.

1.3 Thesis organisation

The work presented in this thesis focus on the development of InGaAs/InAlAs SPADs at NIR wavelength and X-ray detectors using III-V semiconductors. Chapter 2 introduces the background theory of avalanche photodiodes including impact ionisation, avalanche gain and excess noise. This is followed by the principle of operation and figure of merits of SPADs. The background of radiation detector is also described. In chapter 3, the basic APD characterisation measurements (I-V, C-V and photomultiplication) are described. This chapter will also provide the details of characterisation setups for SPADs and X-ray detectors. The design, fabrication and characterisation of our InGaAs/InAlAs SPADs will be presented in chapter 4. Analysis on the origin of the high *DCR* will be

discussed. According to the modelling results, modifications in the SPAD structure were made. The InGaAs/InAlAs SPADs with improved structure have been fabricated and demonstrated promising photon counting performances in chapter 5. In chapter 6, InAs APDs are demonstrated to detect soft X-ray with an energy resolution of 401 keV. The advantage of avalanche gain has been shown by measuring the energy resolution at different bias voltages (different avalanche gain). Noise analysis has been carried out to assess the significance of electronic noise at different bias voltages. A comparison of InAs APDs with p-i-n and n-i-p structures is also discussed. Chapter 7 describes the study on influence of etching solution and depth on GaAs mesa diodes for X-ray detection. With appropriate etching recipe and partially etched mesa, our GaAs diodes present uniformly low dark current. The X-ray spectroscopic results from these diodes are also included. Finally, chapter 8 will conclude for the work on InGaAs/InAlAs SPAD and III-V X-ray detectors and give suggestions for their future directions.

1.4 References

[1] N. Gisin, G. Ribordy, W. Tittel, and H. Zbinden, "Quantum cryptography," *Reviews of Modern Physics,* vol. 74, pp. 145-195, 2002.

[2] T. D. Ladd, F. Jelezko, R. Laflamme, Y. Nakamura, C. Monroe, and J. L. O'Brien, "Quantum computers," *Nature,* vol. 464, pp. 45-53, 2010.

[3] F. Stellari, A. Tosi, F. Zappa, and S. Cova, "CMOS circuit testing via time-resolved luminescence measurements and simulations," *Instrumentation and Measurement, IEEE Transactions on,* vol. 53, pp. 163-169, 2004.

[4] B. F. Levine and C. G. Bethea, "Single photon detection at 1.3 μm using a gated avalanche photodiode," *Applied Physics Letters,* vol. 44, pp. 553-555, 1984.

[5] K. Suhling, J. Siegel, D. Phillips, P. M. W. French, S. Lévêque-Fort, S. E. D. Webb*, et al.*, "Imaging the Environment of Green Fluorescent Protein," *Biophysical Journal,* vol. 83, pp. 3589-3595.

[6] L. Alaverdian, S. Alaverdian, O. Bilenko, I. Bogdanov, E. Filippova, D. Gavrilov*, et al.*, "A family of novel DNA sequencing instruments based on single-photon detection," *ELECTROPHORESIS,* vol. 23, pp. 2804-2817, 2002.

[7] B. F. Aull , D. J. Young , R. M. Heinrichs , B. J. Felton , P. J. Daniels and D. J. Landers, "Geiger-mode avalanche photodiodes for three-dimensional imaging," *Lincoln Lab. J.,* vol. 13, pp. 335-350, 2002.

[8] C. H. Bennett and G. Brassard, "Quantum cryptography: Public key distribution and coin tossing," in *Proceedings of IEEE International Conference on Computers, Systems and Signal Processing*, Banglore, India, pp. 175-179, 1984.

[9] W. K. Wootters and W. H. Zurek, "A single quantum cannot be cloned," *Nature,* vol. 299, pp. 802-803, 1982.

[10] C. H. Bennett and G. Brassard, "Experimental quantum cryptography: the dawn of a new era for quantum cryptography: the experimental prototype is working," *SIGACT News,* vol. 20, pp. 78-80, 1989.

[11] A. R. Dixon, Z. L. Yuan, J. F. Dynes, A. W. Sharpe, and A. J. Shields, "Gigahertz decoy quantum key distribution with 1 Mbit/s secure key rate," *Optics Express,* vol. 16, pp. 18790-18979, 2008.

[12] P. A. Hiskett, D. Rosenberg, C. G. Peterson, R. J. Hughes, S. Nam, A. E. Lita*, et al.*, "Long-distance quantum key distribution in optical fibre," *New Journal of Physics,* vol. 8, p. 193, 2006.

[13] ID Quantique, *CERBERIS QUANTUM KEY DISTRIBUTION (QKD) SERVER*. Available: http://www.idquantique.com/network-encryption/products/cerberis-quantum-key-distribution.html

[14] MagiQ Technologies, *Quantum Key Distribution System (Q-Box)*. Available: http://www.magiqtech.com/Products.html

[15] Quintessence Labs, *qOpticaTM*. Available: http://quintessencelabs.com/qopticatm/

[16] Sequrenet, *Cygnus: State-of-the-art CVQKD module*. Available: http://www.sequrenet.com/products.html

[17] D. Knebel, P. Sanda, M. McManus, J. A. Kash, J. C. Tsang, D. Vallett*, et al.*, "Diagnosis and characterization of timing-related defects by time-dependent light emission," in *Test Conference, 1998. Proceedings., International*, pp. 733-739, 1998.

[18] M. Pavesi, P. L. Rigolli, M. Manfredi, P. Palestri, and L. Selmi, "Spontaneous hot-carrier photon emission rates in silicon: Improved modeling and applications to metal oxide semiconductor devices," *Physical Review B,* vol. 65, p. 195209, 2002.

[19] J. C. Tsang, J. A. Kash, and D. P. Vallett, "Picosecond imaging circuit analysis," *IBM Journal of Research and Development,* vol. 44, pp. 583-603, 2000.

[20] J. Bude, N. Sano, and A. Yoshii, "Hot-carrier luminescence in Si," *Physical Review B,* vol. 45, pp. 5848-5856, 1992.

[21] A. Korneev, A. Lipatov, O. Okunev, G. Chulkova, K. Smirnov, G. Gol'tsman*, et al.*, "GHz counting rate NbN single-photon detector for IR diagnostics of VLSI CMOS circuits," *Microelectronic Engineering,* vol. 69, pp. 274-278, 2003.

[22] R. H. Hadfield, "Single-photon detectors for optical quantum information applications," *Nat Photon,* vol. 3, pp. 696-705, 2009.

[23] Hamamatsu, *Photomultiplier Tubes: Basics and Applications, 3rd ed.* . Available: http://www.hamamatsu.com/resources/pdf/etd/PMT_handbook_v3aE.pdf

[24] GE Healthcare Life Sciences, *Typhoon FLA 9500*. Available: http://www.gelifesciences.com/webapp/wcs/stores/servlet/productById/en/GELifeSciences/28996943

[25] L. Q. Li and L. M. Davis, "Single photon avalanche diode for single molecule detection," *Review of Scientific Instruments,* vol. 64, pp. 1524-1529, 1993.

[26] X. Michalet, A. Ingargiola, R. A. Colyer, G. Scalia, S. Weiss, P. Maccagnani*, et al.*, "Silicon Photon-Counting Avalanche Diodes for Single-Molecule Fluorescence Spectroscopy," *Selected Topics in Quantum Electronics, IEEE Journal of,* vol. 20, pp. 1-20, 2014.

[27] E. Brooks Shera, N. K. Seitzinger, L. M. Davis, R. A. Keller, and S. A. Soper, "Detection of single fluorescent molecules," *Chemical Physics Letters,* vol. 174, pp. 553-557, 1990.

[28] G. S. Buller and A. M. Wallace, "Ranging and Three-Dimensional Imaging Using Time-Correlated Single-Photon Counting and Point-by-Point Acquisition," *Selected Topics in Quantum Electronics, IEEE Journal of,* vol. 13, pp. 1006-1015, 2007.

[29] A. Wehr and U. Lohr, "Airborne laser scanning—an introduction and overview," *ISPRS Journal of Photogrammetry and Remote Sensing,* vol. 54, pp. 68-82, 1999.

[30] A. McCarthy, X. Ren, A. Della Frera, N. R. Gemmell, N. J. Krichel, C. Scarcella*, et al.*, "Kilometer-range depth imaging at 1550 nm wavelength using an InGaAs/InP single-photon avalanche diode detector," *Optics Express,* vol. 21, pp. 22098-22113, 2013.

[31] A. McCarthy, N. J. Krichel, N. R. Gemmell, X. Ren, M. G. Tanner, S. N. Dorenbos, *et al.*, "Kilometer-range, high resolution depth imaging via 1560 nm wavelength single-photon detection," *Optics Express,* vol. 21, pp. 8904-8915, 2013.

[32] H. Iams and B. Salzberg, "The Secondary Emission Phototube," *Radio Engineers, Proceedings of the Institute of,* vol. 23, pp. 55-64, 1935.

[33] Hamamatsu, *Photomultiplier Tubes: Basics and Applications, 3rd ed.* . Available: http://www.hamamatsu.com/resources/pdf/etd/PMT_handbook_v3aE.pdf

[34] Hamamatsu, *Thermoelectric cooled NIR-PMT unit*. Available: http://www.hamamatsu.com/resources/pdf/etd/H10330B-25_-45_-75_TPMO1056E02.pdf

[35] J. Bardeen, L. N. Cooper, and J. R. Schrieffer, "Theory of Superconductivity," *Physical Review,* vol. 108, pp. 1175-1204, 1957.

[36] G. N. Gol'tsman, O. Okunev, G. Chulkova, A. Lipatov, A. Semenov, K. Smirnov, *et al.*, "Picosecond superconducting single-photon optical detector," *Applied Physics Letters,* vol. 79, pp. 705-707, 2001.

[37] S. P. Chockalingam, M. Chand, J. Jesudasan, V. Tripathi, and P. Raychaudhuri, "Superconducting properties and Hall effect of epitaxial NbN thin films," *Physical Review B,* vol. 77, p. 214503, 2008.

[38] MarsiliF, V. B. Verma, J. A. Stern, HarringtonS, A. E. Lita, GerritsT, *et al.*, "Detecting single infrared photons with 93% system efficiency," *Nat Photon,* vol. 7, pp. 210-214, 2013.

[39] T. Yamashita, S. Miki, K. Makise, W. Qiu, H. Terai, M. Fujiwara, *et al.*, "Origin of intrinsic dark count in superconducting nanowire single-photon detectors," *Applied Physics Letters,* vol. 99, p. 161105, 2011.

[40] A. Korneev, P. Kouminov, V. Matvienko, G. Chulkova, K. Smirnov, B. Voronov, *et al.*, "Sensitivity and gigahertz counting performance of NbN superconducting single-photon detectors," *Applied Physics Letters,* vol. 84, pp. 5338-5340, 2004.

[41] A. J. Kerman, E. A. Dauler, W. E. Keicher, J. K. W. Yang, K. K. Berggren, G. Gol'tsman, *et al.*, "Kinetic-inductance-limited reset time of superconducting nanowire photon counters," *Applied Physics Letters,* vol. 88, p. 111116, 2006.

[42] A. E. Lita, A. J. Miller, and S. W. Nam, "Counting near-infrared single-photons with 95% efficiency," *Optics Express,* vol. 16, pp. 3032-3040, 2008.

[43] D. Fukuda, G. Fujii, T. Numata, K. Amemiya, A. Yoshizawa, H. Tsuchida, *et al.*, "Titanium-based transition-edge photon number resolving detector with 98% detection efficiency with index-matched small-gap fiber coupling," *Optics Express,* vol. 19, pp. 870-875, 2011.

[44] D. Rosenberg, A. E. Lita, A. J. Miller, S. Nam, and R. E. Schwall, "Performance of photon-number resolving transition-edge sensors with integrated 1550 nm resonant cavities," *Applied Superconductivity, IEEE Transactions on,* vol. 15, pp. 575-578, 2005.

[45] D. Rosenberg, J. W. Harrington, P. R. Rice, P. A. Hiskett, C. G. Peterson, R. J. Hughes, *et al.*, "Long-Distance Decoy-State Quantum Key Distribution in Optical Fiber," *Physical Review Letters,* vol. 98, p. 010503, 2007.

[46] R. H. Haitz, "Model for the Electrical Behavior of a Microplasma," *Journal of Applied Physics,* vol. 35, pp. 1370-1376, 1964.

[47] M. Ghioni, A. Gulinatti, I. Rech, F. Zappa, and S. Cova, "Progress in Silicon Single-Photon Avalanche Diodes," *Selected Topics in Quantum Electronics, IEEE Journal of,* vol. 13, pp. 852-862, 2007.

[48] A. Lacaita, M. Ghioni, and S. Cova, "Double epitaxy improves single-photon avalanche diode performance," *Electronics Letters,* vol. 25, pp. 841-843, 1989.

[49] Micro Photon Devices, *PDM series*. Available: http://www.micro-photon-devices.com/Products/SPAD-by-Wavelength/400nm-900nm/PDM-PDF

[50] F. Zappa, S. Tisa, S. Cova, P. Maccagnani, D. B. Calia, R. Saletti, *et al.*, "Single-photon avalanche diode arrays for fast transients and adaptive optics," *Instrumentation and Measurement, IEEE Transactions on,* vol. 55, pp. 365-374, 2006.

[51] Excelitas Technologies Corp., *Single Photon Counting Modules (SPCM)*. Available: http://www.excelitas.com/Pages/Product/Single-Photon-Counting-Modules-SPCM.aspx

[52] Excelitas Technologies Corp., "C30902SH APD." Available: http://www.excelitas.com/Lists/APDs/DispForm.aspx?ID=10

[53] Y.-S. Kim, Y.-C. Jeong, S. Sauge, V. Makarov, and Y.-H. Kim, "Ultra-low noise single-photon detector based on Si avalanche photodiode," *Review of Scientific Instruments,* vol. 82, p. 093110, 2011.

[54] A. Rochas, M. Gani, B. Furrer, P. A. Besse, R. S. Popovic, G. Ribordy*, et al.*, "Single photon detector fabricated in a complementary metal–oxide–semiconductor high-voltage technology," *Review of Scientific Instruments,* vol. 74, pp. 3263-3270, 2003.

[55] C. Niclass, M. Sergio, and E. Charbon, "A Single Photon Avalanche Diode Array Fabricated in 0.35µm CMOS and based on an Event-Driven Readout for TCSPC Experiments," Proc. SPIE 6372, Advanced Photon Counting Techniques, 63720S, 2006.

[56] S. Tisa, F. Guerrieri, and F. Zappa, "Variable-load quenching circuit for single-photon avalanche diodes," *Optics Express,* vol. 16, pp. 2232-2244, 2008.

[57] S. Cova, M. Ghioni, A. Lacaita, C. Samori, and F. Zappa, "Avalanche photodiodes and quenching circuits for single-photon detection," *Applied Optics,* vol. 35, pp. 1956-1976, 1996.

[58] N. Faramarzpour, M. J. Deen, S. Shirani, and F. Qiyin, "Fully Integrated Single Photon Avalanche Diode Detector in Standard CMOS 0.18-µm Technology," *Electron Devices, IEEE Transactions on,* vol. 55, pp. 760-767, 2008.

[59] M. A. Marwick and A. G. Andreou, "Single photon avalanche photodetector with integrated quenching fabricated in TSMC 0.18 µm 1.8 V CMOS process," *Electronics Letters,* vol. 44, pp. 643-644, 2008.

[60] H. Finkelstein, M. J. Hsu, and S. C. Esener, "STI-Bounded Single-Photon Avalanche Diode in a Deep-Submicrometer CMOS Technology," *Electron Device Letters, IEEE,* vol. 27, pp. 887-889, 2006.

[61] J. A. Richardson, E. A. G. Webster, L. A. Grant, and R. K. Henderson, "Scaleable Single-Photon Avalanche Diode Structures in Nanometer CMOS Technology," *Electron Devices, IEEE Transactions on,* vol. 58, pp. 2028-2035, 2011.

[62] E. A. G. Webster, J. A. Richardson, L. A. Grant, D. Renshaw, and R. K. Henderson, "A Single-Photon Avalanche Diode in 90-nm CMOS Imaging Technology With 44% Photon Detection Efficiency at 690 nm," *Electron Device Letters, IEEE,* vol. 33, pp. 694-696, 2012.

[63] C. Niclass, A. Rochas, P. A. Besse, and E. Charbon, "Design and characterization of a CMOS 3-D image sensor based on single photon avalanche diodes," *Solid-State Circuits, IEEE Journal of,* vol. 40, pp. 1847-1854, 2005.

[64] F. Guerrieri, S. Tisa, A. Tosi, and F. Zappa, "Two-Dimensional SPAD Imaging Camera for Photon Counting," *Photonics Journal, IEEE,* vol. 2, pp. 759-774, 2010.

[65] M. Gersbach, Y. Maruyama, R. Trimananda, M. W. Fishburn, D. Stoppa, J. A. Richardson*, et al.*, "A Time-Resolved, Low-Noise Single-Photon Image Sensor Fabricated in Deep-Submicron CMOS Technology," *Solid-State Circuits, IEEE Journal of,* vol. 47, pp. 1394-1407, 2012.

[66] C. Veerappan, J. Richardson, R. Walker, L. Day-Uey, M. W. Fishburn, Y. Maruyama*, et al.*, "A 160×128 single-photon image sensor with on-pixel 55ps 10b time-to-digital converter," in *Solid-State Circuits Conference Digest of Technical Papers (ISSCC), 2011 IEEE International*, pp. 312-314, 2011.

[67] S. Marangoni, I. Rech, M. Ghioni, P. Maccagnani, M. Chiari, M. Cretich, *et al.*, "A 6×8 photon-counting array detector system for fast and sensitive analysis of protein microarrays," *Sensors and Actuators B: Chemical,* vol. 149, pp. 420-426, 2010.

[68] X. Michalet, R. A. Colyer, G. Scalia, A. Ingargiola, R. Lin, J. E. Millaud, *et al.*, *Development of new photon-counting detectors for single-molecule fluorescence microscopy* vol. 368, 2013.

[69] W. Haecker, O. Groezinger, and M. H. Pilkuhn, "Infrared Photon Counting by Ge Avalanche Diodes," *Applied Physics Letters,* vol. 19, pp. 113-115, 1971.

[70] A. Lacaita, P. A. Francese, F. Zappa, and S. Cova, "Single-photon detection beyond 1 µm: performance of commercially available germanium photodiodes," *Applied Optics,* vol. 33, pp. 6902-6918, 1994.

[71] Y. Kang, H. D. Liu, M. Morse, M. J. Paniccia, M. Zadka, S. Litski, *et al.*, "Monolithic germanium/silicon avalanche photodiodes with 340 GHz gain-bandwidth product," *Nat Photon,* vol. 3, pp. 59-63, 2009.

[72] Z. Lu, Y. Kang, C. Hu, Q. Zhou, H. D. Liu, and J. C. Campbell, "Geiger-Mode Operation of Ge-on-Si Avalanche Photodiodes," *Quantum Electronics, IEEE Journal of,* vol. 47, pp. 731-735, 2011.

[73] R. E. Warburton, G. Intermite, M. Myronov, P. Allred, D. R. Leadley, K. Gallacher, *et al.*, "Ge-on-Si Single-Photon Avalanche Diode Detectors: Design, Modeling, Fabrication, and Characterization at Wavelengths 1310 and 1550 nm," *Electron Devices, IEEE Transactions on,* vol. 60, pp. 3807-3813, 2013.

[74] K. Nishida, K. Taguchi, and Y. Matsumoto, "InGaAsP heterostructure avalanche photodiodes with high avalanche gain," *Applied Physics Letters,* vol. 35, pp. 251-253, 1979.

[75] J. C. Campbell, A. G. Dentai, W. S. Holden, and B. L. Kasper, "High-performance avalanche photodiode with separate absorption 'grading' and multiplication regions," *Electronics Letters,* vol. 19, pp. 818-820, 1983.

[76] A. Lacaita, F. Zappa, S. Cova, and P. Lovati, "Single-photon detection beyond 1 µm: performance of commercially available InGaAs/InP detectors," *Applied Optics,* vol. 35, pp. 2986-2996, 1996.

[77] G. Ribordy, J. D. Gautier, H. Zbinden, and N. Gisin, "Performance of InGaAs/InP avalanche photodiodes as gated-mode photon counters," *Applied Optics,* vol. 37, pp. 2272-2277, 1998.

[78] P. A. Hiskett, G. S. Buller, A. Y. Loudon, J. M. Smith, I. Gontijo, A. C. Walker, *et al.*, "Performance and design of InGaAs/InP photodiodes for single-photon counting at 1.55 µm," *Applied Optics,* vol. 39, pp. 6818-6829, 2000.

[79] D. Stucki, G. Ribordy, A. Stefanov, H. Zbinden, J. G. Rarity, and T. Wall, "Photon counting for quantum key distribution with peltier cooled InGaAs/InP APDs," *Journal of Modern Optics,* vol. 48, pp. 1967-1981, 2001.

[80] J. P. Donnelly, E. K. Duerr, K. A. McIntosh, E. A. Dauler, D. C. Oakley, S. H. Groves, *et al.*, "Design considerations for 1.06-µm InGaAsP-InP Geiger-mode avalanche photodiodes," *Quantum Electronics, IEEE Journal of,* vol. 42, pp. 797-809, 2006.

[81] S. Pellegrini, R. E. Warburton, L. J. J. Tan, N. Jo Shien, A. B. Krysa, K. Groom, *et al.*, "Design and performance of an InGaAs-InP single-photon avalanche diode detector," *Quantum Electronics, IEEE Journal of,* vol. 42, pp. 397-403, 2006.

[82] M. A. Itzler, r. Ben-Michael, C. F. Hsu, K. Slomkowski, A. Tosi, S. Cova, *et al.*, "Single photon avalanche diodes (SPADs) for 1.5 µm photon counting applications," *Journal of Modern Optics,* vol. 54, pp. 283-304, 2007.

[83] M. A. Itzler, X. Jiang, M. Entwistle, K. Slomkowski, A. Tosi, F. Acerbi, *et al.*, "Advances in InGaAsP-based avalanche diode single photon detectors," *Journal of Modern Optics,* vol. 58, pp. 174-200, 2011.

[84] N. Namekata, S. Sasamori, and S. Inoue, "800 MHz single-photon detection at 1550-nm using an InGaAs/InP avalanche photodiode operated with a sine wave gating," *Optics Express,* vol. 14, pp. 10043-10049, 2006.

[85] Y. Nambu, S. Takahashi, K. Yoshino, A. Tanaka, M. Fujiwara, M. Sasaki*, et al.*, "Efficient and low-noise single-photon avalanche photodiode for 1.244-GHz clocked quantum key distribution," *Optics Express,* vol. 19, pp. 20531-20541, 2011.

[86] G. S. Buller and R. J. Collins, "Single-photon generation and detection," *Measurement Science and Technology,* vol. 21, p. 012002, 2010.

[87] M. A. Itzler, X. Jiang, B. Nyman, and K. Slomkowski, "InP-based negative feedback avalanche diodes," in *Proc. SPIE 7222, Quantum Sensing and Nanophotonic Devices VI*, pp. 72221K-72221K-12, 2009.

[88] B. Korzh, N. Walenta, T. Lunghi, N. Gisin, and H. Zbinden, "Free-running InGaAs single photon detector with 1 dark count per second at 10% efficiency," *Applied Physics Letters,* vol. 104, p. 081108, 2014.

[89] A. Tosi, C. Scarcella, G. Boso, and F. Acerbi, "Gate-Free InGaAs/InP Single-Photon Detector Working at Up to 100 Mcount/s," *Photonics Journal, IEEE,* vol. 5, pp. 6801308-6801308, 2013.

[90] Micro Photon Devices, *InGaAs/InP*. Available: http://www.micro-photon-devices.com/Products/SPAD-by-Wavelength/900nm-1700nm/InGaAs-InP

[91] ID Quantique, *ID230 FREE RUNNING SINGLE PHOTON DETECTOR - NEAR INFRARED RANGE*. Available: http://www.idquantique.com/instrumentation.html

[92] S. Verghese, J. P. Donnelly, E. K. Duerr, K. A. McIntosh, D. C. Chapman, C. J. Vineis*, et al.*, "Arrays of InP-based Avalanche Photodiodes for Photon Counting," *Selected Topics in Quantum Electronics, IEEE Journal of,* vol. 13, pp. 870-886, 2007.

[93] Princeton Lightwave, *128 x 32 Geiger-mode Avalanche Photodiode (GmAPD) Camera*. Available: http://www.princetonlightwave.com/mm-products/3d-ladar/128-x-32-gmapd-camera

[94] Spectralab, *3D Geiger-mode LIDAR Camera*. Available: http://www.spectrolab.com/sensors/products/products.html

[95] J. C. Boisvert, G. S. Kinsey, D. McAlister, T. Isshiki, R. Sudharsanan, and M. Krainak, "Large-area InAlAs/InGaAs single-photon-counting avalanche photodiodes," in *Proc. SPIE 5412, Laser Radar Technology and Applications IX*, pp. 126-136, 2004.

[96] W. R. Clark, K. Vaccaro, and W. D. Waters, "InAlAs-InGaAs based avalanche photodiodes for next generation eye-safe optical receivers," in *Proc. SPIE 6796, Photonics North 2007*, pp. 67962H-67962H-15, 2007.

[97] "Self-quenching and self-recovering InGaAs/InAlAs single photon avalanche detector," *Appl. Phys. Lett.,* vol. 93, p. 153504, 2008.

[98] G. Karve, X. Zheng, X. Zhang, X. Li, S. Wang, F. Ma*, et al.*, "Geiger mode operation of an $In_{0.53}Ga_{0.47}As$-$In_{0.52}Al_{0.48}As$ avalanche photodiode," *Quantum Electronics, IEEE Journal of,* vol. 39, pp. 1281-1286, 2003.

[99] T. Nakata, E. Mizuki, T. Tsukuda, S. Takahashi, H. Hatakeyama, T. Anan*, et al.*, "InAlAs avalanche photodiodes for gated Geiger mode single photon counting," in *OptoElectronics and Communications Conference (OECC), 2010 15th*, pp. 822-823, 2010.

[100] M. A. Diagne, M. Greszik, E. K. Duerr, J. J. Zayhowski, M. J. Manfra, R. J. Bailey*, et al.*, "Integrated array of 2-µm antimonide-based single-photon counting devices," *Optics Express,* vol. 19, pp. 4210-4216, 2011.

[101] B. M. Onat, K. Slomkowski, and M. Itzler, "Extended wavelength InGaAs-Based avalanche photodiodes for single photon counting applications," in *Photonics Conference (IPC), 2012 IEEE*, pp. 96-97, 2012.

[102] J. P. R. David and C. H. Tan, "Material Considerations for Avalanche Photodiodes," *Selected Topics in Quantum Electronics, IEEE Journal of,* vol. 14, pp. 998-1009, 2008.

[103] Y. L. Goh, D. J. Massey, A. R. J. Marshall, J. S. Ng, C. H. Tan, W. K. Ng*, et al.*, "Avalanche Multiplication in InAlAs," *Electron Devices, IEEE Transactions on,* vol. 54, pp. 11-16, 2007.

[104] L. J. J. Tan, D. S. G. Ong, N. Jo Shien, T. Chee Hing, S. K. Jones, Q. Yahong*, et al.*, "Temperature Dependence of Avalanche Breakdown in InP and InAlAs," *Quantum Electronics, IEEE Journal of,* vol. 46, pp. 1153-1157, 2010.

[105] M. Lahrichi, G. Glastre, E. Derouin, D. Carpentier, N. Lagay, J. Decobert*, et al.*, "240-GHz Gain-Bandwidth Product Back-Side Illuminated AlInAs Avalanche Photodiodes," *Photonics Technology Letters, IEEE,* vol. 22, pp. 1373-1375, 2010.

[106] C. Lenox, H. Nie, P. Yuan, G. Kinsey, A. L. Homles, Jr., B. G. Streetman*, et al.*, "Resonant-cavity InGaAs-InAlAs avalanche photodiodes with gain-bandwidth product of 290 GHz," *Photonics Technology Letters, IEEE,* vol. 11, pp. 1162-1164, 1999.

[107] N. Li, R. Sidhu, X. Li, F. Ma, X. Zheng, S. Wang*, et al.*, "InGaAs/InAlAs avalanche photodiode with undepleted absorber," *Applied Physics Letters,* vol. 82, pp. 2175-2177, 2003.

[108] E. Yagyu, E. Ishimura, M. Nakaji, T. Aoyagi, K. Yoshiara, and Y. Tokuda, "Investigation of guardring-free planar AlInAs avalanche photodiodes," *Photonics Technology Letters, IEEE,* vol. 18, pp. 1264-1266, 2006.

[109] A. Rouvie, D. Carpentier, N. Lagay, J. Decobert, F. Pommereau, and M. Achouche, "High Gain × Bandwidth Product Over 140-GHz Planar Junction AlInAs Avalanche Photodiodes," *Photonics Technology Letters, IEEE,* vol. 20, pp. 455-457, 2008.

[110] X. G. Zheng, J. S. Hsu, J. B. Hurst, X. Li, S. Wang, X. Sun*, et al.*, "Long-wavelength $In_{0.53}Ga_{0.47}As$-$In_{0.52}Al_{0.48}As$ large-area avalanche photodiodes and arrays," *Quantum Electronics, IEEE Journal of,* vol. 40, pp. 1068-1073, 2004.

[111] J. C. Boisvert, A. Masalykin, G. S. Kinsey, T. Isshiki, M. Haddad, R. Sudharsanan*, et al.*, "Characterization of InAlAs/InGaAs APD arrays for SWIR imaging applications," in *Proc. SPIE 5406, Infrared Technology and Applications XXX*, pp. 13-20, 2004.

[112] Voxtel. Inc., *InGaAs APD Detector Arrays*. Available: http://voxtel-inc.com/products/single-element-detectors-and-pixelated-detector-arrays/

[113] OptoGration Inc., *InGaAs APD array*. Available: http://www.optogration.com/array_products.htm

[114] S. C. Liew Tat Mun, C. H. Tan, S. J. Dimler, L. J. J. Tan, J. S. Ng, Y. L. Goh*, et al.*, "A Theoretical Comparison of the Breakdown Behavior of $In_{0.52}Al_{0.48}As$ and InP Near-Infrared Single-Photon Avalanche Photodiodes," *Quantum Electronics, IEEE Journal of,* vol. 45, pp. 566-571, 2009.

[115] S. Wang, F. Ma, X. Li, G. Karve, X. Zheng, and J. C. Campbell, "Analysis of breakdown probabilities in avalanche photodiodes using a history-dependent analytical model," *Applied Physics Letters,* vol. 82, pp. 1971-1973, 2003.

[116] D. A. Ramirez, M. M. Hayat, G. Karve, J. C. Campbell, S. N. Torres, B. E. A. Saleh*, et al.*, "Detection efficiencies and generalized breakdown probabilities for nanosecond-gated near infrared single-photon avalanche photodiodes," *Quantum Electronics, IEEE Journal of,* vol. 42, pp. 137-145, 2006.

[117] A. Filler, "The History, Development and Impact of Computed Imaging in Neurological Diagnosis and Neurosurgery: CT, MRI, and DTI," in *Nature Precedings*, 2009.

[118] NASA, Goddard Space Flight Center, *Imagine the universe*. Available: http://imagine.gsfc.nasa.gov/science/toolbox/emspectrum1.html

[119] Anritsu, *HD X-Ray Inspection Systems*. Available: http://www.us.anritsu-industry.com/x-ray-inspection.aspx

[120] J. D. Watson and F. H. C. Crick, "Molecular Structure of Nucleic Acids: A Structure for Deoxyribose Nucleic Acid," *Nature,* vol. 171, pp. 737-738, 1953.

[121] S. Del Sordo, L. Abbene, E. Caroli, A. M. Mancini, A. Zappettini, and P. Ubertini, "Progress in the Development of CdTe and CdZnTe Semiconductor Radiation Detectors for Astrophysical and Medical Applications," *Sensors,* vol. 9, pp. 3491-3526, 2009.

[122] A. Owens and A. Peacock, "Compound semiconductor radiation detectors," *Nuclear Instruments and Methods in Physics Research Section A: Accelerators, Spectrometers, Detectors and Associated Equipment,* vol. 531, pp. 18-37, 2004.

[123] Ioffe Institute, *Indium Arsenide*. Available: http://www.ioffe.ru/SVA/NSM/Semicond/InAs/

[124] T. Takahashi, T. Mitani, Y. Kobayashi, M. Kouda, G. Sato, S. Watanabe*, et al.*, "High-resolution Schottky CdTe diode detector," *Nuclear Science, IEEE Transactions on,* vol. 49, pp. 1297-1303, 2002.

[125] A. K. Khusainov, A. L. Dudin, A. G. Ilves, V. F. Morozov, A. K. Pustovoit, and R. D. Arlt, "High performance p–i–n CdTe and CdZnTe detectors," *Nuclear Instruments and Methods in Physics Research Section A: Accelerators, Spectrometers, Detectors and Associated Equipment,* vol. 428, pp. 58-65, 1999.

[126] Amptek, *XR-100T-CdTe X-Ray & Gamma Ray Detector*. Available: http://www.amptek.com/products/xr-100t-cdte-x-ray-and-gamma-ray-detector/

[127] Oy AJAT Ltd., *ART Plus Panoramic Imaging System*. Available: http://www.ajat.fi/product/art-plus-panoramic-imaging-system/

[128] A. W. Webb, S. B. Qadri, E. R. Carpenter, E. F. Skelton, and J. Kennedy, "Effects of pressure on $Cd_{1-x}Zn_xTe$ alloys ($0 \leq x < 0.5$)," *Journal of Applied Physics,* vol. 61, pp. 2492-2494, 1987.

[129] A. Niemela and H. Sipila, "Evaluation of CdZnTe detectors for soft X-Ray applications," *Nuclear Science, IEEE Transactions on,* vol. 41, pp. 1054-1057, 1994.

[130] A. Owens, M. Bavdaz, H. Andersson, T. Gagliardi, M. Krumrey, S. Nenonen*, et al.*, "The X-ray response of CdZnTe," *Nuclear Instruments and Methods in Physics Research Section A: Accelerators, Spectrometers, Detectors and Associated Equipment,* vol. 484, pp. 242-250, 2002.

[131] D. S. McGregor and H. Hermon, "Room-temperature compound semiconductor radiation detectors," *Nuclear Instruments and Methods in Physics Research Section A: Accelerators, Spectrometers, Detectors and Associated Equipment,* vol. 395, pp. 101-124, 1997.

[132] D. S. McGregor, A. J. Antolak, H. C. Chui, E. S. Cross, Z. Q. Fang, M. S. Goorsky*, et al.*, "The investigation of custom grown vertical zone melt semi-insulating bulk gallium arsenide as a radiation spectrometer," in *Nuclear Science Symposium and Medical Imaging Conference Record, 1995., 1995 IEEE,* pp. 85-89 vol.1, 1995.

[133] C. Schwarz, M. Campbell, R. Goeppert, E. H. M. Heijne, J. Ludwig, G. Meddeler*, et al.*, "X-ray imaging using a hybrid photon counting GaAs pixel detector," *Nuclear Physics B - Proceedings Supplements,* vol. 78, pp. 491-496, 1999.

[134] L. Tlustos, G. Shelkov, and O. P. Tolbanov, "Characterisation of a GaAs(Cr) Medipix2 hybrid pixel detector," *Nuclear Instruments and Methods in Physics Research Section A: Accelerators, Spectrometers, Detectors and Associated Equipment,* vol. 633, Supplement 1, pp. S103-S107, 2011.

[135] M. C. Veale, S. J. Bell, D. D. Duarte, M. J. French, A. Schneider, P. Seller*, et al.*, "Chromium compensated gallium arsenide detectors for X-ray and γ-ray spectroscopic imaging," *Nuclear Instruments and Methods in Physics Research Section A: Accelerators, Spectrometers, Detectors and Associated Equipment,* vol. 752, pp. 6-14, 2014.

[136] A. Owens, M. Bavdaz, A. Peacock, A. Poelaert, H. Andersson, S. Nenonen*, et al.*, "Hard X-ray spectroscopy using small format GaAs arrays," *Nuclear Instruments and Methods in Physics Research Section A: Accelerators, Spectrometers, Detectors and Associated Equipment,* vol. 466, pp. 168-173, 2001.

[137] A. Owens, M. Bavdaz, A. Peacock, H. Andersson, S. Nenonen, M. Krumrey, *et al.*, "High resolution X-ray spectroscopy using a GaAs pixel detector," *Nuclear Instruments and Methods in Physics Research Section A: Accelerators, Spectrometers, Detectors and Associated Equipment,* vol. 479, pp. 531-534, 2002.

[138] P. Kostamo, S. Nenonen, S. Vähänen, L. Tlustos, C. Fröjdh, M. Campbell, *et al.*, "GaAs Medipix2 hybrid pixel detector," *Nuclear Instruments and Methods in Physics Research Section A: Accelerators, Spectrometers, Detectors and Associated Equipment,* vol. 591, pp. 174-177, 2008.

2 Background theory

2.1 Impact ionisation

Impact ionisation is a key process in APDs, during which energetic carriers (electrons or holes) collide with the lattice creating EHPs. In this process, an energetic electron (or hole) impart its energy to an electron in the valance band and promote it to the conduction band leaving a new hole in the valance band. As shown in Figure 2-1, the photo-generated electron and hole (primary carriers) are accelerated under the applied electric field and directed to n- and p- layer respectively. During their travel in the i-layer (high electric field region), both of them generate a new EHP (secondary carriers) through impact ionisation. Both the primary and secondary carriers are swept to the electrodes resulting an internal gain of 3. This internal gain is known as multiplication factor or avalanche gain.

The minimum energy gained by carriers to enable an impact ionisation is referred as threshold energy, E_{th}. E_{th} is larger than the bandgap of the in order to conserve energies and momentum of the carriers involved. The impact ionisation process is often described by the impact ionisation coefficients (denoted as α and β for electron and hole respectively), which are the mean number of EHPs created by the primary carrier per unit travelled length. Ionisation coefficients are dependent on material, electric field and temperature.

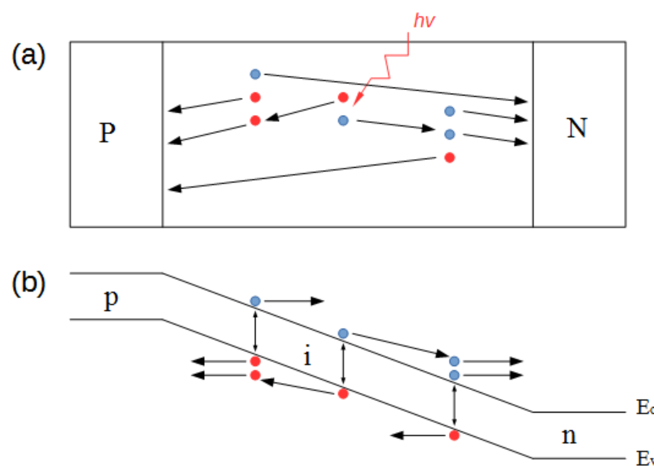

Figure 2-1 Illustration of impact ionisation process in (a) a reverse biased PIN diode and (b) the corresponding energy band transition.

2.2 Avalanche gain and excess noise

It has been shown in section 2.1 that a chain of impact ionisations in an APD result in avalanche multiplication gain. The multiplication gain is related to ionisation coefficients which are position dependent when the electric field is not uniform. The mean multiplication factor, M, can be expressed in relation to ionisation coefficients by solving current continuity function [1]

$$M(x) = \frac{\exp\left(-\int_0^x [\alpha(x') - \beta(x')]dx'\right)}{1 - \int_0^w \alpha(x') \exp\left(-\int_0^{x'} [\alpha(x'') - \beta(x'')]dx''\right) dx'}, \qquad (2\text{-}1)$$

where the primary carrier is generated in a depletion region with thickness of w and at position x.

For an ideal p-i-n diode, the electric field in i-layer is constant, so the ionisation coefficients are no longer dependent on electric field and hence the position. This expression then can be simplified as:

$$M(x) = \frac{(\alpha - \beta)\exp[-(\alpha - \beta)x]}{\alpha \exp[-(\alpha - \beta)w] - \beta}. \qquad (2\text{-}2)$$

Furthermore, it can be seen that when $\alpha>\beta$, $M(x)$ decreases with x; and when $\alpha<\beta$, $M(x)$ increases with x. This gives us two special cases where maximum multiplication gain is achieved: $x = 0$ (pure electron injection) and $x = w$ (pure hole injection) when $\alpha>\beta$ and $\alpha<\beta$ respectively.

Due to the intrinsically random nature of impact ionisation process, avalanche multiplication has a distribution around a mean gain value, M. This adds additional noise other than shot noise which is due to the random motion of discrete charge carriers. McIntyre [2] has shown that the mean square noise current spectral density is

$$\langle i^2 \rangle = 2qI_{pr}M^2F, \qquad (2\text{-}3)$$

where I_{pr} is the primary current, F is the excess noise factor used to characterise the avalanche noise and given by

$$F = \frac{\langle M^2 \rangle}{M^2}. \tag{2-4}$$

McIntyre's work also has also shown that F can be expressed as a function of M and the ratio of ionisation coefficients ($k = \beta/\alpha$) assuming that ionisation coefficients depend only on local electric field and k is constant. The expression is given as

$$F = k_{eff}M + (1 - k_{eff})(2 - \frac{1}{M}), \tag{2-5}$$

where $k_{eff} = k = \beta/\alpha$ for pure electron injection and $k_{eff} = 1/k = \alpha/\beta$ for pure hole injection. From the above equation, it can be seen that in order to achieve lowest excess noise the ionisation coefficient need to be as dissimilar as possible and the initiating carrier should have larger ionisation coefficient.

2.3 SPAD principle of operation

2.3.1 Operation mode of APDs

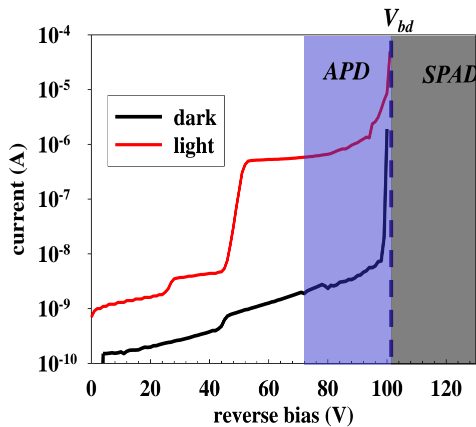

	APD	SPAD
Operation mode	Linear mode	Geiger mode
Voltage	$<V_{bd}$	$>V_{bd}$
Gain	<1000	$>10^6$
Single photon sensitivity	No	Yes

Figure 2-2 Left: typical I-V (in dark or under illumination) of an APD showing different operation modes. Right: comparison of APD and SPAD.

As Figure 2-2 shown, APDs can be operated in either linear mode (APDs) or Geiger mode (SPADs) depending on the applied voltage. In linear mode, a reverse bias less than V_{bd} is applied to the diode and an avalanche gain <1000 is obtained as the results of a series of impact ionisation process. However, this gain is not enough for detection of light in single photon level unless additional high-gain amplifiers with low noise are used. Geiger mode APDs (SPAD) operate above the breakdown voltage having large enough gain for single photon sensitivity. The gain is so high (infinity) that a single primary carrier could produce a macroscopic avalanche current which can be detected by the

readout circuit. However, the large avalanche current is self-sustaining which will destroy the diode due to excessive heat. Therefore a quenching circuit is required to reduce the applied bias to be below V_{bd} and stops the avalanche current.

Figure 2-3(a) shows a passive quenching circuit (PQC), the most basic form of quenching circuits. A DC voltage, which is larger than the V_{bd}, is applied to the SPAD through a ballast resistor, R_B. When an avalanche event occurs, there is a large avalanche current flowing through the SPAD and the ballast resistor. The avalanche current results in a voltage drop across the ballast resistor reducing the bias voltage across the SPAD. This negative feedback, with large enough R_B, can terminate the avalanche current. During the avalanche event, a 50 Ω resistor, impedance matched with coaxial cable and input terminal of the readout circuit, gives a potential drop (V_{out}) which could be sensed by readout circuit. After the avalanche current is quenched, the bias voltage across the SPAD increases back to the DC voltage and the SPAD is ready for next avalanche event, which is known as the recharging process. The recharge time is determined by the time constant $C_t R_B$, where C_t is the total capacitance including the SPAD capacitance and any parasitic capacitance in the setup. However, in order to quench the avalanche current effectively R_B usually has a large value (> 100 kΩ), which has the undesirable effect of a long recharge time and hence small maximum count rate.

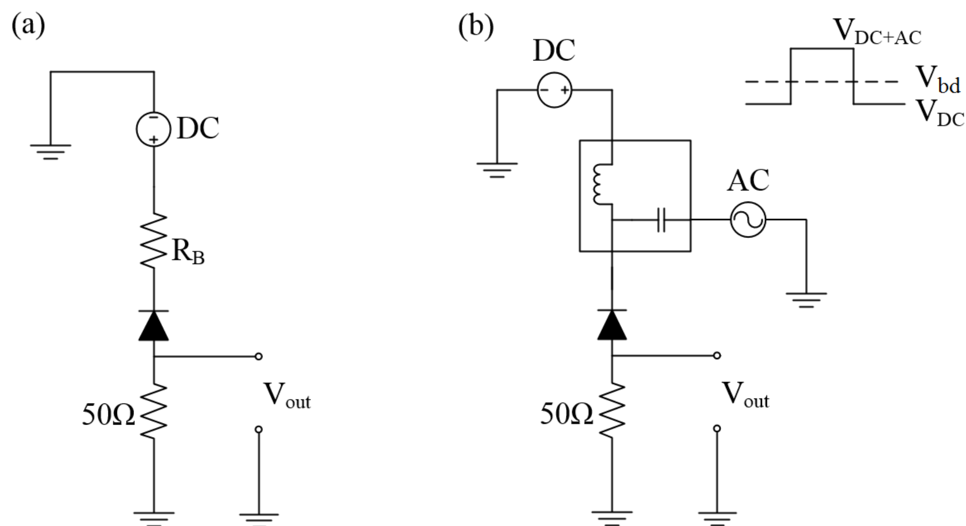

Figure 2-3 schematic of (a) a passive quenching circuit and (b) a gated quenching circuit.

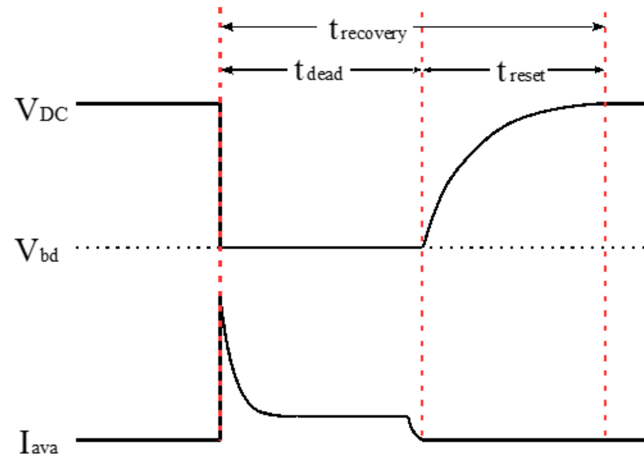

Figure 2-4 Bias voltage and avalanche current (I_{ava}) in a SPAD quenched by a PQC during an avalanche event.

Figure 2-4 shows how the voltage and current change with time during an avalanche event in a SPAD quenched by a PQC circuit. When an avalanche event is triggered, the avalanche current build up quickly. The large current causes a potential drop across the ballast resistor, which brings the bias voltage down and quenches the avalanche current. During this time, the SPAD is not sensitive to any incoming photons, known as dead time (t_{dead}). After the avalanche is quenched, the bias voltage increases back to V_{DC} with a reset time (t_{reset}) determined by ballast resistor and total capacitance across the SPAD. It worth noting that during t_{reset} the bias voltage increases from V_{bd} to V_{DC} and the SPAD is capable of detecting single photons with an increasing probability. The time required to recover the bias voltage back to V_{DC} is the recovery time, $t_{recovery}$. For quenching methods giving a very fast reset time, $t_{recovery}$ is approximately the same with t_{dead}, and they are usually used interchangeably.

Gated quenching circuit shown in Figure 2-3(b) is preferred when the incoming photons have known and periodic arrival time. The gated operation is realised by biasing the SPAD with a DC voltage ($V_{DC} < V_{bd}$) superimposed with AC pulses so that ($V_{DC} + V_{AC}$) > V_{bd}. Thus the SPAD is active only when the total bias is above V_{bd} (on-time). If an avalanche event occurs during the on-time, the falling edge of the AC pulse will quench the avalanche current. The AC pulse is usually kept short (several ns), so the dark count rate is reduced since the SPAD is active only during the on time. The frequency of the AC pulses can be kept low to effectively give a long off-time reducing the afterpulsing effect. One main disadvantage of gated quenching is that it cannot be used in applications

in which incoming photons have random arrival time. The circuit can be used in combination with passive quenching circuit by including R_B in series with the SPAD.

Other more sophisticated quenching circuits, such as active quenching circuit (AQC) and capacitive quenching circuit (CQC), have been also investigated [3, 4]. AQC uses active components to sense the rising edge of the avalanche current, reduce the bias voltage rapidly terminating the avalanche current and then reset the bias voltage back to be above breakdown voltage. AQC has fast quenching and recharging time, however, it is more complex than other quenching circuits. CQC uses a capacitor instead of a resistor to quenching the avalanche current. Fast quenching and clean square AC bias can be obtained.

2.3.2 Single Photon Detection Efficiency

Single photon detection efficiency is defined as the ratio of the number of avalanche pulses triggered by photo-generated carriers and the number of incident photons (in single photon level). For SPADs with SAMAPD structure, which is the case studied in this work, *SPDE* is the product of absorption efficiency, collection efficiency and breakdown probability,

$$SPDE = P_{abs} \times (1 - P_{loss}) \times P_b, \qquad (2\text{-}6)$$

where P_{loss} is the probability that photo-generated carriers are lost before entering the avalanche layer.

Absorption efficiency, P_{abs}, is the probability of an photon being absorbed in the absorption layer, which can be calculated as $P_{abs} = 1\text{-}exp(-\alpha_{abs} \times w_{abs})$, where α_{abs} is the absorption coefficient and w_{abs} is the width of absorption layer. The exponential term indicates that the percentage of the remaining photon flux decays exponentially with the distance and with a rate determined by α_{abs}. Absorption coefficient is related to the wavelength of the light and material of the absorption layer. Thick absorption layer is desirable to achieve high P_{abs} and hence high *SPDE*.

Collection efficiency is the probability that the photo-generated carriers travel to the multiplication layer without being trapped or recombined. This comes from the fact that SPADs with SAMAPD structure has a heterojunction between the absorption and multiplication layers which might cause carrier trapping reducing the *SPDE*. A grading

layer with intermediate bandgap value between those of the absorption and multiplication layer is usually used to reduce the band discontinuity.

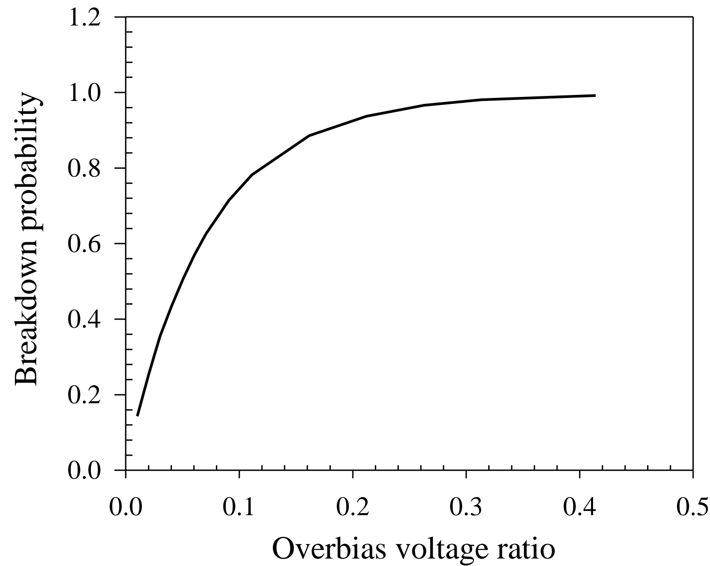

Figure 2-5 Breakdown probability of an InAlAs SPAD with 0.1 μm thick multiplication layer versus overbias voltage ratio.

Breakdown probability is the probability of having an avalanche breakdown triggered by a carrier in the multiplication layer. P_b is usually expressed as a function of overbias voltage ratio, which is defined as $(V_b$-$V_{bd})/V_{bd}$. P_b increases from zero at V_{bd} and saturates to one for $V_b << V_{bd}$. Figure 2-5 shows the calculated P_b as a function of over bias ratio for an InAlAs SPAD with 0.1 μm thick multiplication layer.

2.3.3 Dark count rate

Dark count rate is the rate of avalanche events (dark counts) triggered by carriers generated in absence of light. Readout circuit normally is unable to distinguish between the avalanche events from light and dark, so dark counts will result in false counts reducing the usefulness of the SPAD in applications. There are three main dark carrier generation mechanisms that contribute to dark count: thermal generation, tunnelling current and carrier re-emission of trapped carriers [5]. The last one is known as the cause of afterpulsing effect and will be discussed in section 2.3.4.

Thermal generation current is generated from the Shockley-Read-Hall process. The generation rate can be expressed as n_i/τ, where n_i is the intrinsic carrier concentration and

τ is the generation carrier lifetime which is related to the material quality [6]. Thermal generation usually occurs through local energy levels introduced by defects. Since energy levels located within the bandgap act as generation centres, energy required to thermally excite an electron from valance band to conduction band is effectively reduced. So the density of the defects in the material affects the generation carrier lifetime and thermal generation rate. For III-V SPADs, thermal generation current from the absorption layer, which is normally made of narrow bandgap material, is dominant. Cooling the SPAD can reduce the thermal generation current by reducing n_i.

Since SPAD needs to be operated above breakdown voltage, the electric field in multiplication layer might be so high that band-to-band (BTB) tunnelling becomes significant. Under very high electric field, the potential barrier that an electron has to across from valance to conduction band becomes narrower resulting in BTB tunnelling with a certain probability. At lower electric field, tunnelling current can still be significant with the assistance of defects with energy level in the bandgap. This is known as trap-assisted tunnelling (TAT), which is significantly influenced by the position and density of the defects, which are in turn related to by improving the quality of the material [7]. Both tunnelling mechanisms are weakly dependent on temperature.

Similar with *SPDE*, *DCR* also increases with overbias voltage due to the increase of breakdown probability. Therefore a trade-off always exists between achieving high *SPDE* and low *DCR*.

2.3.4 Afterpulsing

Afterpulsing effect describes the process that a carrier trapped during one avalanche event by a defect is subsequently released and triggers an additional avalanche event (dark count). Afterpulsing effect introduces additional dark counts hence also known as secondary dark counts [3].

The carriers are trapped by the deep level defects in the material and the time taken before they are released is described by an exponential time constant depending on the type of defects. The afterpulsing effect can be reduced by minimising the number of carriers flowing through the diode during the avalanche event. This can be achieved by using a fast quenching technique such as CQC and/or quenching by a very narrow gate.

Lower overbias voltage also reduces the total carriers, however, at the price of lower *SPDE*.

Another method to suppress the afterpulsing effect is to introduce a hold-off time (applied voltage is lower than V_b) after an avalanche event. During this hold-off time, the trapped carriers get released without triggering new avalanche pulses. Hence longer hold-off time reduces the severity of the afterpulse effect. However, this method reduces the maximum operating rate of the SPAD. Afterpulsing also becomes more severe when the detector is cooled since the release process of the trapped carriers become slower at lower temperature.

2.3.5 Timing jitter

Timing jitter is the fluctuation of time between photon arrival and detection of the avalanche pulse triggered by the incident photon. The main fluctuation comes from the variation in build-up time of avalanche pulses as a result of stochastic nature of avalanche process. The fluctuation of build-up time decreases with increasing overbias voltage. This is due to the less spread of ionisation path length probability density function (pdf), which directly affect the level of fluctuation in the avalanche process [8].

Another source of the timing jitter is the difference in the time taken by photo-generated carriers to travel from absorption layer to the avalanche layer, which depends on the positon of photon absorption. When the absorption layer is not fully depleted, carriers generated in undepleted region need to diffuse to the avalanche layer. In this case the uncertainty of diffusion time might be a significant component of the timing jitter.

In terms of timing jitter of the system, jitter of the photon arrival time and RC limit of the circuit and diode also contribute to the total timing jitter. The jitter of photon arrival time is determined by the pulse width of the pulse laser which is usually defined by *FWHM* of the duration time. The RC limit is set by the product of C_t and $R_d + R_{load}$, where R_d is the diode resistance and R_{load} is the load resistance of the readout circuit [3].

2.4 Background of radiation detection

2.4.1 Interaction of X-rays with matters

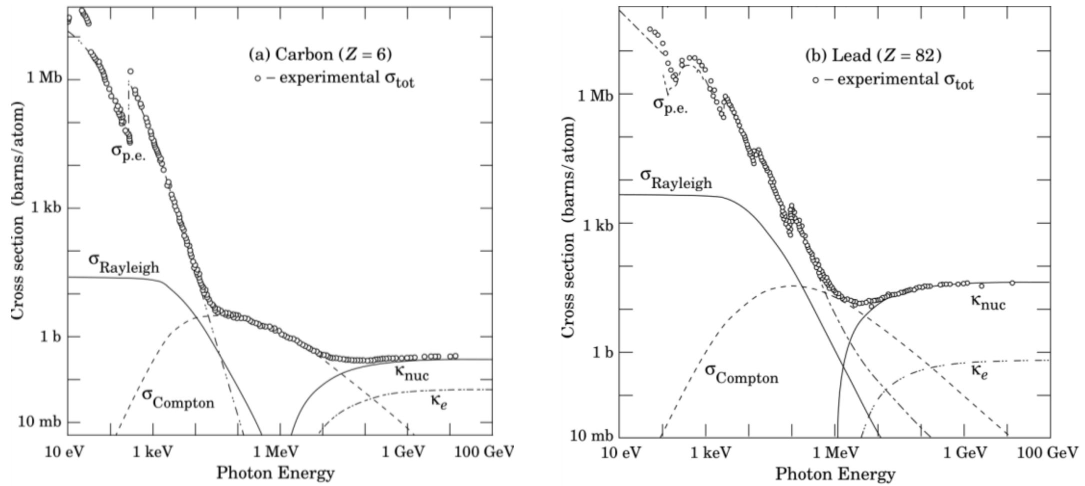

Figure 2-6 Energy dependence of different interactions for carbon and lead [9].

When X-ray photons are passing through matters, three main interactions will occur namely photoelectric effect, Compton scattering and pair creation. X-ray photons will transfer energy to bound electrons, partially or completely depending on the type of interaction, though these interactions. However, the probability (or sometimes called cross-sections) that each interaction occurs is different depending on the photon energy and material properties. Figure 2-6 shows the probability of different interactions as a function of photon energy in carbon and lead. Pair creation is the process that photon energy is converted into an electron-positron pair. The interaction usually occurs when the photon energy is in MeV range, because the equivalent energy to twice the rest mass energy of an electron is 1.02 MeV [10]. In Compton scattering, part of its energy is transferred to an electron through collision between them. After the collision the photon is usually deflected by an angle, θ, which determines the amount of transferred energy. In contrast, photoelectric effect requires the incoming X-ray photon to transfer all of the photon energy to an electron, which makes it is preferred when the X-ray detector is used in X-ray spectroscopy. In this thesis, GaAs and InAs will be used to detect X-rays in soft X-ray range where photoelectric effect is the major interaction, so details of photon electric effect will be discussed in the following section.

2.4.2 Photoelectric effect

In the interaction caused by photoelectric effect, a bound electron will be ejected with kinetic energy given by hv - E_{bind}, where hv is the photon energy and E_{bind} is the binding energy of the electron, resulting a photoelectron shown in Figure 2-7(a). Since photon energy has to be higher than the binding energy of the electrons at different shells, the probability of occurring photoelectric effect ($\sigma_{p.e.}$) drops abruptly when the photon energy is slightly lower than the binding energy resulting "absorption edges" shown in Figure 2-5. The probability of photoelectric effect also decreases rapidly with the photon energy. Moreover, it increases with atomic number (Z) of the absorption material, as shown in Figure 2-5 that for a given photon energy, photoelectric effect is more likely to take place in lead ($Z = 82$) than carbon ($Z = 6$). This relationship can be expressed as [10]:

$$\sigma_{p.e.} \cong A \times \frac{Z^n}{(hv)^{3.5}}, \qquad (2\text{-}7)$$

where n is a constant that has a value between 4 to 5 and A is a constant independent of Z and hv.

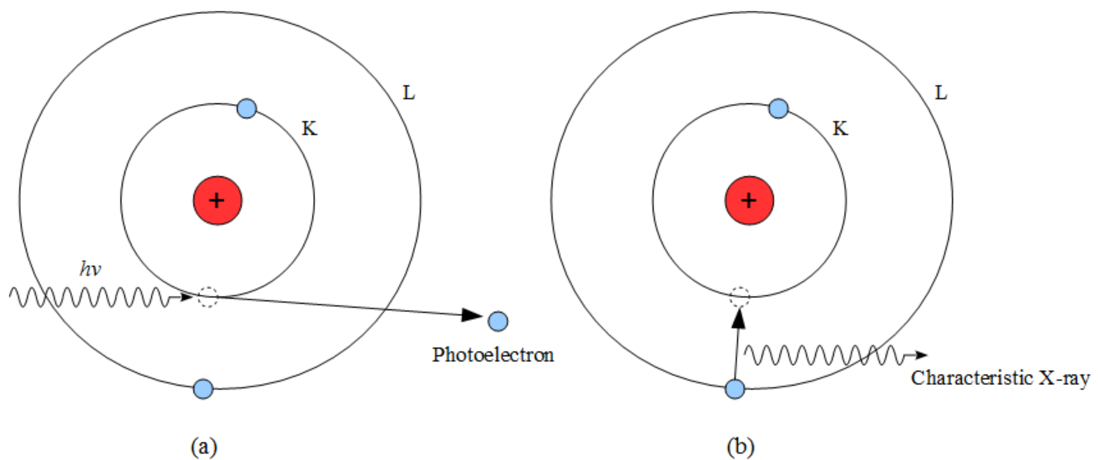

Figure 2-7 (a) Photoelectric effect in an atom. (b) Generation of characteristic X-ray.

The ejection of the photoelectron leaves an ionised atom with a vacancy. This vacancy might be filled by an electron from outer shell to stabilise the atom. Meanwhile, the energy difference between the two shells can be released in form of photons known as characteristic X-rays. The process of generating characteristic X-rays is shown in Figure 2-7(b). Although in most cases characteristic X-rays will be absorbed by subsequent photoelectric effect, some of them might escape from the surface of the

detector resulting in escape peaks. The energy of the escape peaks is given by the difference between energy of the incident photon and the escaped characteristic X-ray.

2.4.3 Energy resolution

In the spectroscopy measurement, the height distribution of pulses produced in detectors provides an energy spectrum of the incident photons. Ideally a delta-like peak spectrum is expected for radiation of fixed energy. However the measured peak is a wider Gaussian-shape peak due to the fluctuations of pulse height. This fluctuation is the end result of the fluctuations in the number of carriers collected by the readout circuit.

Energy resolution is an importance characteristics of the radiation detector showing the limit of distinguishing two closely spaced energy peaks. The energy resolution (E_R) is defined as the ratio of the *FWHM* of the energy peak to the centroid energy of the peak (E_C), $E_R = \frac{FWHM}{E_C}$. Figure 2-8 shows the *FWHM* of a typical Gaussian function. The relationship between the FWHM and standard deviation of the Gaussian function (σ) is $FWHM = 2.36\sigma$.

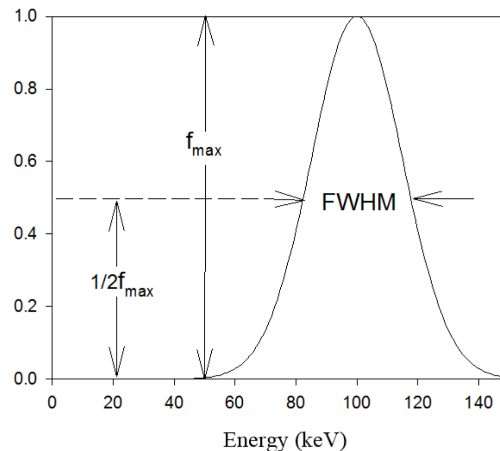

Figure 2-8 Example of energy spectrum with peak energy E_C = 100 keV. f_{mas} is the maximum amplitude of the Gaussian peak.

2.4.4 Absorption efficiency

When a beam of monoenergetic photons is passing through the detector, the intensity of the photons, $I(x)$, at distance x has an exponential expression as follow:

$$I(x) = I_0 \exp(-\varphi \times \rho \times x), \tag{2-8}$$

where I_0 is the incident intensity, φ is the mass attenuation coefficient of the material and ρ is the density of the material. The mass attenuation coefficient is proportional to $\sigma_{p.e.}$ which increases with Z rapidly (4th or 5th power of Z) [11]. Hence materials with high Z are desirable for high energy radiation detection. In addition, material with high Z can also increase the attenuation probability per distance. The absorption efficiency of a detector with thickness of w is given by

$$P(w) = 1 - \exp(-\varphi \times \rho \times w). \quad (2\text{-}9)$$

2.4.5 Fano factor

Ideally full photon energy is completely converted into EHPs and the number of EHPs produced by each absorbed photon do not vary. In reality, a finite amount of the photon energy is lost by mechanisms other than EHPs creation process (e.g. scattering with lattices) leading to a statistical fluctuation of the number of EHPs generated. The distribution of the EHPs numbers generated from a given X-ray photon is firstly thought to follow the Poissonian distribution so that $\sigma^2 = N$, where N is the average number of the produced EHPs. However, it has been found that the variance of the number of EHPs is actually smaller than the value calculated from the Poissonian distribution. This implies that the ionisation events are not completely independent. Fano [12] introduced Fano factor, f_F, to characterise the variance of the number of EHPs produced by ionisation of gas, which is expressed as

$$\sigma^2 = f_F N. \quad (2\text{-}10)$$

This indicates that the ionisation process lies between two extreme cases which are ionisation events are completely independent ($f_F = 1$) and all ionisation events completely convert photon energy to EHPs ($f_F = 0$).

Due to the fluctuation of number of EHPs created during the ionisation event, there is a theoretical limit on the lowest possible energy resolution called Fano-limited resolution, E_f. The energy peak is assumed to have a Gaussian shape since the number of EHPs is a large number. Then the Fano-limited resolution in term of energy can be expressed as

$$FWHM_f = 2.35\varepsilon\sqrt{f_F N} = 2.35\sqrt{f_F E\varepsilon}, \qquad (2\text{-}11)$$

where ε is the average energy required to create an EHP and E is the energy of the incident X-ray.

2.4.6 APD X-ray detector

In a spectroscopy system, apart from the Fano noise, the electronic noise (e.g. from diode's leakage current, capacitance and preamplifier) also contributes to the spread of energy peak. Therefore the total energy resolution of a spectrometer in *FWHM* is usually expressed as

$$(FWHM_{total})^2 = (FWHM_f)^2 + (FWHM_{EN})^2, \qquad (2\text{-}12)$$

where $FWHM_{EN}$ accounts for the electronic noise.

Using an APD as the X-ray detector will improve the signal to noise ratio and hence energy resolution due to the avalanche gain mechanism. However the avalanche gain fluctuation, characterised by excess noise factor, can degrade the energy resolution. Work in [10, 13, 14] have shown that for an APD X-ray detector the excess noise is added to the Fano-limited energy resolution giving the total intrinsic energy resolution as

$$(FWHM_{total})^2 = (2.35)^2 \times (f_F + F - 1)E\varepsilon + (FWHM_{EN})^2. \qquad (2\text{-}13)$$

However, this equation doesn't show that the electronic noise will be reduced by the avalanche gain which is the main advantage of APDs used as X-ray detectors. In order to understand the effect of avalanche gain fluctuation on the detector's intrinsic energy resolution and electronic noise, following derivation is carried out.

Since the energy resolution is related to the fluctuation of number of collected electrons, the total number of electrons needs to be considered. If the number of primary photo-generated electrons is N_0, number of electronic noise charge is N_{EN} and mean avalanche gain is $\bar{M}$, the number of total collected electron is

$$N_{total} = N_0 \cdot \bar{M} + N_{EN}. \qquad (2\text{-}14)$$

Assuming N_{EN} is independent with avalanche gain, according to error propagation rules, the variance of N_{total} can be expressed as

$$\sigma_{total}{}^2 = \bar{M}^2 \cdot \sigma_{N_0}{}^2 + N_0{}^2 \cdot \sigma_{\bar{M}}{}^2 + \sigma_{EN}{}^2, \quad (2\text{-}15)$$

where $\sigma_{N_0}{}^2, \sigma_{\bar{M}}{}^2$ and $\sigma_{EN}{}^2$ are the variance of N_0, $\bar{M}$ and N_{EN} respectively.

Again, according to the propagation rules, when $\bar{M} = \frac{1}{N_0}\sum_0^{N_0} M_k$,

$$\sigma_{\bar{M}}{}^2 = (1/N_0)\sigma_M{}^2. \quad (2\text{-}16)$$

By substituting equation (2-16) into equation (2-15), we get

$$\sigma_{total}{}^2 = \bar{M}^2 \cdot \sigma_{N_0}{}^2 + N_0 \cdot \sigma_M{}^2 + \sigma_{EN}{}^2. \quad (2\text{-}17)$$

Since the calibration of pulse height distribution into energy requires the multiplied signal peak to be scaled by $\bar{M}$, the final variance is

$$\sigma'_{total}{}^2 = \frac{\sigma_{total}{}^2}{\bar{M}^2} = \sigma_{N_0}{}^2 + \frac{N_0}{\bar{M}^2} \cdot \sigma_M{}^2 + \frac{1}{\bar{M}^2} \cdot \sigma_{EN}{}^2. \quad (2\text{-}18)$$

From equation (2-10) and (2-4), we have $\sigma_{N_0}{}^2 = N_0 f_F$ and $\sigma_M{}^2 = (F-1)\bar{M}^2$. By substituting these two equations into equation (2-18), we have

$$\sigma'_{total}{}^2 = N_0 f_F + N_0(F-1) + \frac{1}{\bar{M}^2} \cdot \sigma_{EN}{}^2. \quad (2\text{-}19)$$

Knowing $FWHM = 2.35\sigma\varepsilon$, the total energy resolution is

$$(FWHM_{total})^2 = (2.35)^2 \times (f_F + F - 1)E\varepsilon + \frac{1}{\bar{M}^2}(FWHM_{EN})^2. \quad (2\text{-}20)$$

It can be seen from equation (2-20) that avalanche gain could improve the energy resolution of a spectroscopy system which is limited by electronics noise.

2.5 References

[1] G. E. Stillman and C. M. Wolfe, "*Avalanche photodiodes," Semiconductors and Semimetals, Academic Press,* vol. 12, pp. 291-293, 1977.

[2] R. J. McIntyre, "Multiplication noise in uniform avalanche diodes," *Electron Devices, IEEE Transactions on,* vol. ED-13, pp. 164-168, 1966.

[3] S. Cova, M. Ghioni, A. Lacaita, C. Samori, and F. Zappa, "Avalanche photodiodes and quenching circuits for single-photon detection," *Applied Optics,* vol. 35, pp. 1956-1976, 1996.

[4] S. J. Dimler, J. S. Ng, R. C. Tozer, G. J. Rees, and J. P. R. David, "Capacitive Quenching Measurement Circuit for Geiger-Mode Avalanche Photodiodes," *Selected Topics in Quantum Electronics, IEEE Journal of,* vol. 13, pp. 919-925, 2007.

[5] R. H. Haitz, "Mechanisms Contributing to the Noise Pulse Rate of Avalanche Diodes," *Journal of Applied Physics,* vol. 36, pp. 3123-3131, 1965.

[6] S. M. Sze and K. K. Ng, "*Physics of semiconductor devices*," 3rd ed., John Wiley and Sons Inc., 2007.

[7] J. P. Donnelly, E. K. Duerr, K. A. McIntosh, E. A. Dauler, D. C. Oakley, S. H. Groves*, et al.*, "Design Considerations for 1.06-µm InGaAsP-InP Geiger-Mode Avalanche Photodiodes," *Quantum Electronics, IEEE Journal of,* vol. 42, pp. 797-809, 2006.

[8] C. H. Tan, J. S. Ng, G. J. Rees, and J. P. R. David, "Statistics of Avalanche Current Buildup Time in Single-Photon Avalanche Diodes," *Selected Topics in Quantum Electronics, IEEE Journal of,* vol. 13, pp. 906-910, 2007.

[9] S. Ahmed, "*Physics and Engineering of Radiation Detection*," 1st ed., Academic Press Inc., 2007.

[10] G. Knoll, "*Radiation Detection and Measurement*," 3rd ed., Wiley, 2000.

[11] J. H. Hubbell and S. M. Seltzer. Tables of X-Ray Mass Attenuation Coefficients and Mass Energy-Absorption Coefficients (version 1.4) [Online]. Available: http://www.nist.gov/pml/data/xraycoef/

[12] U. Fano, "Ionization Yield of Radiations. II. The Fluctuations of the Number of Ions," *Physical Review,* vol. 72, pp. 26-29, 1947.

[13] M. Moszyński, M. Szawlowski, M. Kapusta, and M. Balcerzyk, "Large area avalanche photodiodes in scintillation and X-rays detection," *Nuclear Instruments and Methods in Physics Research Section A: Accelerators, Spectrometers, Detectors and Associated Equipment,* vol. 485, pp. 504-521, 2002.

[14] C. H. Tan, R. B. Gomes, J. P. R. David, A. M. Barnett, D. J. Bassford, J. E. Lees*, et al.*, "Avalanche Gain and Energy Resolution of Semiconductor X-ray Detectors," *Electron Devices, IEEE Transactions on,* vol. 58, pp. 1696-1701, 2011.

3 Experimental methods

This chapter will firstly describe several common measurements used to characterise the basic performances of APDs including current-voltage (I-V) measurement, capacitance-voltage (C-V) measurement and photomultiplication measurement. Then the experiment setups and theory for single photon counting and X-ray spectroscopy will be presented.

3.1 I-V measurement

I-V measurement is the basic characterisation to assess the performances of the photodiode. I-V measurement were carried out using a Keithley 236 source–measurement unit (SMU) or an Agilent B1505A power device analyser. During dark current measurements, the device under test (DUT) was placed in dark environment to minimise photocurrent.

The forward current equation of a p-i-n diode is [1]

$$I_F = I_s \exp\left[\frac{q(V_t - R_s I_F)}{nk_b T} - 1\right], \quad (3\text{-}1)$$

where I_s is the saturation current, V_t is the total voltage drop across the diode, n is the ideality factor and k_b is the Boltzmann's constant. Series resistance R_s is taken into account since the potential drop across contact resistance between deposited metal contact and semiconductor becomes significant at high forward current. The experimental I–V data can be fitted using the forward current equation to deduce values of R and n. Ideality factor n has a value between 1 and 2 depending on whether diffusion or generation-recombination current are more dominant.

For the mesa diodes studied in this thesis, the dark current measured could be due to current flowing through detector's bulk region or edge surface. The bulk dark current consists of the diffusion (I_{diff}), generation recombination ($I_{g\text{-}r}$) and band-to-band tunnelling (I_{tunn}) components. Surface dark current can be caused by surface states formed on the sidewall of etched mesa due to the abrupt termination of the semiconductor material. The bulk- and surface-related dark current should scale with diode area and

perimeter respectively. Hence the origin of dark current can be determined by normalising the dark current to diode area and perimeter.

For SPADs, bulk dark current is the main source of the *DCR*. The surface dark current, in contrast, is not believed to contribute to *DCR*, because the surface carriers will not experience such a high electric field and generate avalanche pulses. From the reverse bias I-V characteristic, important information, such as breakdown voltage and punch-through voltage (V_p), can be obtained.

For X-ray APDs, dark current contributes to the system noise, which reduces the signal to noise ratio and results in poor energy resolution. So the dark current of the diode needs to be kept low, for instance, InAs diode need to be cooled down to 77 K to reduce the high dark current at room temperature. Dark current has another effect on the detector in the spectroscopy measurement. Reverse bias to the detector is always applied with a large value resistor in series in order to prevent charge signal discharging through it. When the dark current is very high, the voltage drop across the biasing resistor might be so large as to prevent further increase in the actual reverse bias applied to the diode.

3.2 C-V measurement

C-V measurements were made using Agilent/HP 4275A Multi- Frequency LCR Meter with AC test signal of 60 mV rms and frequency of 1 MHz. C-V results were mainly used to estimate the depletion width (W_d), doping profile and built-in potential (V_{bi}).

Using a one sided abrupt junction model, the depletion width W_d is given as

$$W_d = \sqrt{\frac{2\varepsilon_s}{qN_0}\left(V_{bi} + V_R - \frac{2k_bT}{q}\right)}, \qquad (3\text{-}2)$$

where ε_s is the permittivity of the semiconductor, N_0 is the doping concentration of the depletion region and V_R is the reverse bias voltage. $2k_bT/q$ is used to correct the effect of majority carrier diffusion at the edge of the depletion region. The capacitance of the junction with area of A and depletion width W_d is

$$C = \frac{\varepsilon A}{W_d}. \tag{3-3}$$

By substituting equation (3-2) into equation (3-3), we get

$$\frac{1}{C^2} = \frac{2}{q\varepsilon N_0 A^2}\left(V_{bi} + V - \frac{2k_b T}{q}\right). \tag{3-4}$$

The built-in potential can be calculated by firstly plotting the $1/C^2$ against bias voltage V in straight line. Then the intercept of the x-axis and $1/C^2$ gives the value of $V_{bi} - \frac{2k_b T}{q}$.

The expression of doping profile at different depletion width is given as below by rearranging equation (3-4),

$$N_0(W_d) = \frac{2}{q\varepsilon A^2}\frac{dV}{d\left(\frac{1}{C^2}\right)}. \tag{3-5}$$

Furthermore, the electric field profile can be estimated by solving Poisson's equation

$$\frac{dE}{dx} = \frac{qN_0}{\varepsilon_s}, \tag{3-6}$$

where E is the electric field in the region and x is the depletion width of the region. With this equation, the depletion width of the diode at a voltage (V_t) can be calculated by equating the area under the electric field to V_t. Then the capacitance of the diode can be obtained using equation (3-3). The calculated capacitance is then fitted to the experimental results by adjusting the doping density in each layer in the diode and intrinsic region thickness. When the diode capacitance is small (i.e. less than 1 pF), parasitic capacitance can add significant error. So it is necessary to perform an open circuit zero to remove the parasitic capacitance. In addition, wet etching might reduce the actual size of the diode through isotropic etching, affecting the measured capacitance. Hence capacitance data of diodes with different sizes must be measured and compared to ensure accurate interpretation of the data.

3.3 Photomultiplication measurement

The multiplication characteristic of the APD used in this work was obtained by using photomultiplication measurement. This is calculated with the equation

$$M(V) = \frac{I_{ph}(V)}{I_{pr}(V)}, \tag{3-7}$$

where I_{ph} is the measured photocurrent and I_{pr} is the unmultiplied primary current.

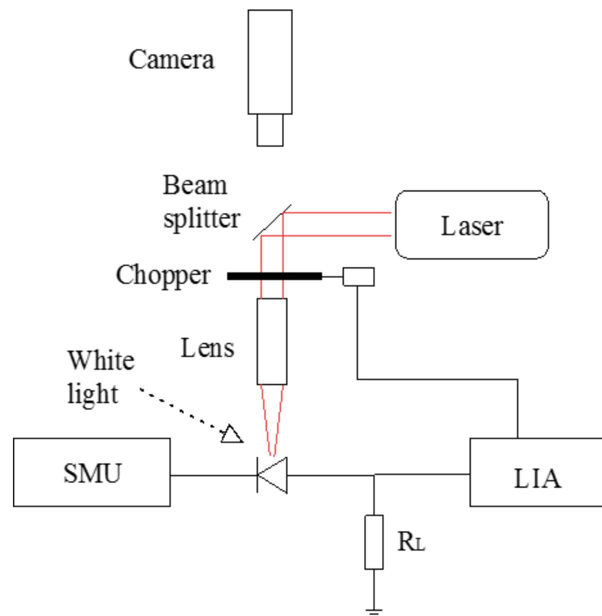

Figure 3-1 Schematic diagram of the setup used to measure photomultiplication. SMU: Keithley 236 source measurement unit. LIA: Stanford Research 830 Lock-in amplifier.

I_{ph} was measured using the setup shown in Figure 3-1. Laser beam was focused on the optical window of the diode using a microscope lens. The laser spot was confined within the top mesa to ensure pure carrier injection. An optical chopper was used to modulate the laser at frequency of 180 Hz. The reverse biased APD illuminated by the modulated laser generated an AC current signal which was then sensed by measuring the voltage drop across the load resistor with the lock-in amplifier. The frequency of the optical chopper was fed to the LIA as reference frequency. LIA can only measure signal at reference frequency and reject noise at other frequencies. Therefore, for APDs with high dark current, photomultiplication measurement using LIA is preferred.

I_{ph} increases with bias voltage due to two possible reasons: increased multiplication gain and higher collection efficiency due to increased depletion region. The latter will

increase the I_{pr} and can be approximated by a linear function $I_{pr} = aV + b$. This equation can be used to fit the dependence of I_{pr} with V at small bias voltage and extrapolate the value of I_{pr} at different bias voltages. The gain curve can then be obtained from above. InAs APDs used in this work (chapter 6) have long carrier diffusion length and hence there was negligible increase of I_{pr} with V. For these APDs, I_{pr} was assumed to be constant with V.

3.4 Single photon counting

3.4.1 Experimental setup

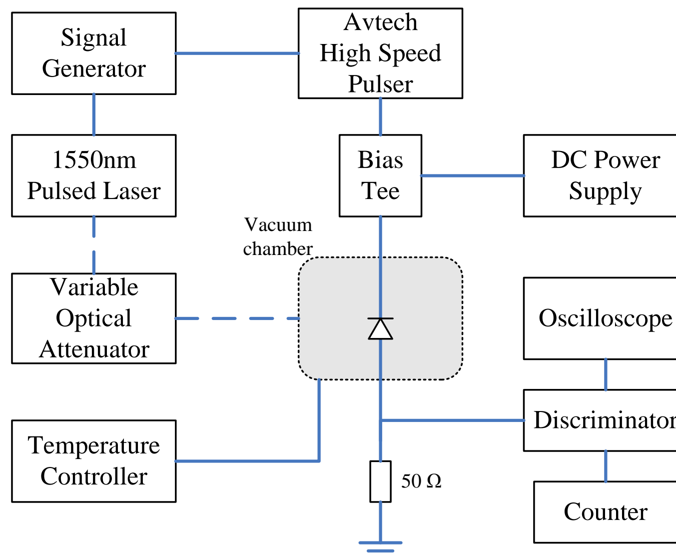

Figure 3-2 Experimental setup for dark counts and photon counts measurements with gated quenching. Solid lines and dashed lines represent electrical and optical connections, respectively.

Due to the need of temperature stabilisation and low temperature characterisation, a cryogenic probe station (Janis ST-500) was used to cool the SPAD to desired temperatures. The cryostat was cooled by continuous flowing liquid nitrogen from a pressurised liquid nitrogen dewar. Before cooling down, the sample chamber was evacuated by a turbo pumping station (Pfeiffer High Cube 80) to ~ 2×10^{-5} mBar (pressure near the chamber is < 1×10^{-3} mBar) to avoid any subsequent moisture condensation. A temperature controller was used to control the heater underneath the sample stage and stabilise the temperature. The optical window was covered by multi-layer black aluminium foil to block the ambient light.

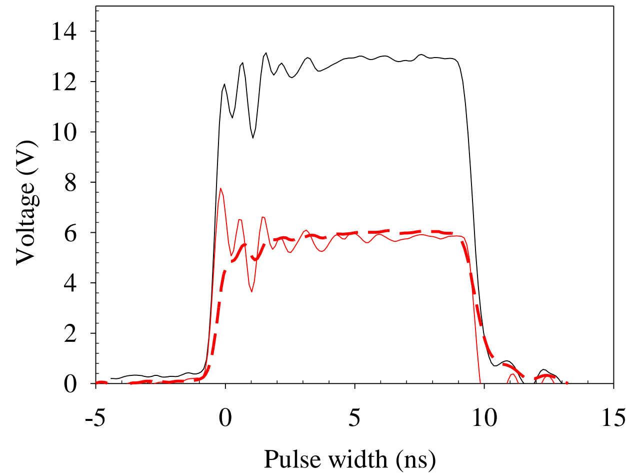

Figure 3-3 AC pulses with 10 ns pulse width from the Avtech pulser. Pulses obtained using internal amplitude adjustment are shown in solid line, and the pulse generated using external attenuator is shown in dash line.

The setup used is shown schematically in Figure 3-2 and the SPAD was placed inside the Janis probe station. In order to pulse-bias the SPAD above the breakdown voltage, a commercial bias tee (Picosecond Pulse Labs, 5530B) was used to superimpose AC voltage (V_{AC}) pulses on a DC bias (V_{DC}), which was set below the breakdown voltage. The DC bias was provided by a Keithley 2400 or an Agilent B2901A SMU. The AC voltage pulses was provided by an Avtech AVI-V-2L pulser which was triggered by an Agilent 81101A pulse generator. The Avtech pulser can provide AC pulses with amplitude up to 40 V and frequency up to 100 kHz. The pulse amplitude is adjustable, however, the pulse shape is poorer (i.e. ringing at rising edge) at lower voltage amplitude as shown in Figure 3-3. Hence a variable electrical attenuator was used to generate better low-amplitude pulses. The pulse width is variable from 1 to 10 ns (*FWHM*) and the rise and fall time is less than 500 ps. The SPAD was reverse biased by a positive superimposed voltage connected to the cathode of the SPAD, and then the anode was connected to the ground through a 50 Ω resistor. 50 Ω resistor was used to achieve impedance matching with the coaxial cable and input impedance of the following circuit. Avalanche signals from the SPAD (due to dark or photon-generated carriers) were detected by an edge-triggered discriminator (designed and made by Simon Dimler), which then generated nuclear instrument module (NIM) signals. The threshold voltage of the discriminator was adjusted to be higher than the transient pulses but lower than the avalanche pulses. The applied threshold voltage was monitored by a Keithley 2700 Digital Multimeter (DMM). The NIM signals from the discriminator were supplied to a

Canberra 512 counter to yield count rate. The avalanche signals were also monitored using a Lecroy Waverunner 204Xl oscilloscope (10GS/s) during measurements.

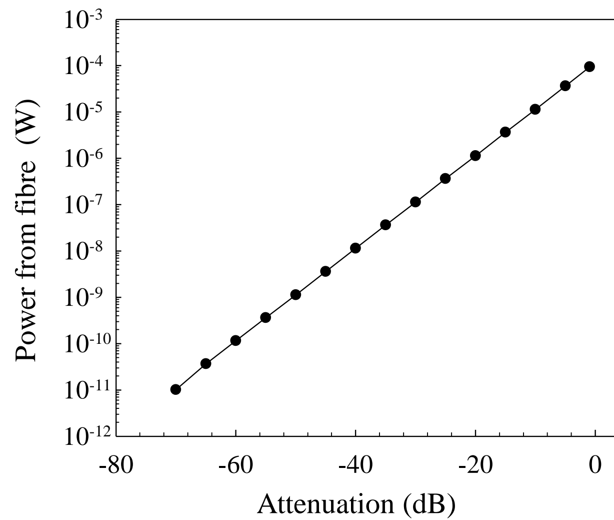

Figure 3-4 Output power from the fibre when 1 mW input continuous wave (CW) laser is attenuated from 0 to 70 dB.

Photon source for the photon counts measurements was a fibre-coupled pulsed laser from Picosecond Laser Diode Systems (PiL155), which emits 1550 nm wavelength light pulses with 20 ps pulse width (*FWHM*) at a frequency from 1 Hz to 1 MHz. The light pulses were synchronised with the AC voltage pulse by adjusting the delay time between them using the Agilent pulse generator. This was done as follow:

- Firstly reverse bias the SPAD at a voltage higher than punch-through voltage and lower than breakdown voltage.
- Then shine the SPAD with un-attenuated pulsed light and check the positions of the photocurrent peak and AC pulse using the oscilloscope.
- At last, adjust the delay time between the photocurrent peak and AC pulse until they are the well synchronised.

The light was attenuated to a desired level by an Exfo FVA-3100 variable optical attenuator (VOA). The attenuation of the VOA along with the fibres connected to the input and output of the VOA was calibrated through optical power measurement using an InGaAs photodiode with known responsivity. The laser power from the fibre was determined by measuring the photocurrent of the InGaAs photodiode generated by shining 1550 nm CW laser on it. Figure 3-4 shows the measured laser power from the

fibre at attenuation level from 0 to 70 dB. With this figure the laser power output from the fibre can be determined if the input laser power and attenuation are known.

3.4.2 Dark count probability and DCR

In gated mode, dark count probability of the SPAD, P_d, is defined as the probability that a dark count is triggered by at least one dark carrier within the AC pulse duration. Since the number of dark carriers per time duration is random, so its distribution needs to be considered.

Assuming the dark carriers follows Poisson distribution [2], if the average number of carriers in a pulse is n_d, the probability that there are k carriers in a pulse will be

$$P(n_d, k) = \frac{{n_d}^k \times e^{-n_d}}{k!}. \tag{3-8}$$

For each k value, the probability of detecting a dark count is $1\text{-}(1\text{-}P_b)^k$. Integrating $P(n_d, k)$ weighted by $[1\text{-}(1\text{-}P_b)^k]$ over k from 0 to $+\infty$, we get

$$P_d = \sum_{k=0}^{\infty}[1-(1-P_b)^k] \times \frac{{n_d}^k \times e^{-n_d}}{k!}. \tag{3-9}$$

Simplifying this equation as follow

$$P_d = \sum_{k=0}^{\infty}\{[1-(1-P_b)^k] \times \frac{{n_d}^k \times e^{-n_d}}{k!}\}$$

$$= \sum_{k=0}^{\infty}\frac{{n_d}^k \times e^{-n_d}}{k!} - \sum_{k=0}^{\infty}[\frac{{n_d}^k \times e^{-n_d}}{k!} \times (1-P_b)^k]$$

$$= 1 - e^{-n_d \times P_b}\sum_{k=0}^{\infty}[\frac{[n_d(1-P_b)]^k \times e^{-n_d(1-P_b)}}{k!}]$$

$$= 1 - e^{-n_d \times P_b}$$

we get the expression of P_d

$$P_d = 1 - e^{-n_d \times P_b} . \quad (3\text{-}10)$$

In the gated mode measurement, P_d can be obtained experimentally through

$$P_d = \frac{N_d}{f}, \quad (3\text{-}11)$$

where N_d is the number of measured dark counts per second and f is the repetition frequency of the AC pulses.

DCR is the number of dark counts per second when the SPAD is operated in free running mode with fast quenching and recharging. So for SPADs operated in gated mode, *DCR* is related with P_d with equation

$$P_d = 1 - e^{-DCR \times t_{on}} , \quad (3\text{-}12)$$

where t_{on} is the pulse width of the gate (i.e. on-time). When $DCR \times t_{on}$ is << 1, equation (3-12) can be rewritten as

$$DCR = \frac{P_d}{t_{on}}. \quad (3\text{-}13)$$

3.4.3 Single Photon Detection Efficiency

SPDE is used to characterise the ability of the SPAD to detect a single photon. However, the number of photons per light pulse follows a distribution which also needs to be taken into account. Assuming Poissonian statistics for the arriving photons, the probability of a light pulse triggering an avalanche is

$$P_{ph} = \sum_{k=0}^{\infty} [1 - (1 - SPDE)^k] \times \frac{n^k \times e^{-\bar{n}}}{k!} , \quad (3\text{-}14)$$

where $\bar{n}$ is the average number of photon per light pulse and k is the number of arrived photon. Using the same simplification used in section 3.4.2 for P_d, P_{ph} can be given as

$$P_{ph} = 1 - e^{-\bar{n} \times SPDE} . \quad (3\text{-}15)$$

Since we know that the total count probability (i.e. probability to detect a count triggered by either a dark carrier or a photo-generated carrier), P_t, can be expressed as

$$1 - P_t = \left(1 - P_{ph}\right) \times (1 - P_d). \tag{3-16}$$

Substituting equation (3-15) into the equation (3-16) and re-arranging the equation, we get

$$SPDE = \frac{1}{\bar{n}} \times ln\left(\frac{1 - P_d}{1 - P_t}\right). \tag{3-17}$$

P_t was obtained experimentally from equation $P_t = \frac{N_t}{f}$, where N_t is the total counts measured per second when the SPAD is illuminated with light.

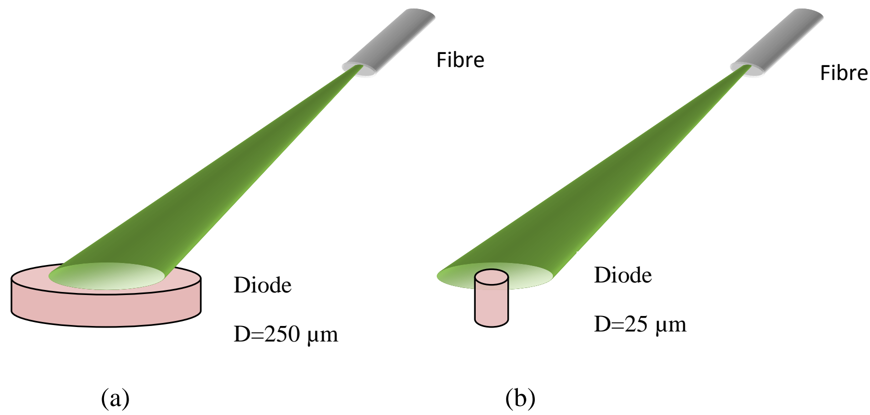

Figure 3-5 Illustration of coupling efficiency measurement. Diodes with diameter 250 µm (a) and 25 µm (b) are shown.

In order to deduce the *SPDE*, the average number of photon arriving at the diode ($\bar{n}$) must be determined accurately. Since the average power of the laser coming out from the fibre tip (P_{ave}) can be calculated using the relationship shown in Figure 3-4, $\bar{n}$ can be expressed as

$$\bar{n} = \eta_{cp} \times \frac{P_{ave}}{f \times hv}, \tag{3-18}$$

where η_{cp} is the optical coupling efficiency from the fibre to the diode. This is due to the fact that the diameter of the SPAD device used in this work was 25 µm which is smaller than the diameter of the fibre core (65 µm). Moreover, the divergence of the light beam at the end of the fibre will further increase the spot size, as shown in Figure 3-5. Thus

photocurrent measurements using 25 and 250 μm diameter InAs photodiodes were taken. During the measurement for 250 μm diameter diode, it was found that there was range within which the photocurrent is independent with the fibre position indicating the light spot was smaller than the optical window. Therefore the coupling efficiency was calculated by taking the ratio of photocurrent using 25 and 250 μm diameter diodes. The photocurrent results from both diode sizes are summarised in Table 3-1. The coupling efficiency was calculated to be 5% at reverse bias of 0.2 V.

Table 3-1 Photocurrent (μA) measured from two different size diodes at different bias voltages using CW laser at 1550 nm. The result from D4 with 25 diameter at 0.5 V reverse bias was probably affected by degradation of the diode and hence was excluded.

Diode diameter	Diode	Photocurrent (μA)		
		0V	-0.2 V	-0.5 V
ø = 250 μm	D1	0.59	11.38	12.36
	D2	0.62	11.51	11.77
ø = 25 μm	D1	0.21	0.57	0.67
	D2	0.25	0.50	0.55
	D3	0.22	0.63	0.65
	D4	0.24	0.60	9.3

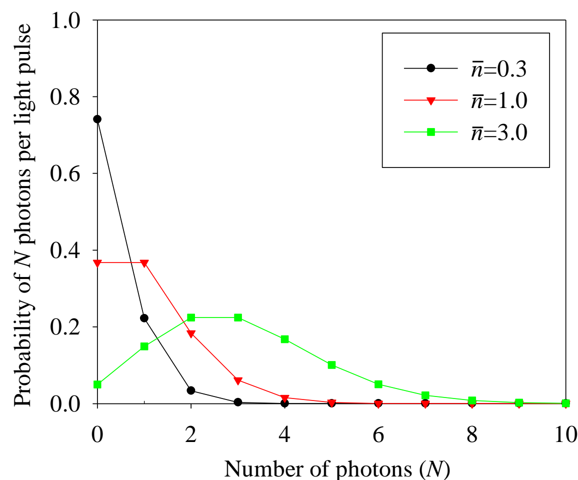

Figure 3-6 Probability distribution of photon number per light pulse at different average photon number.

For the measurement in chapter 4 and 5, $P_{average}$ was measured to be 77 fW, so using equation (3-15) with $\eta_{cp} = 0.05$, photon energy = 0.8 eV, and $f = 100$ kHz, n was estimated to be 0.3. Since the number of photon per pulse follows Poisson distribution it is

important to keep the average photon number low to avoid the case that multiple photons present in one light pulse, which will increase the P_{ph} overestimating the *SPDE*. Figure 3-6 shows the probability distribution of photon number per light pulse at different average photon number. The probability of multiple photon per light pulse are calculated to be 0.75, 0.26 and 0.037 for n is 3, 1 and 0.3 respectively.

3.4.4 Modified CQC for measurements at cryogenic temperature

CQC can provide well defined over-bias voltage and effective avalanche quenching, which are important in the characterisation and analysis of SPAD. But in measurements at cryogenic temperature, cables or wires connecting device and CQC, which are mounted inside and outside the cryostat respectively, introduce parasitic capacitance across the device resulting in large transient pulses and complicating the counting of the avalanche pulses.

Hence I modified the existing CQC to make it capable of measurements at cryogenic temperature. The core parts of the CQC circuit (DUT, dummy capacitor, biasing capacitor and Schottky Diode) were moved into a Judson metal dewar along the DUT and other parts are mounted outside the cryostat to minimise the capacitance across the device and reduce the transient pulses.

The modified CQC circuit was tested by measuring *DCR* of a Si SPAD (supplied by University College Cork) at 77 K. The transient pulses after cancellation were lower than avalanche pulses. A *DCR* of 12 Hz was obtained with over bias of 4.5 V and pulse width of 200 ns at 77 K. This was more than 4 orders of magnitude lower than the *DCR* of 270 kHz at room temperature.

3.5 X-ray spectroscopy

The X-ray spectroscopy measurement was carried out using the set up shown in Figure 3-7. The packaged diode was placed in a shielded chamber approximately 5 mm from a 185 MBq ^{55}Fe radioisotope source. A Keithley 2400 SMU was used to reverse bias the device. The resultant signal from the diode under test was integrated and amplified using an Amptek A250CF charge-sensitive preamplifier, before being further amplified and shaped into semi-Gaussian pulses by an Ortec 570 shaping amplifier. The output from the shaping amplifier was fed to an Ortec multi-channel analyser (MCA)

controlled by a PC. A MCA emulator software (Ortec Maestro-32) was used to generate pulse height distributions which can then be converted into energy spectra.

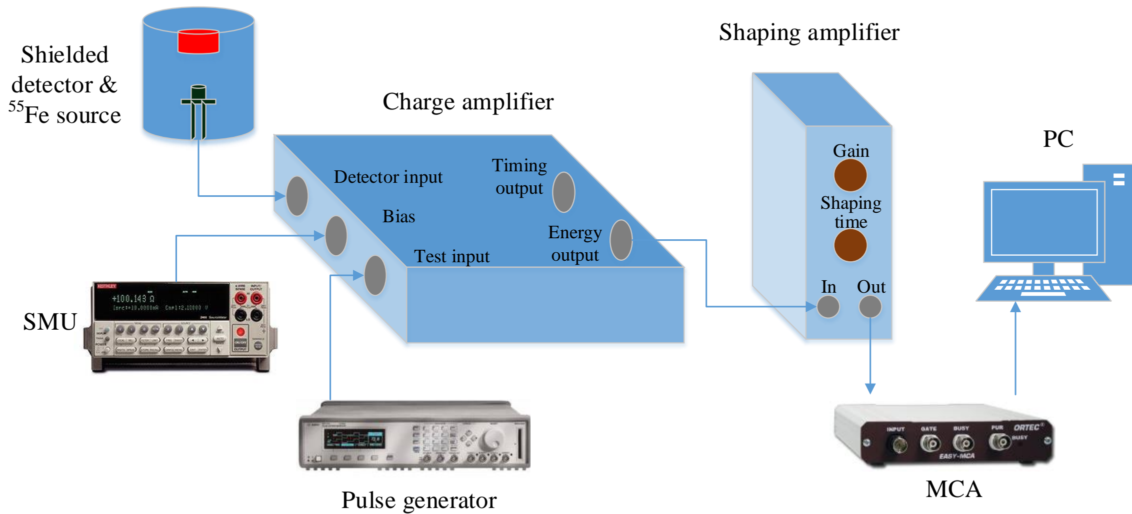

Figure 3-7 Schematic diagram of a X-ray spectroscopy system. MCA: Multi-channel analyser.

3.5.1 Radioactive source

A ^{55}Fe radioactive X-ray source from HTSL [3] was used for X-ray characterisations in this work. The ^{55}Fe was sealed in a welded Monel capsule with a brazed beryllium window. The source was covered in an additional cylindrical Perspex sleeve for handling purposes. The diameter of the active aperture was 10 mm. ^{55}Fe decays via electron capture to ^{55}Mn with a half-life of 2.7 years. The emissions of the source included K_α X-ray at 5.9 keV (24.5% probability), and K_β X-ray at 6.49 keV (3.29 % probability) [4].

3.5.2 Preamplifier

Electric signals generated in the semiconductor materials due to absorption of soft X-ray photons usually have very narrow width and small amplitude. Therefore it is necessary to get the signal amplified by a pre-amplifier before being fed to signal processing units. Charge-sensitive preamplifier is preferred since its output voltage is proportional to the total charge collected by the detector and independent on the input capacitance (combination of diode capacitance and parasitic capacitance) which could be changing with different operation conditions.

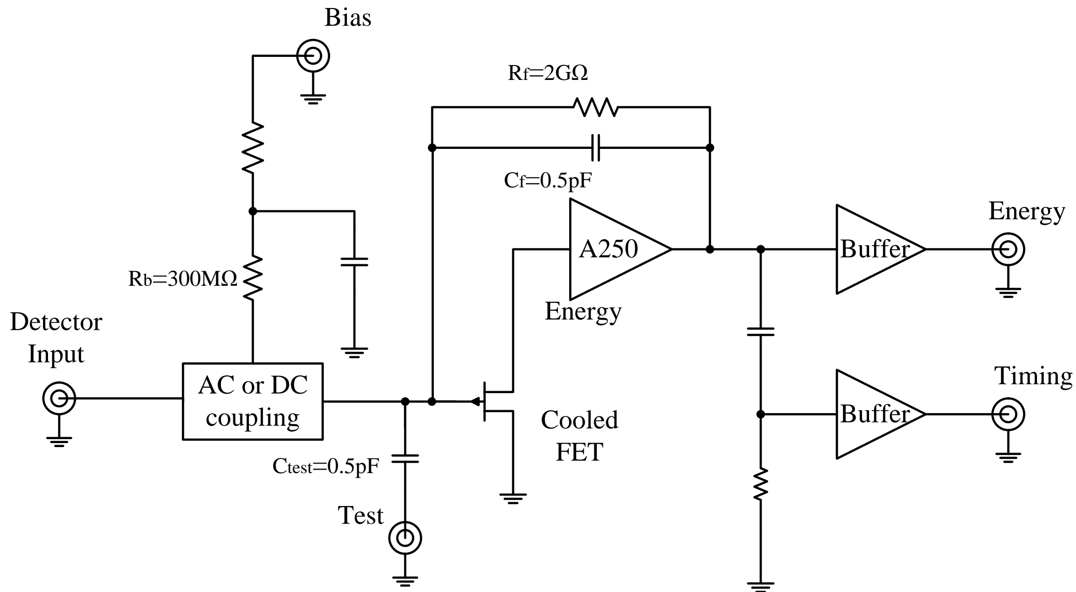

Figure 3-8 Block diagram of an Amptek A250 CF charge sensitive preamplifier [5].

For a charge-sensitive amplifier with a FET at the input, the capacitance of the FET needs to be matched with the detector capacitance to maximise the SNR. The reason is that transconductance is proportional to the capacitance of the FET. Transconductance of the FET needs to be kept high to reduce the noise of preamplifier, however, the capacitance will also be increased and in turn increase the electronic noise. The optimal point has been shown to be where the detector capacitance is equal to the FET capacitance [6]. As shown in Figure 3-8, Amptek A250 charge sensitive preamplifier has three FETs to allow matching to detectors with different capacitances. FET 1 and 2 have a low capacitance of 8 pF and FET 3 has a higher capacitance of 30 pF. Since the diodes used in this work are generally below than 10 pF, FET with 8 pF capacitance was used. In addition, all the three FETs are placed on top of a thermoelectric cooler and enclosed in a TO-8 package. Cooling the FET reduces its leakage current and increases the transconductance, both of which act to reduce the amplifier noise.

The detector was reverse biased through a biasing resistor (R_b = 300 MΩ). The value of R_b was large so that the photo-generated carriers will not discharge through R_b before being collected by the preamplifier. However, for detectors with high leakage current, the potential drop across R_b would reduce the actual voltage applied to the detector. In the worst case, e.g. the leakage current increases with reverse bias resulting in a potential drop larger than the increase in bias itself, limiting the maximum applied voltage. This can be solved by reduce the value of R_b (R_b consists of three 100 MΩ resistor in series)

by simply remove one or more resistor(s). For coupling configuration, DC coupling could offer lower noise than AC coupling, however, extreme caution is required since any accidental high DC voltage which could cause fatal damage the preamplifier. In this work the input of preamplifier was AC coupled to the detector.

The feedback resistor (R_f) with resistance of 2 GΩ was used to discharge the feedback capacitor (C_f = 0.5 pF). Hence the output voltage would decay back to baseline with a time constant of $R_f \times C_f$ = 1 ms. The feedback resistor contributes to the thermal noise, as shown in equation

$$i_n{}^2 = \frac{4kT}{R_f}, \tag{3-19}$$

where $i_n{}^2$ is the noise current spectral density of thermal noise. Increasing R_f thus diminishes $i_n{}^2$. However, large R_f might result in large decay time constant causing pulses pile-up at high count rate. Pile-up occurs when the time interval between two adjacent signal pulses is less than the decay time of the signal pulses, which results in false amplitudes. It is worth noting that each pulse is superimposed on the residual tail of the previous pulse whose amplitude depends on the random rate of incoming X-ray photons. So at high count rate, pile-up of pulses shown in Figure 3-9 might significantly degrade the energy resolution if inappropriate decay time is used. Additionally, gate leakage current of the FET flowing through R_f will make the output terminal operate at a negative DC level. The DC level should not exceed the clipping level, so R_f needs to be lower than a value determined by the ratio of clipping voltage over FET leakage current.

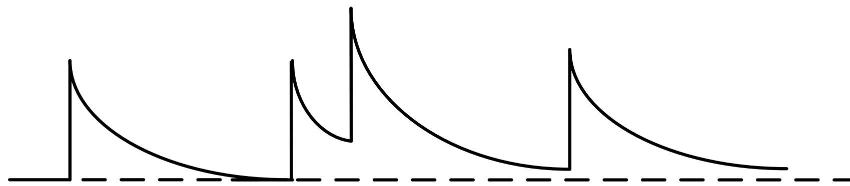

Figure 3-9 Pile-up of pulses with exponential tail from the preamplifier.

Noise measurement can be performed by connecting a pulse generator (Agilent 81101-a) to the test input of the preamplifier. Square waves with a rise time of 5 ns and pulse width of 50 μs was applied to a 0.5 pF test capacitor (C_{test}) to simulate the charges induced by X-ray photons. Charges accumulated on the test capacitor (Q) can be express as $Q = C_{test}V$, where V is the amplitude of square pulses. Detector should be connected

to the input terminal to take the noise sources from detector (e.g. leakage current and capacitance) into account. Detector should never be connected to test input to avoid any large current pulse which causes damage to the FET. The output of preamplifier was connected to shaping amplifier with shaping time used in the actually measurement. Test pulses with different amplitudes will give peaks at different channel number at the spectrum obtained by the MCA. Then the channel number on the spectrum was converted to energy by performing procedures listed in Appendix A. After calibration of the spectrum, the noise value (*FWHM*) can be calculated by Gaussian fitting to the noise peak. Details of procedures of noise measurement are presented in Appendix B.

3.5.3 Post shaping amplifier

Shaping amplifier is used to improve the signal to noise ratio of the system while keeping the pulse height information of the signal. The shaping amplifier usually employs a CR-(RC)^n circuit (i.e. a high-pass filter/differentiator cascaded with a series of low-pass filters/integrators) to reduce the bandwidth of the signal. This is very helpful to reduce the white noise from amplifier which is independent with frequency and proportional with the bandwidth. In addition, the output signal from preamplifier generally has a long decay time (e.g. several hundred of μs) due to the large feedback resistance, which will limit the maximum count rate. This can be solved by the high-pass filter which cuts off the long decay tail by reducing its low frequency component. However, the pulse after high-pass filter has a sharp peak which is still not suitable for pulse height analysis because of the short peak duration. A stage of low-pass filter will increase the rise time of the signal pulse and results in a rounded peak which allows the MCA to get pulse high information more easily. Moreover, the low-pass filter can further reduce the amplifier noise. Figure 3-10 shows the schematic of the Ortec 570 shaping amplifier [7].

The time constant of the high-pass and low-pass filter are typically set the same, which is the so-called shaping time constant. For spectroscopy system with high electronic noise, choice of shaping time constant is vital to achieve high energy resolution since the electronic noise (i.e. series and parallel noise) is dependent on the shaping time. For instance, in Figure 3-11, shaping time constant of 1 and 2 μs give the best energy resolution of 1.95 keV.

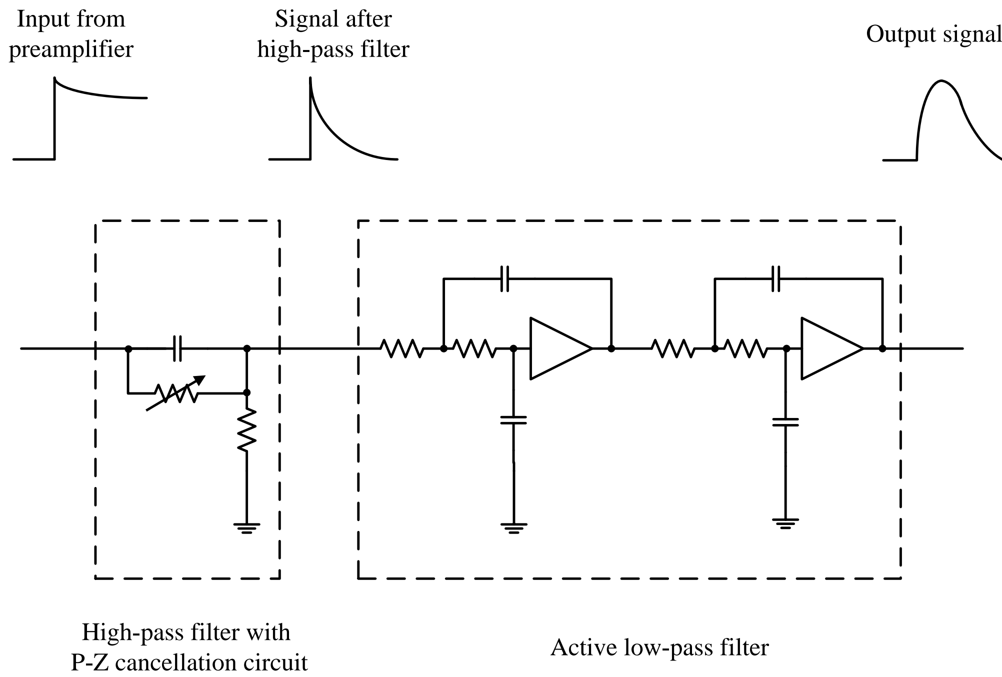

Figure 3-10 Block diagram of the Ortec 570 shaping amplifer. Typical pulse shapes at different nodes in the circuit are also shown.

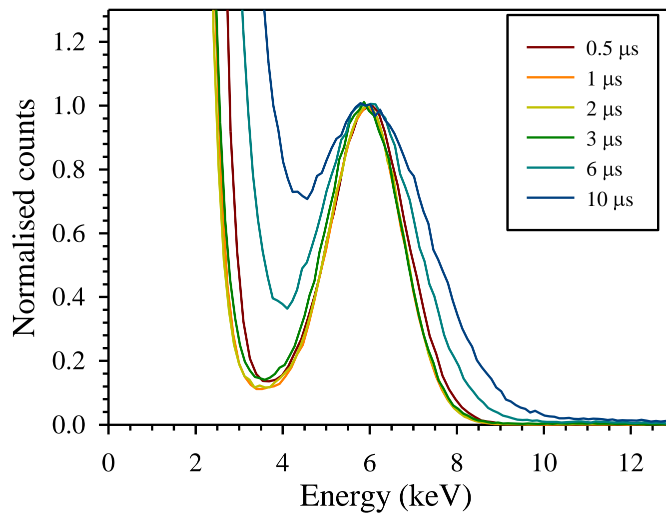

Figure 3-11 Energy spectra (^{55}Fe) from a GaAs p-i-n diode at room temperature using different shaping time constants.

Since the output of preamplifier is an exponentially decaying pulse, this will cause an undershoot on the signal (i.e. peak below the baseline) after going through the high-pass filter. At high count rate this will reduce the pulse height of the following pulse and degrade the energy resolution. The ratio of amplitude of the undershoot and the signal after the high-pass filter decreases with the decay time of the preamplifier output signal.

Therefore, increasing the decay time of preamplifier could suppress the undershoot, while at the price of low maximum count rate. In ORTEC 570, a pole-zero (P-Z) cancellation circuit, as shown in Figure 3-12, is used to eliminate undershoot. This P-Z cancellation circuit introduces a zero which has an adjustable value by changing the resistance of R_2. By equating RC to the time constant of the decay time of the preamplifier, this zero could cancel the pole caused by the preamplifier giving an exponential decay without undershoot. Before any high count rate measurement, the P-Z adjustment is essential to make sure the falling edge of the output signal from shaping amplifier returns to the baseline without any undershoot and overshoot. The output signal can be checked by being DC coupled to an oscilloscope. The P-Z cancellation circuit can be adjusted using the potentiometer on the front panel of the shaping amplifier. The minimum decay time that the P-Z cancellation circuit can cope with is 40 μs.

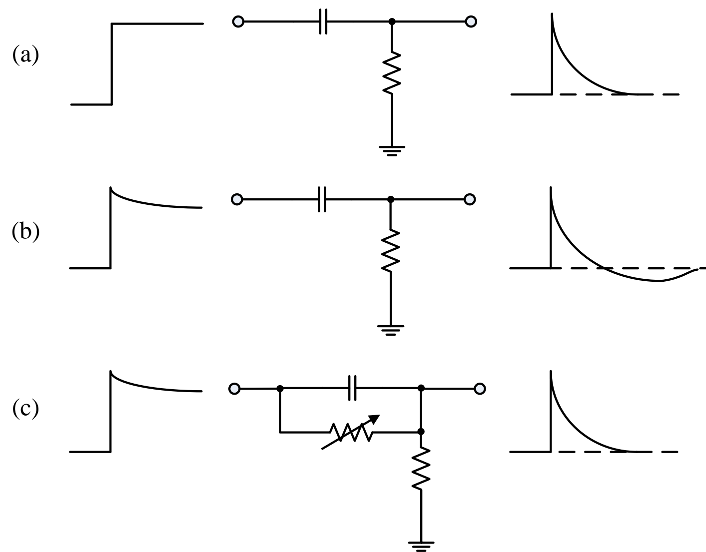

Figure 3-12 (a) Output signal from a high-pass filter when input signal is a step function. (b) Output signal from a high-pass filter when input signal is an exponential decay function. (c) Output signal from a high-pass filter with P-Z cancellation circuit when input signal is an exponential decay function.

In terms of the shape of the pulse being sent to the MCA, Gaussian function is an ideal choice because it has reasonably high SNR and needs short time to return back to baseline. But Gaussian shape requires the number of low-pass filter to be infinite, i.e. $n = \infty$ in a CR-(RC)^n circuit. The less n is, the less symmetrical the signal is and the smaller the SNR is. ORTEC 570 Spectroscopy Amplifier uses an active filter network which includes a high-pass filter and two second-order active low pass filters. Compared with

Gaussian shape, this active filter network gives a semi-Gaussian shape which has similar SNR and needs only a practical amount of electric circuitry.

3.6 References

[1] S. M. Sze and K. K. Ng, "*Physics of semiconductor devices*," 3rd ed., John Wiley and Sons Inc., 2007.

[2] S. Cova, M. Ghioni, A. Lacaita, C. Samori, and F. Zappa, "Avalanche photodiodes and quenching circuits for single-photon detection," *Applied Optics,* vol. 35, pp. 1956-1976, 1996.

[3] High Technology Source Ltd., *Iron-55 X-ray source*. Available: http://www.hightechsource.co.uk/Legacy/Resources/Iron-55.pdf

[4] D. C. Kocher, "Radioactive decay data tables," DOE/TIC-11026, Technical Information Center / U.S. Dept. of Energy, 1981.

[5] Amptek, "A250CF CoolFET® Charge Sensitive Preamplifier," Available: http://www.amptek.com/products/a250cf-coolfet-charge-sensitive-preamplifier/

[6] H. Spieler,. "*Radiation Detectors and Signal Processing*," Available: http://www-physics.lbl.gov/~spieler/Heidelberg_Notes/

[7] Ortec, *Model 570 Spectroscopy Amplifier Operating and Service Manual*. Available: www.ortec-online.com/download/570-MNL.pdf

4 InGaAs/InAlAs single photon avalanche diodes

Advantages of SPAD using InAlAs as the multiplication layer were discussed in chapter 1. In this chapter, the investigation on 1550 nm single photon detection using an InGaAs/InAlAs SPAD will be presented. Firstly, the wafer structure and fabrication details will be described. Then results from DC characterisations (i.e. I-V and C-V) and photon counting measurements (on *DCR*, *SPDE* and afterpulsing) will be shown and discussed.

4.1 SPAD device detail

4.1.1 Wafer structure

Layer
p^+: InGaAs ,10 nm, 5×10^{18} cm^{-3}
p^+: InAlAs, 300 nm, 5×10^{18} cm^{-3}
i : InAlGaAs, 50 nm,
i : InGaAs, 600 nm
i : InAlGaAs, 50 nm
p : InAlAs, 200 nm, 2×10^{17} cm^{-3}
i : InAlAs, 200 nm
n^+: InAlAs, 100 nm, 2×10^{18} cm^{-3}
n^+: InGaAs, 300 nm, 1×10^{19} cm^{-3}
InP semi-insulating substrate

Figure 4-1 Wafer structure of the InGaAs/InAlAs SPAD showing nominal thickness and doping concentration for each layer.

Nominal wafer details of the InGaAs/InAlAs SPADs (M3698) are shown in Figure 4-1. It was grown by molecular beam epitaxy (MBE) on a semi-insulating InP substrate at the EPSRC National Centre for III-V Technologies at the University of Sheffield. The

compositions of InGaAs and InAlAs were $In_{0.53}Ga_{0.47}As$ and $In_{0.52}Al_{0.48}As$ for lattice matching to InP.

The wafer consisted of a 600 nm InGaAs absorption layer and a 200 nm InAlAs avalanche layer. Both layers were undoped to maintain a uniform electric field throughout the layers. Compared to typical InGaAs/InP SPADs (shown in Figure 1-8), the InGaAs/InAlAs SPAD structure has the absorption layer placed near the p^+ cladding since InAlAs has higher ionisation coefficient for electrons than for holes(opposite in InP). The absorption and avalanche layers were thinner than those of InGaAs/InP SPADs in [1] and [2]. This allows us to achieve very small C_{bd}, by minimising both the avalanche layer width and the total depletion region width (made up of the avalanche layer, absorption layer, grading, and charge sheet). The thin absorption layer also makes it easier to achieve sufficiently low surface leakage currents from mesa devices. Another benefit of using thin avalanche and absorption layer is that lower timing jitter can be achieved which is desired by photon timing-related applications, although these advantages are at the expense of absorption efficiency.

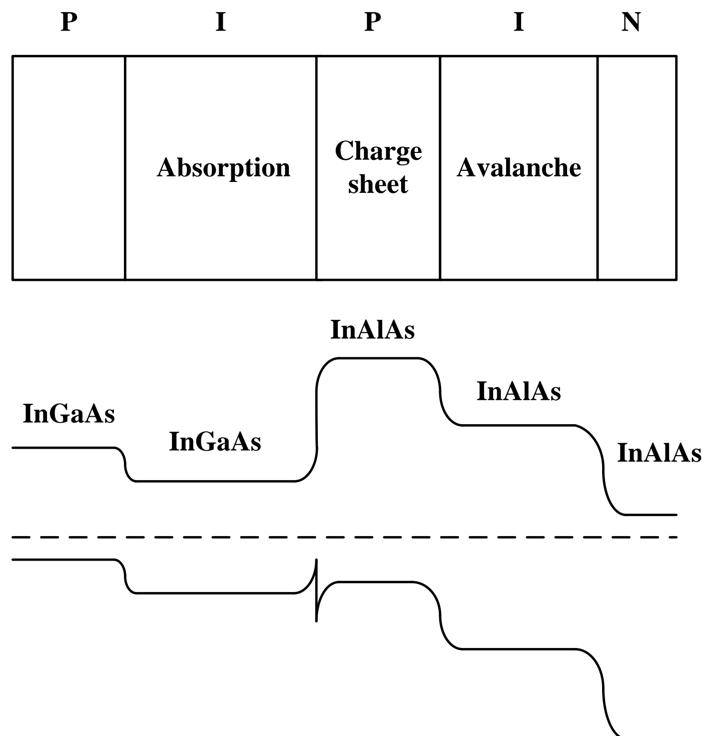

Figure 4-2 Simplified structure of an InGaAs/InAlAs SAMAPD with its band structure at zero bias.

An InAlAs charge sheet (or field control) layer was between the avalanche and absorption layers. This layer is used to ensure that the electric field in avalanche layer is high enough to result in avalanche breakdown while the electric field in absorption layer is low suppressing the tunnelling current. According to the differential form of Gauss's law, the electric field difference between avalanche and absorption layer is determined by the doping concentration and width of the charge sheet layer. Normally the electric field in absorption layer needs to be kept between 0 to 100 kV/cm when the avalanche layer reaches breakdown electric field.

Figure 4-2 shows that in an InGaAs/InAlAs SAMAPD there is a large conduction band offset in the InGaAs/InAlAs heterojunction. This will act an energy barrier which hinders the photo-generated electrons from travelling to the multiplication layer reducing the collection efficiency and hence the *SPDE*. Hence the SPAD design in Figure 4-1 uses two 50 nm $In_{0.53}Al_{0.29}Ga_{0.18}As$ layers, which are lattice-matched with both InAlAs and InGaAs and have intermediate bandgap, to achieve bandgap grading at the heterojunctions.

The top p^+-layer has a highly doped 10 nm InGaAs contact layer and a 300 nm p-type InAlAs cladding layer. The thin narrow bandgap InGaAs layer ensures good ohmic contact without attenuating the incident light significantly. A 300 nm wide bandgap InAlAs layer, which is transparent to the 1550 nm light, was used as the electric field stop layer. Similarly, the bottom n^+ layer consisted of a 100 nm n-type InAlAs cladding layer and a 300 nm n-type InGaAs contact layer.

4.1.2 Device fabrication

Mesa devices with diameters of 25 to 100 μm were fabricated from the wafer by Dr. Shiyu Xie using standard photolithography and wet chemical etching with a solution of sulphuric acid: hydrogen peroxide: deionised water (ratio of 1:8:80). Figure 4-3 shows the schematic of the mesa device cross section. The etching reached down to n^+ InGaAs layer for n-contact deposition.

The p-contacts were formed by thermal evaporation of Ti/Pt/Au with thickness of 10/30/200 nm. Ti was used to due to its good adhesion to semiconductor. Pt has a large work function which is necessary to form a good ohmic contact on the p-type InGaAs layer. P-contact metal was annealed at 420 ^{o}C for 30 seconds using rapid thermal

annealing (RTA) to further reduce the contact resistance. The doping concentration of InGaAs layer needs to be high in order to reduce the depletion width in the metal-semiconductor junction achieving lower contact resistivity. Annular contact was used for p-contact to enable top illumination. InGe/Au (20/200 nm) n-contacts were formed by thermal evaporation.

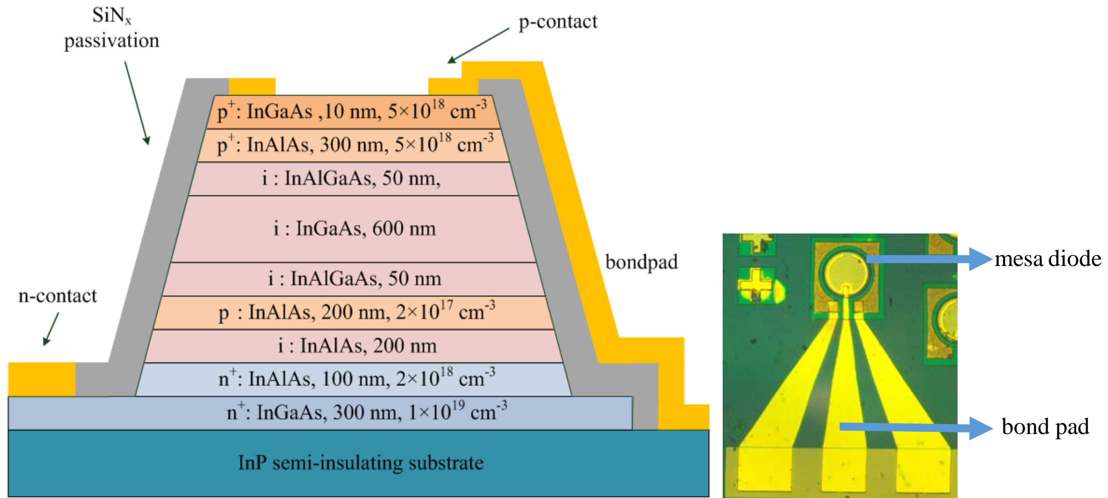

Figure 4-3 Cross-section of a fabricated InGaAs/InAlAs mesa diode and the photograph of the mesa diode with its bond pads.

Then an additional etch down to SI substrate was carried out to create an area for p- and n- bond pads deposition. Ti/Au bond pads were deposited on the semi-insulating substrate. 200 nm thick SiN_x was deposited by plasma-enhanced chemical vapor deposition (PECVD) at 300 °C to passivate the mesa diode and isolate the bond pads from the mesa edge. Reactive ion etching (RIE) was used to open the top optical window and bond pads. No anti-reflection coating was employed.

4.2 Device characterisation

4.2.1 I-V results

I-V measurements of the devices at temperatures ranging from 260 to 290 K were performed using a Janis ST-500 probe station connected to a Keithley Model 236 source-measure-unit. To obtain dark current and photocurrent data, the I-V measurements were conducted in the dark and with fibre-coupled CW 1550 nm light from an Agilent 8164A tunable laser source, respectively.

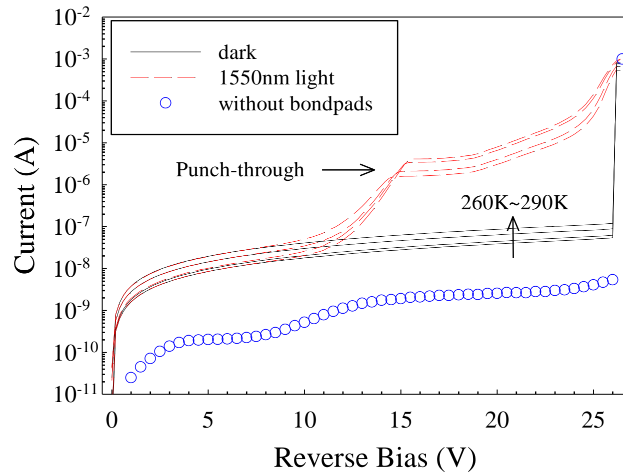

Figure 4-4 Reverse dark current and photocurrent (1550nm light) data of a 25 µm diameter InGaAs/InAlAs SPAD at 260 to 290 K. Dark current of a diode without p-layer bond pad at room temperature is also shown (circle).

Typical dark current and photocurrent data of a 25 µm diameter SPAD at temperatures from 260 to 290 K are shown in Figure 4-4. At bias voltage below 15 V, the photocurrent is low since the absorption layer is not depleted and the photo-generated carriers need to diffuse to the multiplication layer to be collected. As the bias increases to be higher than 15 V, the absorption layer is fully depleted, an increased collection efficiency of carriers lead to a step increase of the photocurrent. The photocurrent data showed similar punch-through voltages (~ 15 V) at different temperatures.

As the bias continues to increase, the photocurrent experiences avalanche multiplication and finally causes an avalanche breakdown at 26 V. For most of semiconductors, breakdown voltage decreases with a decrease of temperature because the ionisation coefficients increases at lower temperature due to reduced phonon scatterings. Also this temperature dependence of breakdown voltage becomes weaker for device with thin avalanche layer. Within the temperature range studied, the breakdown voltages indicated by dark current data varied by less than 0.2 V, consistent with the small C_{bd} expected from [3]. Thus, there was always at least 10 V difference between the breakdown voltage and punch-through voltage, ensuring that the absorption layer of SPAD is fully depleted at breakdown voltage even at low temperature. The dark current at 90% of breakdown voltage was 54 and 120 nA at 260 and 290 K, respectively.

Also included in Figure 4-4 is the room temperature leakage current of a 25 µm diameter diode without p-layer bond pad (from the same sample piece), which is at least an order of magnitude lower than that of the tested diode. This indicates that leakage current due to bond pads contributed significantly to the measured leakage current of the tested diode. This could be due to either leakage current from SI substrate or SiN_x passivation on the mesa sidewall. However the additional leakage currents are not expected to influence dark counts since they do not flow through the multiplication layer.

4.2.2 C-V results

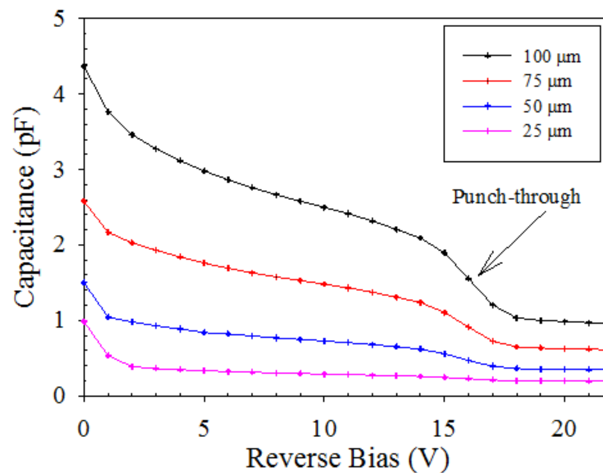

Figure 4-5 C-V data for different-sized InGaAs/InAlAs SPADs at room temperature.

C-V measurements of the mesa devices were carried out at room temperature using a HP4275 LCR meter. Figure 4-5 shows the capacitance results from diodes with diameter ranging from 25 to 100 µm. Small diode capacitance is preferred in photon counting measurement since transient pulses in the gated mode increases with the diode capacitance. The experimental capacitance decreased rapidly with reverse bias at ~ 15 V, because of the depletion of absorption layer. This is consistent with the increase in photocurrent at 15 V. Metal bond pads will introduce parasitic capacitance and add to the measured capacitance, which was estimated to be around 150 fF by comparing the measured capacitance of different-sized diodes.

By fitting to the C-V data using an electrostatic model and assuming abrupt changes in doping density from layer to layer, estimated doping profile and electric field profile of the SPAD were obtained. The fitting parameters are shown in Table 4-1. C-V data

from the largest diodes (100 μm diameter), as shown in Figure 4-6 was used in order to maximise accuracy in the measurement. The fitting is also shown in Figure 4-6.

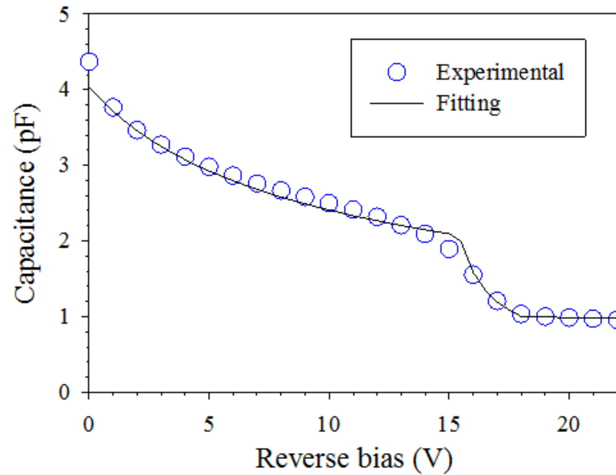

Figure 4-6 C-V data and fitting result for a 100 μm diameter InGaAs/InAlAs SPAD.

Table 4-1 Summary of parameters used to obtain C-V fitting shown in Figure 4-6

Layer	Material	Doping(cm^{-3})		Thickness(nm)	
		Nominal	Fitted	Nominal	Fitted
p^+ cap	InGaAs	5×10^{18}	5×10^{18}	10	10
p^+ cladding	InAlAs	$>5\times10^{18}$	5×10^{18}	300	300
Grading	$In_{0.53}Al_{0.29}Ga_{0.18}As$	undoped	1×10^{18}	50	50
i absorber	InGaAs	undoped	6×10^{15}	600	440
Grading	$In_{0.53}Al_{0.29}Ga_{0.18}As$	undoped	7×10^{15}	50	50
p charge sheet	InAlAs	2×10^{17}	1.8×10^{17}	200	200
i multiplication	InAlAs	undoped	1×10^{16}	200	200
n^+ cladding	InAlAs	$>5\times10^{18}$	2×10^{18}	100	100
n^+ etch stop	InGaAs	1×10^{19}	1×10^{19}	300	300

4.2.3 SPDE

For the photon counting measurement, the device-under-test was operated in gated mode and tested with the setup shown in Figure 3-2. The AC voltage pulses had 1.2 ns pulse width (*FWHM*), 6 V pulse height, and 100 kHz repetition frequency. The fixed AC voltage pulses ensured constant AC pulse width for all measurements. The avalanche

pulses triggered by either photons or dark carriers were monitored using a Lecroy Waverunner 204Xl oscilloscope during measurements, as shown in Figure 4-7. The 1550 nm pulsed laser was triggered at a frequency of 100 kHz, which was synchronised with the voltage pulses. The laser power was attenuated to single photon level ($\bar{n}$ = 0.3) using the method described in section 3.4.3.

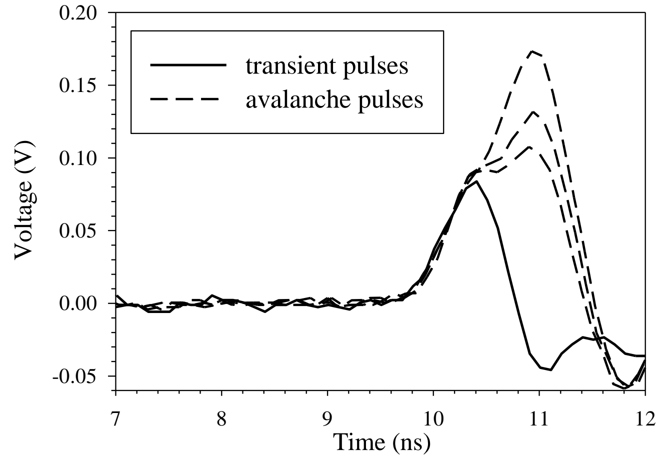

Figure 4-7 Avalanche pulses recorded using Lecroy Waverunner 204Xl oscilloscope.

Following the measurement procedures listed in Appendix A. P_t and P_d were measured, from which the *SPDE* was calculated using equation (3-17). *SPDE* versus DC bias obtained from the SPAD at temperatures of 260 to 290 K, are shown in Figure 4-8. *SPDE* of 10% at 290 K and 21% at 260 K were achieved. At each temperature, *SPDE* increases with overbias voltage due to the increased breakdown probability.

Absorption efficiency, P_{abs}, for a 600 nm InGaAs absorption layer is estimated at 0.39, assuming absorption coefficient of 0.82 μm^{-1} at 1550 nm [4]. *SPDE* is the product of P_{abs}, P_b, and (1 - P_{loss}), where P_{loss} is the probability that photo-generated carriers are lost before entering the avalanche layer. The small difference between the estimated P_{abs} (0.39) and the highest measured *SPDE* (0.10) at 290 K suggests a small P_{loss} and/or a high P_b at the operating conditions used. This is supported by the P_b ~ 0.4 to 0.5 predicted for a 200 nm InAlAs avalanche layer with the conditions used to achieve *SPDE* of 21 % [5].

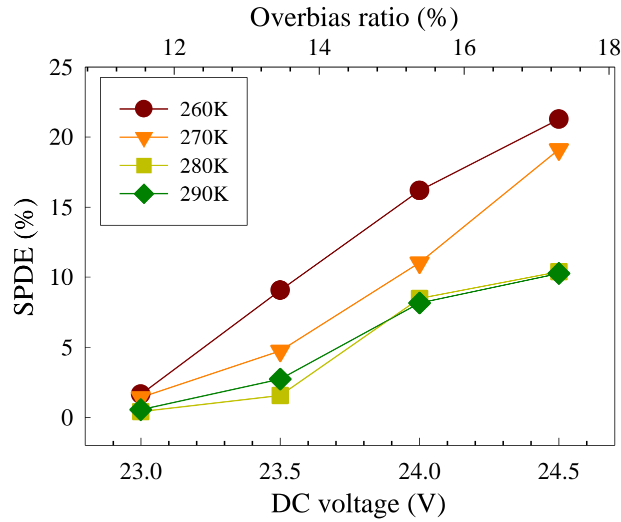

Figure 4-8 SPDE versus DC bias for the SPAD at 260 to 290 K.

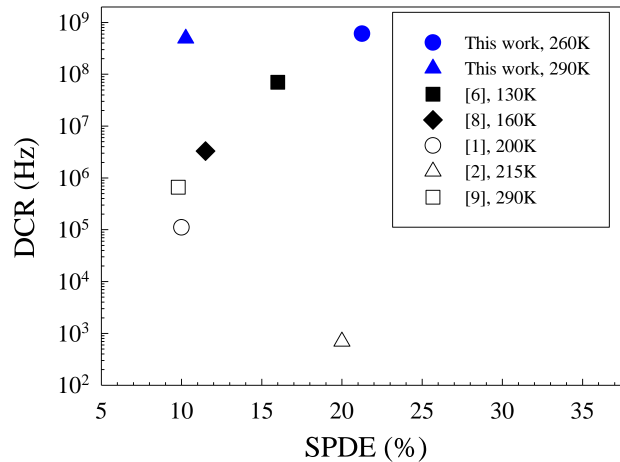

Figure 4-9 DCR vs SPDE results in this work compared with previous reports of InGaAs/InAlAs (closed symbols) and InGaAs/InP SPADs (open symbols).

The measured *SPDE* values are significantly higher than the *SPDE* values previously reported for InGaAs/InAlAs SPADs [6-8] and are approaching or exceeding those for InGaAs/InP SPADs [1, 2, 9] as shown in Figure 4-9. Thus, mesa structure InGaAs/InAlAs SPADs represent a practical alternative to InGaAs/InP SPADs. The former may be particularly advantageous for development of dense arrays of SPADs.

4.2.4 DCR

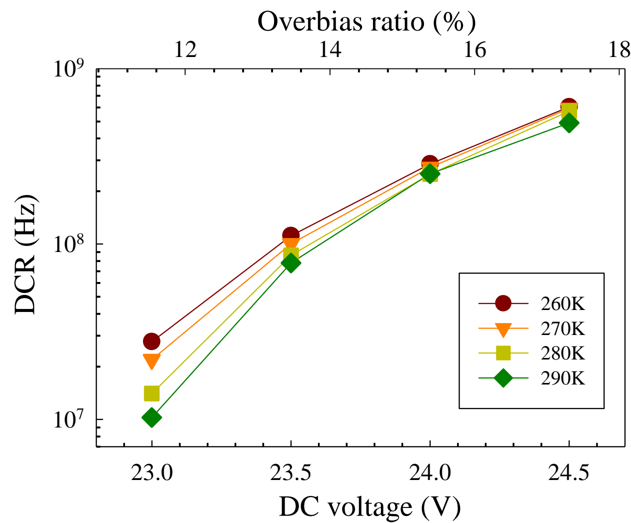

Figure 4-10 DCR versus DC bias for the SPAD at 260 to 290 K.

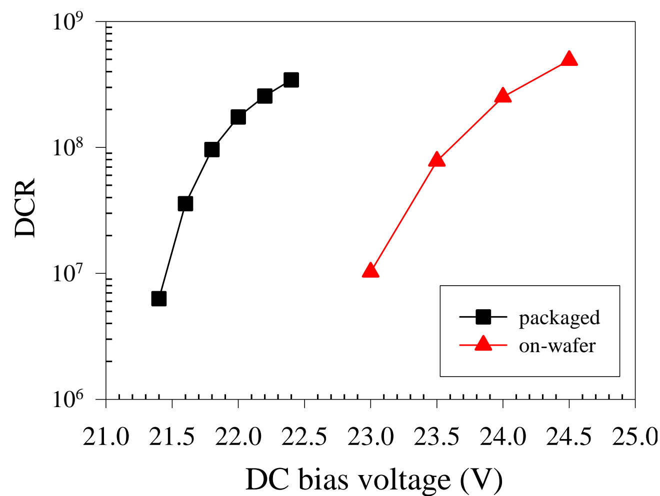

Figure 4-11 Comparison of DCR results from on-wafer and packaged SPADs. AC bias pulses used for both devices are 6 V.

From Figure 4-10, for a given bias condition, *DCR* was observed to increase marginally as temperature decreases. This is likely to be the result of competing effects on *DCR* from tunnelling current and avalanche breakdown probability. As temperature decreases, the BTB tunnelling current in the InAlAs layer decreases slightly, because the semiconductor material bandgap increases slightly (increasing the tunnelling barrier height). However, as temperature decreases, V_{bd} of the SPAD decreases slightly, which may result in a slight increase in P_b and hence *DCR*, for a given voltage.

A device from the same sample piece as the DUT was packaged and characterised with a setup similar to the one shown in Figure 3-2 (an differential amplifier was added to suppress the increased transient pulses due to added parasitic capacitance from the TO header). IV results from the packaged device shown identical breakdown voltage (26 V) with the DUT. In Figure 4-11, *DCR* results from the on-wafer DUT and packaged device show very similar increase over DC bias voltage. However, to reach the same *DCR* value, DUT needs ~ 1.5 V more bias voltage than the packaged device. This is possibly due to the biasing signal loss caused by long cable between device and biasing circuit and/or reflection at the probe/device interface.

Figure 4-9 shows that the *DCR* of this work is higher than those for prior works on InGaAs/InAlAs SPADs, namely [6] (7×10^{7} s^{-1} at 130 K) and [8] (3×10^{6} s^{-1} at 160 K), as well as for the *DCR* reported for InGaAs/InP SPADs (e.g. ~ 10^{4} s^{-1} at 253 K from [10]). There was no sufficient information in [7] to extract its *DCR*. The *DCR* data are insensitive to changes in temperatures within the range studied. This suggests that the dominant mechanism is unlikely to be diffusion or generation recombination current, both of which increase exponentially with temperature. BTB tunnelling current, which depends weakly on temperature, is thus a possible significant source of dark carrier generation.

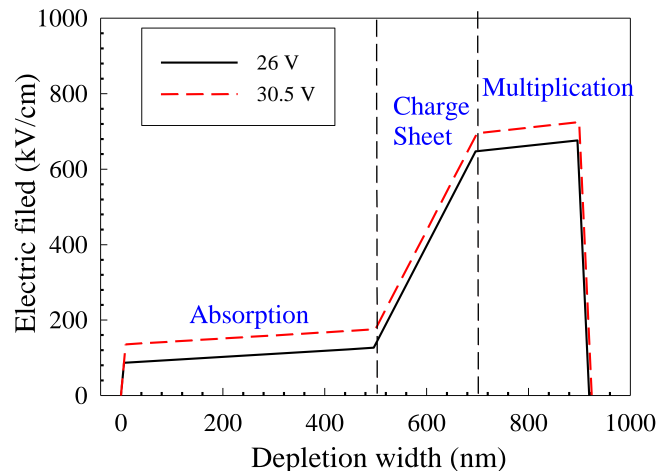

Figure 4-12 Calculated electric field profiles at 26 and 30.5 V.

In order to assess the significance of BTB tunnelling current in the SPAD, electric field profiles were calculated for 26 and 30.5 V. These are the breakdown voltage and

maximum voltage applied in the measurements, respectively. The field profiles are shown in Figure 4-12.

The peak electric field in the InAlAs avalanche layer reaches 725 kV/cm at 30.5 V. Such fields were shown to cause significant BTB tunnelling current for a 200 nm InAlAs avalanche layer [11]. Hence the high *DCR* of the SPAD is attributed to excessive tunnelling current from the InAlAs avalanche layer.

4.2.5 Afterpulsing

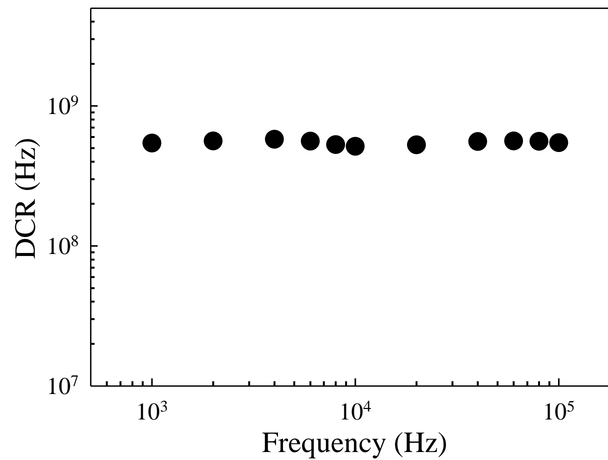

Figure 4-13 DCR of the SPAD versus AC voltage pulse repetition frequency at room temperature with 4.5 V overbias. No after-pulse problem was observed.

Since SPADs sensitive to 1550 nm light can suffer from significant after-pulse problem, dark counts measurements were repeated at room temperature for *f* ranging from 1 to 100 kHz (the maximum repetition frequency of the pulse generator). The data for 4.5 V overbias (24.5 V DC with 6 V AC bias) are shown in Figure 4-13. No significant dependence on frequency could be observed, confirming afterpulsing is not the dominant source of the dark counts within this temperature range.

4.3 Summary

Mesa structure SPADs using InGaAs absorption layer and InAlAs avalanche layer have been designed, fabricated and characterised. The 25 µm diameter SPAD was demonstrated to have good temperature stability (< 0.2 V change over 30 K). In gated mode, the *SPDE* of 10% and 21% was achieved at 290 K and 260 K, respectively.

However high *DCR* over the temperature range studied was observed and its temperature insensitivity implies its origin being tunnelling current. This is supported by the electric field profile estimation for the avalanche layer. Further improvements, such as thicker avalanche layer, will be necessary to reduce the breakdown electric field in the InAlAs layer. No noticeable after-pulse problem was observed in the frequency range (up to 100 kHz) studied. Overall the results indicate InGaAs/InAlAs has considerable potential for operation at (or near) room temperature.

4.4 References

[1] S. Pellegrini, R. E. Warburton, L. J. J. Tan, N. Jo Shien, A. B. Krysa, K. Groom, *et al.*, "Design and performance of an InGaAs-InP single-photon avalanche diode detector," *Quantum Electronics, IEEE Journal of,* vol. 42, pp. 397-403, 2006.

[2] M. A. Itzler, X. Jiang, M. Entwistle, K. Slomkowski, A. Tosi, F. Acerbi, *et al.*, "Advances in InGaAsP-based avalanche diode single photon detectors," *Journal of Modern Optics,* vol. 58, pp. 174-200, 2011.

[3] L. J. J. Tan, D. S. G. Ong, N. Jo Shien, T. Chee Hing, S. K. Jones, Q. Yahong, *et al.*, "Temperature Dependence of Avalanche Breakdown in InP and InAlAs," *Quantum Electronics, IEEE Journal of,* vol. 46, pp. 1153-1157, 2010.

[4] D. A. Humphreys, R. J. King, D. Jenkins, and A. J. Moseley, "Measurement of absorption coefficients of $Ga_{0.47}In_{0.53}As$ over the wavelength range 1.0-1.7 μm," *Electronics Letters,* vol. 21, pp. 1187-1189, 1985.

[5] S. C. Liew Tat Mun, C. H. Tan, S. J. Dimler, L. J. J. Tan, J. S. Ng, Y. L. Goh, *et al.*, "A Theoretical Comparison of the Breakdown Behavior of $In_{0.52}Al_{0.48}As$ and InP Near-Infrared Single-Photon Avalanche Photodiodes," *Quantum Electronics, IEEE Journal of,* vol. 45, pp. 566-571, 2009.

[6] G. Karve, X. Zheng, X. Zhang, X. Li, S. Wang, F. Ma, *et al.*, "Geiger mode operation of an $In_{0.53}Ga_{0.47}As$-$In_{0.52}Al_{0.48}As$ avalanche photodiode," *Quantum Electronics, IEEE Journal of,* vol. 39, pp. 1281-1286, 2003.

[7] T. Nakata, E. Mizuki, T. Tsukuda, S. Takahashi, H. Hatakeyama, T. Anan, *et al.*, "InAlAs avalanche photodiodes for gated Geiger mode single photon counting," in *OptoElectronics and Communications Conference (OECC), 2010 15th*, 2010, pp. 822-823.

[8] K. Zhao, S. You, J. Cheng, and Y.-h. Lo, "Self-quenching and self-recovering InGaAs / InAlAs single photon avalanche detector," *Applied Physics Letters,* vol. 93, p. 153504, 2008.

[9] L. Yan, Y. Jian, C. Xiuliang, W. Guang, E. Wu, and H. Zeng, "Room-Temperature Single-Photon Detector Based on InGaAs/InP Avalanche Photodiode With Multichannel Counting Ability," *Photonics Technology Letters, IEEE,* vol. 23, pp. 115-117, 2011.

[10] Y. Zhang, X. Zhang, and S. Wang, "Gaussian pulse gated InGaAs/InP avalanche photodiode for single photon detection," *Optics Letters,* vol. 38, pp. 606-608, 2013.

[11] Y. L. Goh, D. J. Massey, A. R. J. Marshall, J. S. Ng, C. H. Tan, W. K. Ng, *et al.*, "Avalanche Multiplication in InAlAs," *Electron Devices, IEEE Transactions on,* vol. 54, pp. 11-16, 2007.

5 InGaAs/InAlAs SPADs with improved performances

An InGaAs/InAlAs SPAD with promising *SPDE* at near room temperatures and very small temperature coefficient of breakdown voltage was presented in the previous chapter. Nevertheless, the SPAD exhibited high *DCR* caused by BTB tunnelling current in the thin avalanche layer. In this chapter, the design, fabrication and characterisation of an improved InGaAs/InAlAs SPAD are presented.

5.1 Design criteria

The thickness of avalanche layer is one of the crucial parameters in the SPAD design, because the electric field required to achieve avalanche breakdown is very sensitive to the avalanche thickness, which in turn has influence on many performance factors of the SPAD. For instance, a thicker avalanche layer will result in lower breakdown electric field and hence lower tunnelling current in avalanche layer. Meanwhile, the timing jitter will be larger due to the longer transit time and smaller k value [1]. Also higher operating voltage will be required since breakdown voltage increases with avalanche layer thickness. In addition, temperature dependence of breakdown voltage is greater in SPADs with thicker avalanche layers [2].

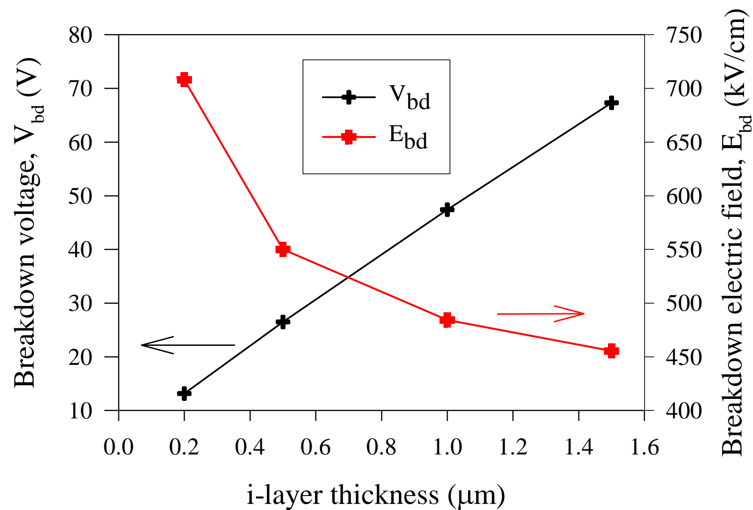

Figure 5-1 Breakdown voltage and electric field for InAlAs p-i-n diodes with different i-layer thickness.

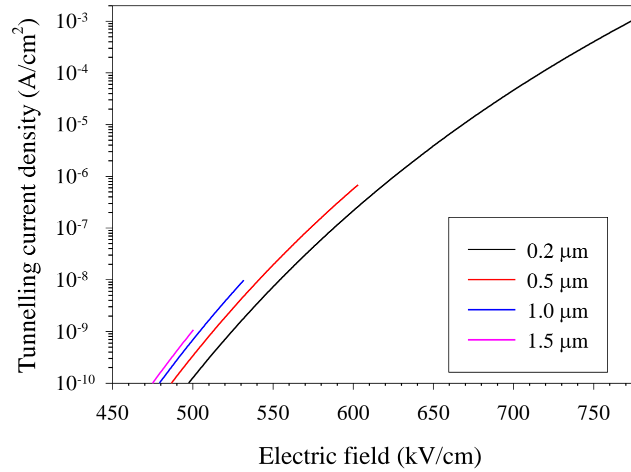

Figure 5-2 Tunnelling current calculated for InAlAs p-i-n diodes with different i-layer thickness.

In order to make a decision on what avalanche layer thickness to choose, V_{bd} and breakdown electric field (E_{bd}) of an InAlAs p-i-n diode with i-layer thickness of 0.2, 0.5, 1.0 and 1.5 μm was estimated from avalanche gain simulation, as shown in Figure 5-1. V_{bd} and E_{bd} are defined as the voltage and electric field at which the avalanche gain is 100, respectively. The ionisation coefficients used are from ref. [3]. From Figure 5-1 it can be seen that E_{bd} decreases from 700 kV/cm for 0.2 μm i-layer thickness to 450 kV/cm for 1.5 μm i-layer thickness. This is due to the fact that thinner avalanche layer needs higher electric field to achieve the same average gain as the thicker avalanche layer. BTB tunnelling currents versus electric field for each avalanche layer thickness were also calculated. Figure 5-2 shows the calculated tunnelling current for different avalanche layer thickness. Tunnelling current was calculated using equation (1) with a fitting parameter value (α_T) of 1.26 in ref. [4]. The tunnelling current curves for each thickness end at the voltage of $1.1\times V_{bd}$, which is sufficient to achieve high P_b (0.8 to 0.9, for avalanche layer thickness of 0.2 to 1.0 μm, [5]). It is clear that as the i-layer thickness increases from 0.2 to 1.0 μm the tunnelling current at $1.1\times V_{bd}$ reduces by five orders of magnitude, with less dramatic decrease for further increase in avalanche thickness. On the other hand, the breakdown voltage increases almost linearly with i-layer thickness (V_{bd} will be even higher when absorption layer is taken into consideration). Higher V_{bd} will require higher operating voltage, increasing the height of capacitive transient pulses and complicating the measurement. So there is a trade-off between lower tunnelling current and lower operating voltage. The device investigated in this chapter has an avalanche layer

thickness (w_{ava}) of 1.0 µm, which offers a reasonable compromise in having a reasonably low operating voltage while avoid excessive tunnelling current.

The thickness of absorption layer determines the absorption efficiency and hence the *SPDE* of the SPAD. Figure 5-3 shows the calculated absorption efficiency for an InGaAs layer with different thickness, using absorption coefficient reported in ref. [6]. Thicker absorption layer will give high absorption efficiency, however, the thermal generation current will also be higher for thick device. So the choice of absorption layer thickness will be a results of trade-off between high *SPDE* and high *DCR*. Moreover, thicker absorption layer will also increase the risk of having undepleted absorption layer if low background doping is not assured. Considering above factors, absorption layer thickness (w_{abs}) of 1.7 µm was chosen, which gives reasonably high absorption efficiency (75 %).

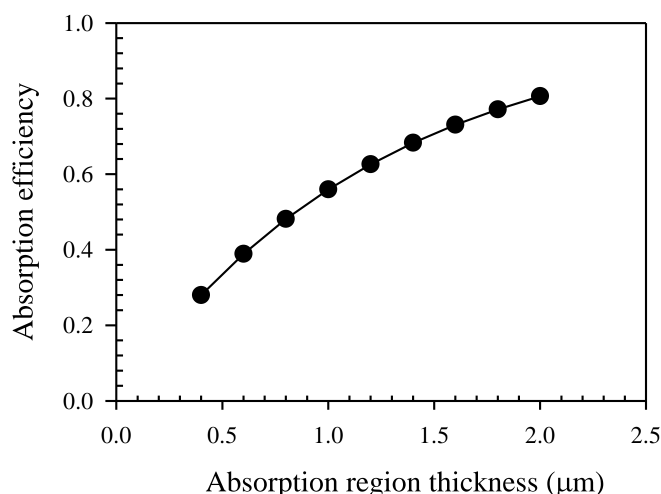

Figure 5-3 Absorption efficiency of InGaAs layers with different thickness.

The electric field in InGaAs absorption layer need to be low to reduce the field-related dark carrier generation mechanisms (e.g. tunnelling and field-assisted thermal generation). For an InGaAs p-i-n diode with 1.7 µm i-layer thickness, using the BTB tunnelling current equation and fitting parameter constant of 1.34 in ref. [7], the tunnelling current density is 10 nA/cm^2 (the tunnelling current density of a 1.0 µm InAlAs p-i-n diode at reverse bias of $1.1\times V_{bd}$) at electric field of 165 kV/cm. This places an upper limit of the electric field in InGaAs.

Since the SPAD might need to be cooled to reduce the thermal generation current, the decrease of breakdown voltage (V_b) at lower temperature might result in undepleted absorption layer during breakdown. To avoid this problem, there should be ~ 10 V difference between the V_{bd} and V_p to enable measurement down to 100 K. This sets the lower limit of electric field in InGaAs. The 10 V difference is calculated as the product of temperature coefficient of V_b, 50 mV/K, as calculated using equations (1b) and (2) in [2] and a temperature difference of 200 K.

Therefore, the design of SPAD requires that, when the InAlAs layer reaches its $1.1\times E_{bd}$,, the electric field in the InGaAs layer is < 165 kV/cm and the (V_{bd} - V_p) > 10 V. Electric field profile calculations (using electrostatic model) were performed to work out the desirable doping density and thickness for the charge sheet, N_c and w_c, respectively. The key parameters used were w_{ava} = 1.0 µm, w_{abs} = 1.7 µm, E_{bd} = 484 kV/cm, and $N_c = 3.85\times10^{17}$ cm^{-3}. The values of V_{bd}, V_p and E_{ab} at $1.1\times E_{bd}$ versus w_c are plotted in Figure 5-4. The lower and upper limits of w_c are indicated by the red lines in the plot.

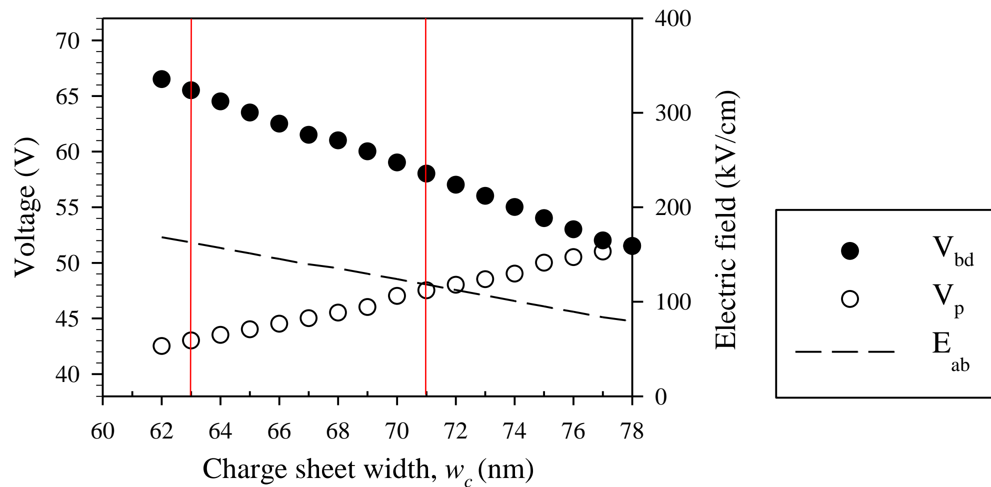

Figure 5-4 Calculated V_{bd}, V_p and E_{ab} using the electrostatic model with design parameters versus different charge sheet width.

5.2 Growth and fabrication

The InGaAs/InAlAs SPAD (SF0817) was grown by MBE on a semi-insulating InP substrate by Dr. Shiyong Zhang at the EPSRC National Centre for III-V Technologies at the University of Sheffield. As shown in Figure 5-5, the wafer consisted of a 1700

nm InGaAs absorption layer and a 1000 nm InAlAs avalanche layer. Compared to the design used in chapter 4, the wafer had thicker absorption and avalanche layers, increasing the photon absorption efficiency and reducing the tunnelling current from InAlAs, respectively. A thin InAlAs charge sheet layer with high doping density (> 1×10^{17} cm^{-3}) was used to achieve a large difference in the electric fields in absorption layer and avalanche layer. InAlGaAs layers with intermediate bandgaps were included for bandgap grading at InGaAs/InAlAs heterojunctions.

Top-illuminated mesa devices with diameters of 10 to 50 μm were fabricated from the wafer using standard photolithography and wet chemical etching with a solution of sulphuric acid: hydrogen peroxide: deionized water (ratio of 1:8:80). The p-contacts and n-contacts were formed by annealed metals of Ti/Pt/Au (10/30/200 nm). The devices were passivated by silicon nitride deposited using PECVD at 150 ºC. Bond pads to the p- and n-contacts were formed by depositing Ti/Au (10/500 nm). No anti-reflection coating was applied. Results shown in following sections were obtained from the 25 μm diameter SPADs, which is the typical size for commercial SPADs at 1550 nm.

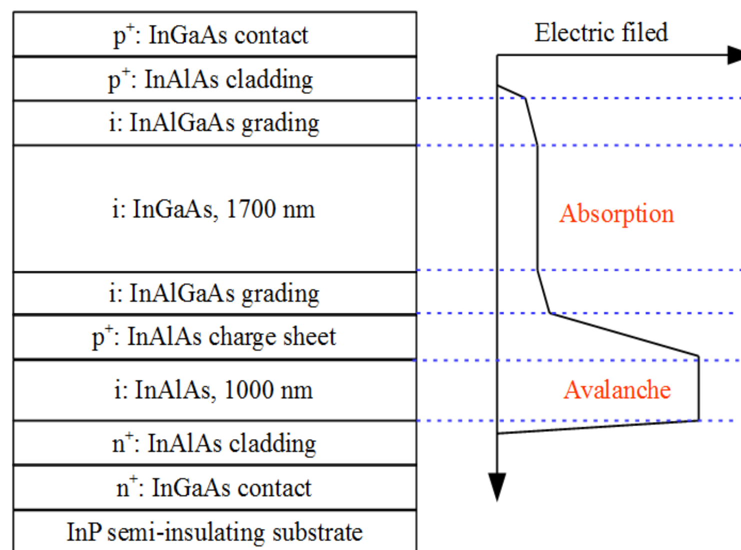

Figure 5-5 Structure details and electric field profile of InGaAs/InAlAs SPAD.

5.3 Characterisation results

Figure 5-6(a) shows the typical dark I-V data of a 25 μm diameter SPAD at temperatures from 210 to 293 K as well as the photocurrent at 210 K when the SPAD

was illuminated with a 1550 nm continuous-wave laser with ~ 40 nW power. The dark current at 95% of breakdown voltage was 17 pA and 2.6 nA at 210 and 293 K, respectively. The photocurrent data indicate a punch-through voltage, the minimum voltage to fully deplete the entire SPAD structure, of ~ 42 V. At room temperature the responsivity of the SPAD at punch-through voltage is 0.7 A/W, giving an external quantum efficiency of 56 %. This gives an upper limit of 56 % for *SPDE* (because probability of photo-generated carriers reach the avalanche layer and probability of avalanche breakdown do not exceed unity).

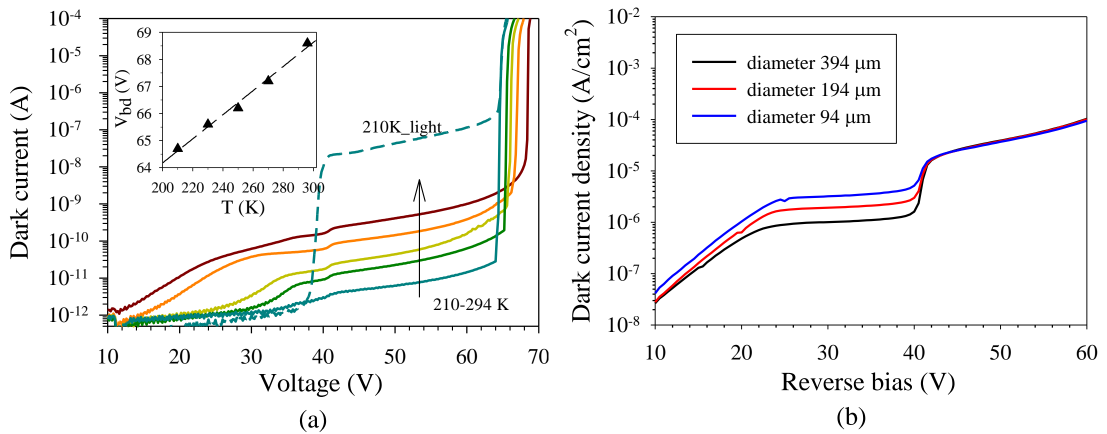

Figure 5-6 (a) Dark currents (solid lines) of a 25 μm diameter InGaAs/InAlAs SPAD at 210, 230,250, 270, and 294 K (bottom to top). Photocurrent (dashed line) at 210 K when the SPAD is illuminated with 1550 nm laser with optical power of ~ 40 nW. Inset: Breakdown voltage versus temperature. (b) Dark current density of SPADs with diameter of 94, 194 and 394 μm fabricated in a separate fabrication run. These diameter values were obtained from results shown in Figure 5-7(b).

Plotting breakdown voltage (the voltage at which current reaches 10 μA) from the dark I-V data versus temperature in the inset of Figure 5-6(a), its temperature coefficient was found to be 45 mV/K. This is close to the design value (50 mV/K), and about half of that obtained from InGaAs/InP SPADs (~ 100 mV/K [8]). This small C_{bd} ensures that the breakdown voltage is always higher than the punch-through voltage, over the temperature studied in this work.

Based on dark current measurements on large diodes with diameters of 94 to 394 μm shown in Figure 5-6(b), we estimated bulk dark current density at punch-through voltage to be 20 μA/cm^2. This is supported by bulk dark current density data from another InGaAs p-i-n diode wafer (grown under highly similar conditions), which yield 23 μA/cm^2 at 0.5 V reverse bias.

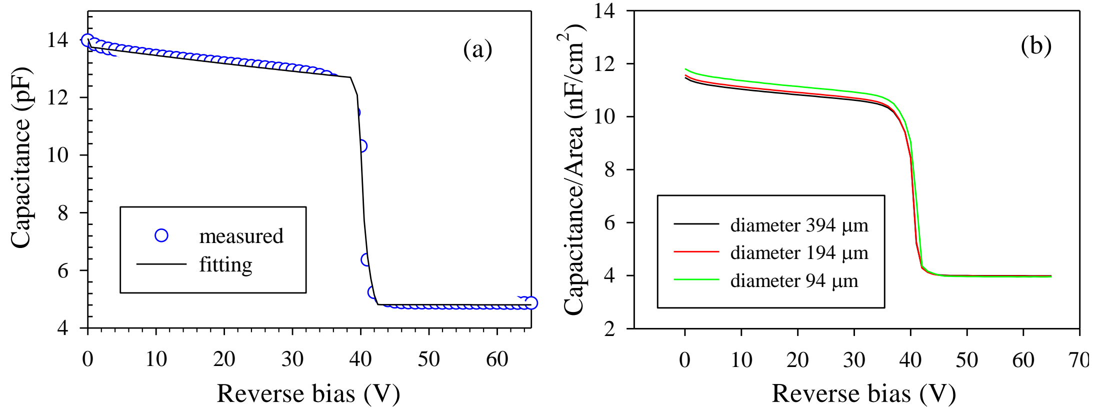

Figure 5-7 (a) C-V data measured from a 394 μm diameter SPAD (symbol) and the fitted result (line). (b) Capacitance divided by area results of different-sized SPADs. Diameters used for calculation are 394, 194 and 94 μm.

Table 5-1 Summary of parameters used in C-V fitting shown in Figure 5-7(a).

<table>
<tr><th rowspan="2">Layer</th><th rowspan="2">Material</th><th colspan="2">Doping(cm^{-3})</th><th colspan="2">Thickness(nm)</th></tr>
<tr><th>Nominal</th><th>Fitted</th><th>Nominal</th><th>Fitted</th></tr>
<tr><td>p$^+$ cap</td><td>InGaAs</td><td>1×10^{19}</td><td></td><td>100</td><td></td></tr>
<tr><td>p$^+$ cladding</td><td>InAlAs</td><td>2×10^{18}</td><td>2×10^{18}</td><td>100</td><td>100</td></tr>
<tr><td>grading</td><td>InAlAs</td><td>undoped</td><td rowspan="4">5.2×10^{14}</td><td>100</td><td rowspan="4">1850</td></tr>
<tr><td>grading</td><td>$In_{0.53}Al_{0.29}Ga_{0.18}As$</td><td>undoped</td><td>25</td></tr>
<tr><td>grading</td><td>$In_{0.53}Al_{0.15}Ga_{0.32}As$</td><td>undoped</td><td>25</td></tr>
<tr><td>i absorber</td><td>InGaAs</td><td>undoped</td><td>1700</td></tr>
<tr><td>grading</td><td>$In_{0.53}Al_{0.15}Ga_{0.32}As$</td><td>undoped</td><td rowspan="3">1.1×10^{16}</td><td>25</td><td rowspan="3">75</td></tr>
<tr><td>grading</td><td>$In_{0.53}Al_{0.29}Ga_{0.18}As$</td><td>undoped</td><td>25</td></tr>
<tr><td>grading</td><td>InAlAs</td><td>undoped</td><td>25</td></tr>
<tr><td>p charge sheet</td><td>InAlAs</td><td>3.85×10^{17}</td><td>3.78×10^{17}</td><td>69</td><td>69</td></tr>
<tr><td>i multiplication</td><td>InAlAs</td><td>undoped</td><td>1.5×10^{15}</td><td>1000</td><td>980</td></tr>
<tr><td>n$^+$ cladding</td><td>InAlAs</td><td>2×10^{18}</td><td>2×10^{18}</td><td>100</td><td>100</td></tr>
<tr><td>n$^+$ etch stop</td><td>InGaAs</td><td>5×10^{18}</td><td>1×10^{19}</td><td>1000</td><td></td></tr>
</table>

C-V data from a 394 μm diameter SPAD are shown in Figure 5-7(a). By doing C-V fitting using model described in section 3.2 (fitted results also shown in Figure 5-7(a)), the doping concentration and thickness of the main layers were deduced, as shown in Table 5-1. For the C-V fitting, corrected diameters instead of the nominal values were used (i.e. 394, 194 and 94 μm instead of 400, 200 and 100 μm). The 6 μm

difference was deduced from comparison of the capacitance scaled by diode area from different-sized diodes, as shown in Figure 5-7(b). Having ~ 6 µm reduction in diameter is expected because the etching used in the SPAD device fabrication was isotropic.

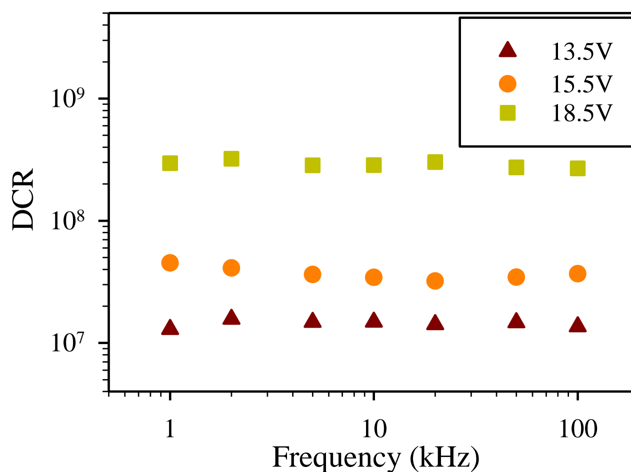

Figure 5-8 DCR versus repetition frequency of the AC pulse at different overbias voltages.

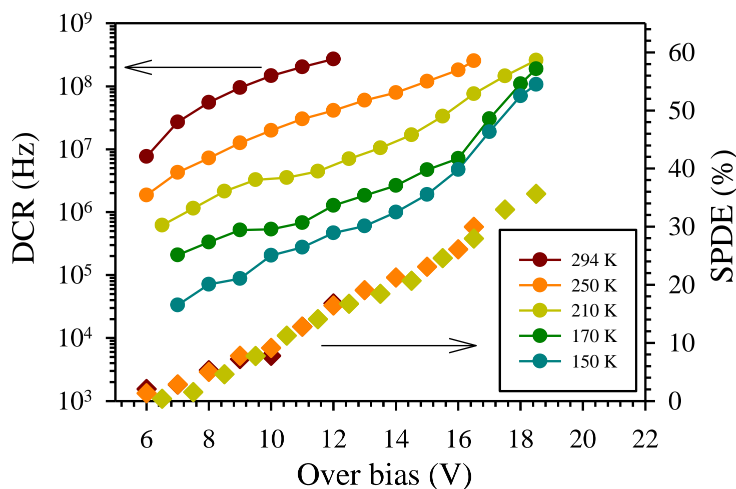

Figure 5-9 DCR and SPDE versus overbias voltage at different temperatures (150 to 294 K).

Selection of the frequency of the electrical pulses for subsequent characterisation was based on measurements of *DCR* versus frequency ranging from 1 kHz to 100 kHz (maximum operating frequency of the pulser), as a function of overbias. The data obtained from our device at 210 K, with overbias up to 18.5 V, are shown in Figure 5-8. The data were not dependent on frequency so afterpulsing effect was negligible. This is expected because the narrow AC pulses used limit the total number of carriers generated during an avalanche breakdown event, and hence the number of trapped

carriers, which are responsible for afterpulsing effect. Repetition frequency of 100 and 10 kHz were used at operating temperatures from 210 to 294 K and from 150 to 170 K.

DCR and *SPDE* versus overbias of the device are plotted as functions of temperature in Figure 5-9. At 293 K, the highest *SPDE* achieved is 17%. Cooling the SPAD down to 210 K reduces the *DCR* at 12 V overbias by nearly two orders of magnitude, indicating that the *DCR* is not dominated by tunnelling currents from avalanche layer as results in chapter 4. The lower *DCR* at 210 K allows higher overbias voltage to be applied, yielding *SPDE* as high as 36 %.

Possible origins of the dark counts were investigated through deduction of activation energy. Activation energy for the *DCR* at two temperature ranges, 150 to 210 K and 250 to 293 K, were obtained from linear fittings to $ln(DCR)$ versus $1/kT$ characteristics, as shown in Figure 5-10. Activation energies of ~ 0.1 and 0.3 eV were deduced for the two temperature ranges, respectively, for overbias upto 12 V (corresponding to *SPDE* upto ~ 15%). An activation energy of 0.3 eV for the higher temperatures is consistent with those reported on InGaAs/InP SPADs at similar temperature range [9-11] (0.3 to 0.5 eV), which are attributed to thermal generation current in the InGaAs absorption layer. At lower temperatures, the lower activation energy indicates that the dominant origin of dark counts is likely to be tunnelling-related mechanism [11], which is less temperature dependent and more prominent at low temperatures [12]. Furthermore, the increase in activation energy with temperature is in line with the general trend of other works, including refs. [10, 11].

Observing Figure 5-10, as overbias increases, the activation energy decreases down to ~ 0.04 eV at the highest overbias used. This is likely to be caused by tunnelling-related current growing in significance with overbias. This is similar to the observation made by Karve et al., who found their InGaAs/InAlAs SPADs with high band-to-band tunnelling current from the InAlAs avalanche layer exhibiting a small activation energy (0.12-0.15 eV) even at high temperatures (up to 280 K). However, it does not necessarily mean that the same dominant dark count mechanism applies to our SPAD at high overbias, because other tunnelling-related mechanisms, such as TAT, can also give rise to very small activation energy.

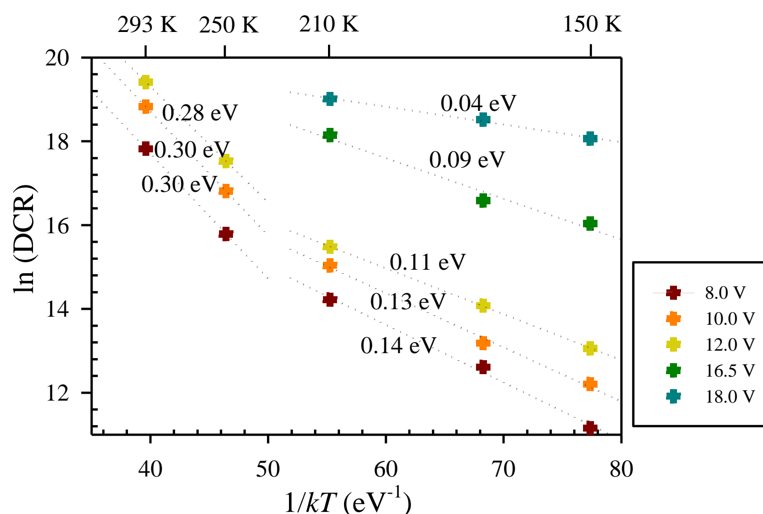

Figure 5-10 ln(DCR) plotted as a function of 1/kT at different overbias voltages.

5.4 Comparison with other reports

DCR and *SPDE* of this work are compared to results from various reports on InGaAs/InAlAs SPADs [13, 14] and InGaAs/InP SPADs [8, 15, 16] in Figure 5-11. Compared with the previous InGaAs/InAlAs SPAD in chapter 4, this work demonstrates significantly improved maximum *SPDE* (from 21% to 36%) and reduced *DCR* (~ two orders of magnitude) for a given SPDE. The increase in maximum *SPDE* is attributed to the thicker absorption layer (1700 nm instead of 600 nm) that gives higher absorption efficiency and *SPDE*. The thicker avalanche layer is responsible for the reduction in *DCR*.

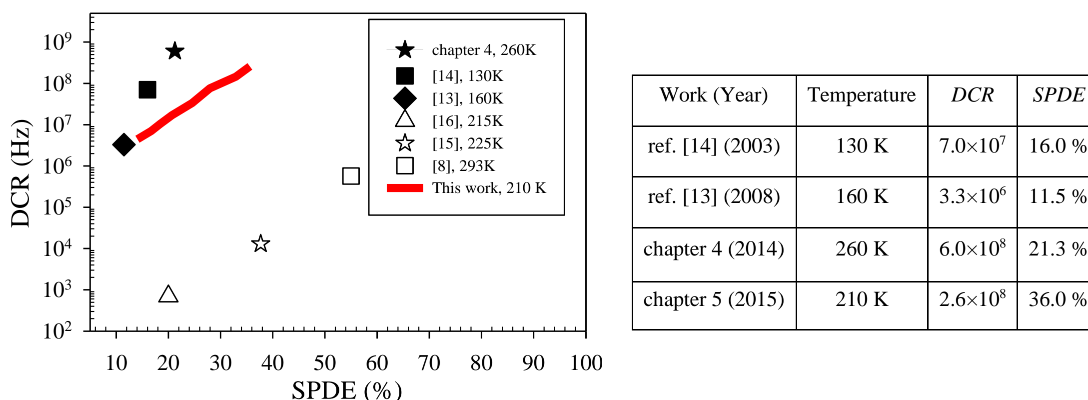

Work (Year)	Temperature	*DCR*	*SPDE*
ref. [14] (2003)	130 K	7.0×10^{7}	16.0 %
ref. [13] (2008)	160 K	3.3×10^{6}	11.5 %
chapter 4 (2014)	260 K	6.0×10^{8}	21.3 %
chapter 5 (2015)	210 K	2.6×10^{8}	36.0 %

Figure 5-11 Left: comparison of DCR versus SPDE results of InGaAs/InAlAs (closed symbols) and InGaAs/InP (open symbols) SPADs from various works. Right: progress in the development of InGaAs/InAlAs SPADs.

In comparison with other works, this work reports the highest *SPDE* among all InGaAs/InAlAs SPADs, while being competitive with the recent InGaAs/InP SPADs with impressive *SPDE* [8, 15]. However, the *DCR* values remain much higher than those of InGaAs/InP SPADs. This is in part related to the quality of InGaAs layer in our device. The bulk dark current density of our SPADs (20 μA/cm^2) is more than two orders of magnitude higher than typical values from commercially available InGaAs photodiodes at low reverse bias (~ 0.1 μA/cm^2).

5.5 Summary

InGaAs/InAlAs SPADs with 1.7 μm thick absorption layer and 1.0 μm thick avalanche layer have been demonstrated with promising *SPDE* value (36%). They also exhibit C_{bd} value that is only half of that of InGaAs/InP, offering greater flexibility in the SPAD operation temperature. Through a study on the dependence of *DCR* on temperatures (from 250 to 294 K), the measured *DCR* was attributed to thermal generation current in InGaAs layer. However, at temperatures below 210 K, tunnelling-related mechanism is the dominant origin of *DCR*. The design criteria described should continue to provide guidance in future design of InGaAs/InAlAs SPADs.

5.6 References

[1] C. H. Tan, J. S. Ng, G. J. Rees, and J. P. R. David, "Statistics of Avalanche Current Buildup Time in Single-Photon Avalanche Diodes," *Selected Topics in Quantum Electronics, IEEE Journal of,* vol. 13, pp. 906-910, 2007.

[2] L. J. J. Tan, D. S. G. Ong, J. S. Ng, C. H. Tan, S. K. Jones, Y. Qian*, et al.*, "Temperature Dependence of Avalanche Breakdown in InP and InAlAs," *Quantum Electronics, IEEE Journal of,* vol. 46, pp. 1153-1157, 2010.

[3] S. C. Liew Tat Mun, C. H. Tan, Y. L. Goh, A. R. J. Marshall, and J. P. R. David, "Modeling of avalanche multiplication and excess noise factor in $In_{0.52}Al_{0.48}As$ avalanche photodiodes using a simple Monte Carlo model," *Journal of Applied Physics,* vol. 104, p. 013114, 2008.

[4] Y. L. Goh, D. J. Massey, A. R. J. Marshall, J. S. Ng, C. H. Tan, W. K. Ng*, et al.*, "Avalanche Multiplication in InAlAs," *Electron Devices, IEEE Transactions on,* vol. 54, pp. 11-16, 2007.

[5] S. C. Liew Tat Mun, C. H. Tan, S. J. Dimler, L. J. J. Tan, J. S. Ng, Y. L. Goh*, et al.*, "A Theoretical Comparison of the Breakdown Behavior of $In_{0.52}Al_{0.48}As$ and InP Near-Infrared Single-Photon Avalanche Photodiodes," *Quantum Electronics, IEEE Journal of,* vol. 45, pp. 566-571, 2009.

[6] D. A. Humphreys, R. J. King, D. Jenkins, and A. J. Moseley, "Measurement of absorption coefficients of $Ga_{0.47}In_{0.53}As$ over the wavelength range 1.0-1.7 μm," *Electronics Letters,* vol. 21, pp. 1187-1189, 1985.

[7] Y. L. Goh, "Impact Ionisation in InGaAs, InAlAs and InGaAs/GaAsSb Superlattices for Near Infrared Avalanche Photodetectors," PhD thesis, University of Sheffield, 2008.

[8] L. C. Comandar, B. Fröhlich, J. F. Dynes, A. W. Sharpe, M. Lucamarini, Z. L. Yuan, *et al.*, "Gigahertz-gated InGaAs/InP single-photon detector with detection efficiency exceeding 55% at 1550 nm," *Journal of Applied Physics,* vol. 117, p. 083109, 2015.

[9] M. Liu, C. Hu, X. Bai, X. Guo, J. C. Campbell, Z. Pan, *et al.*, "High-Performance InGaAs/InP Single-Photon Avalanche Photodiode," *Selected Topics in Quantum Electronics, IEEE Journal of,* vol. 13, pp. 887-894, 2007.

[10] M. A. Itzler, R. Ben-Michael, X. Jiang, and K. Slomkowski, "Geiger-Mode Avalanche Photodiodes for Near-Infrared Photon Counting," in *Lasers and Electro-Optics, 2007. CLEO 2007. Conference on*, 2007, pp. 1-2.

[11] J. Zhang, R. Thew, J. D. Gautier, N. Gisin, and H. Zbinden, "Comprehensive Characterization of InGaAs/InP Avalanche Photodiodes at 1550 nm With an Active Quenching ASIC," *Quantum Electronics, IEEE Journal of,* vol. 45, pp. 792-799, 2009.

[12] F. Acerbi, M. Anti, A. Tosi, and F. Zappa, "Design Criteria for InGaAs/InP Single-Photon Avalanche Diode," *Photonics Journal, IEEE,* vol. 5, pp. 6800209-6800209, 2013.

[13] K. Zhao, S. You, J. Cheng, and Y. Lo, "Self-quenching and self-recovering InGaAs / InAlAs single photon avalanche detector," *Applied Physics Letters,* vol. 93, p. 153504, 2008.

[14] G. Karve, X. Zheng, X. Zhang, X. Li, S. Wang, F. Ma, *et al.*, "Geiger mode operation of an $In_{0.53}Ga_{0.47}As$-$In_{0.52}Al_{0.48}As$ avalanche photodiode," *Quantum Electronics, IEEE Journal of,* vol. 39, pp. 1281-1286, 2003.

[15] A. Tosi, N. Calandri, M. Sanzaro, and F. Acerbi, "Low-Noise, Low-Jitter, High Detection Efficiency InGaAs/InP Single-Photon Avalanche Diode," *Selected Topics in Quantum Electronics, IEEE Journal of,* vol. 20, pp. 192-197, 2014.

[16] M. A. Itzler, X. Jiang, M. Entwistle, K. Slomkowski, A. Tosi, F. Acerbi, *et al.*, "Advances in InGaAsP-based avalanche diode single photon detectors," *Journal of Modern Optics,* vol. 58, pp. 174-200, 2011.

6 InAs APD X-ray detector

6.1 Introduction

Measurement of X-ray fluorescence with Si detectors is an established technique to perform elemental analysis in a wide range of applications, such as treatments of liquid hazardous wastes [1], environmental analysis of water and soil samples [2], in vivo tests on human patients [3], and food safety assessments [4]. The elements of interest often include heavy metals, such as Hg and Pb, requiring X-ray photon detection up to 80 keV. On the other hand, some toxic elements, such as Li and Be, emit X-rays that are < 100 eV in energy.

Although Si is the dominant material used to make soft X-ray detectors, the energy resolution of current commercial Si X-ray detectors is approaching its Fano limit. For example, an Amptek Si drift detector (SDD) has an energy resolution of 125 eV at 5.9 keV [5], while Fano-limited energy resolution is 118 eV (calculated assuming 3.65 eV electron-hole-pair creation energy and 0.117 Fano factor [6]). Moreover, Si has a relatively small atomic number and crystal density, limiting its absorption coefficient at high X-ray energies. Thus alternative semiconductor materials to achieve low Fano-limited energy resolution and high absorption efficiency are desirable.

These criteria are met by certain compound semiconductors with narrow band gaps, E_g, such as InSb (E_g = 0.17 eV [7]) and InAs (E_g = 0.35 eV [8]). They have relatively high atomic numbers (49/51 for InSb and 49/33 for InAs) and densities (5.78 g/cm^3 for InSb and 5.68 g/cm^3 for InAs [9]). Some progress has been made in using these narrow band gap materials for X-ray detectors.

InSb Schottky diodes fabricated from epitaxially grown crystals had been studied as radiation detectors [10-12]. Cooling the Schottky diode to 42 K, alpha particles (5.5 MeV in energy) were detected with 1.8 % *FWHM* [12]. These diodes also detected Gamma rays (59.5 keV in energy), however the gamma ray peaks were not resolved, due to noise caused by the extremely high detector's leakage currents even at cryogenic temperatures [10],[11]. In addition, in order to minimise the leakage current, the detectors were operated without bias, causing undesirably narrow depletion region and hence low collection efficiency. In another work, Zn diffusion was employed to fabricate InAs p-n

diodes, which detected alpha particles when cooled by liquid nitrogen, but again high detector's leakage currents prohibited energy resolution assessment [13].

Si APDs have been extensively investigated for X-ray detection and demonstrated an energy resolution of 360 eV at 5.9 keV at -20 ºC [14]. There are also reports of APDs made with a wide bandgap material, $Al_{0.8}Ga_{0.2}As$, showing promising results at room temperature (or elevated temperatures) [15], [16]. The improvement in SNR is brought by the APD's avalanche gain, when the signal is weak and/or the amplifier's noise is dominant. Both conditions apply to soft X-ray detection applications, where fewer EHPs are created by each photon compared to X-rays with higher energies. Having an appreciable M may improve the $FWHM$ of the detected peak, with very little negative effect from the associated avalanche noise (often known as excess noise), if the APD is appropriately designed [17]. Appropriate designs need to be guided by the impact ionisation properties of the semiconductor materials used. As an example, consider an avalanche material with $\alpha > \beta$, i.e. electrons yield higher gain than holes. Then the X-ray photons need to enter the APD from its p-layer, so that the majority of photo-generated carriers initiating the avalanche gain are electrons, rather than holes. This will ensure that the avalanche gain applicable to the photo-generated carriers is as high as practically possible.

An InAs APD with an n-i-p structure for X-ray detection has been previously reported [18]. When cooled to 77 K, $FWHM$ of the 5.9 keV peak reduced from 2.02 keV to 950 eV, as M increased from 1.58 to 5.3. This represented a significant progress in semiconductor APDs made with narrow bandgap materials for X-ray detection, given that other works on InSb and InAs X-ray detectors were and are still hindered by leakage currents. However, since $\alpha > \beta$ in InAs, an InAs APD requires a p-i-n structure to maximise the value of M experienced by the absorbed X-ray photons for a given reverse bias. Furthermore, the n-i-p structure led to considerable absorption in the n-layer and avalanche layer, degrading the peak-to-background ratio in the X-ray spectra [18]. Thus appropriate changes to InAs APD designs can bring further improvements in their X-ray detection performance. In this chapter, the soft X-ray detection performance of InAs APDs with p-i-n structure is reported, followed by a comparison between InAs APDs with p-i-n and n-i-p structure.

6.2 Device detail and electrical characterisation

The InAs APDs were fabricated from an InAs p-i-n diode wafer (SF0810) grown on a 2” n-type InAs substrate by molecular beam epitaxy by wafer grower Dr. Shiyong Zhang. Be and Si were used as the p- and n-type dopants respectively. The wafer structure, shown schematically in Figure 6-1(a), consisted of a 300 nm p-layer, a 3.5 µm InAs layer with graded p-doping, a 6.0 µm InAs i-layer and a 1.0 µm InAs n-layer. The 3.5 µm InAs layer had doping grading (light to heavy from bottom to top) to help improve collection of minority electrons originally generated by X-ray photon absorption within the p-layer. In addition, a very thin $AlAs_{0.16}Sb_{0.84}$ p^+-layer was included to reduce diffusion of electrons from the p-contact into the graded, reducing the bulk leakage current.

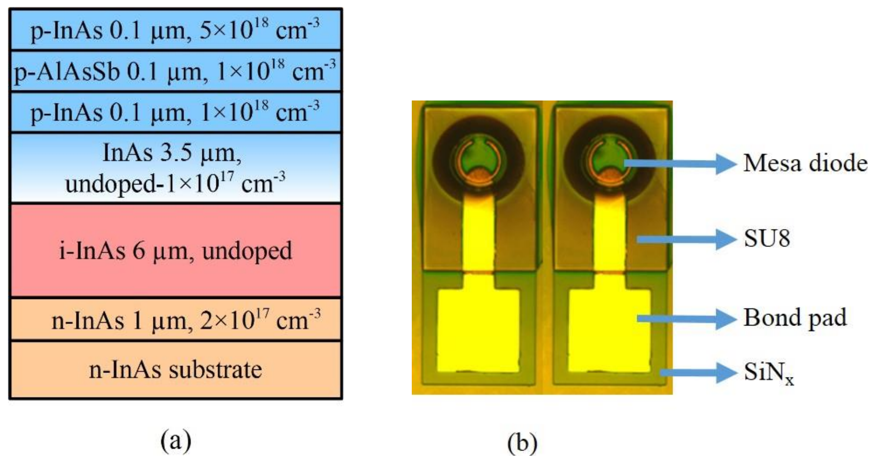

Figure 6-1 (a) Wafer structure of the InAs APD, showing the thickness and doping concentration for each layer. (b) Photograph of the mesa APD and its bond pad.

Standard photolithography and wet chemical etching were used to create circular mesa diodes from the wafer (fabrication was done by Dr. Xinxin Zhou at the National III-V centre, Sheffield). Ti/Au (20/200 nm) were deposited to form p- and n- contacts for the diodes. The main wet chemical etchant used was a mixture of phosphoric acid, hydrogen peroxide and de-ionised water (ratio of 1: 1: 1). The main mesa etching was followed by finishing etches using a solution of sulphuric acid, hydrogen peroxide and de-ionised water (ratio of 1: 8: 80) [19], and diluted hydrofluoric acid. Sidewalls of the mesas were then passivated with negative photoresist SU8, minimizing surface leakage currents degradation [20]. SiN_x was then deposited before the final step of bond pad deposition. The device fabrication yielded diodes with diameters ranging from 15 to 200 µm. The 75 µm diameter diodes, whose top view is shown in Figure 6-1(b), offered the

best trade-off between minimizing capacitance and maximizing the sensitive area for X-ray detection. Hence X-ray data presented later were obtained from diodes with 75 μm diameter, which were wire-bonded onto TO-5 packages to facilitate low temperature X-ray measurements.

The vast majority of the characterizations were carried out on two packaged InAs APDs, namely D1 and D2. Prior to X-ray measurements, reverse leakage currents of D1 and D2 were measured at room temperature, as shown in Figure 6-2(a). At room temperature, due to the narrow band gap of InAs, the diodes' reverse leakage currents are prohibitively high. Comparison with on-wafer measurement data also indicates degradation in leakage currents caused by the packaging process. Cooling the device to 77 K reduces the bulk leakage current significantly [20], also shown in Figure 6-2(a), making the detection of X-rays possible. On-wafer Capacitance-Voltage dependence of the 75 μm diameter InAs APD at 77 K, plotted in Figure 6-2(b), showed that the capacitance decreased rapidly with reverse bias voltage from zero to 4 V, but remained relatively unchanged for higher reverse bias (0.18 pF at 10 V).

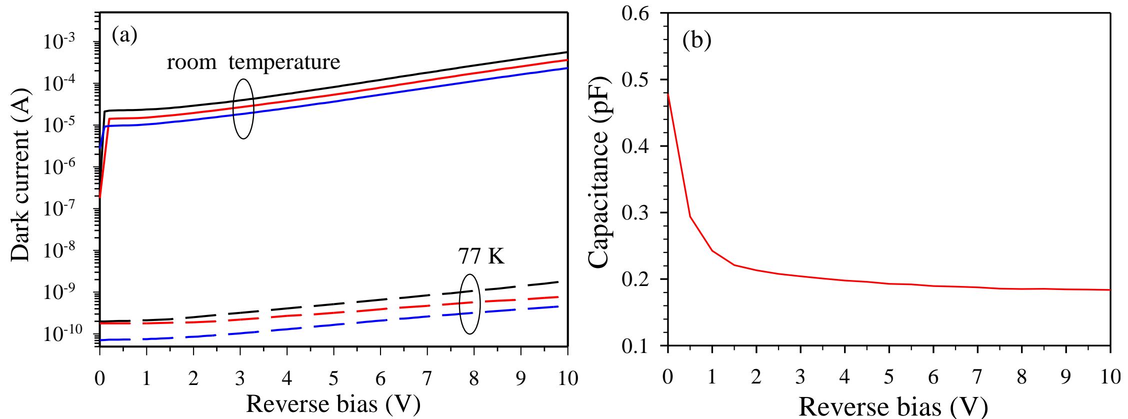

Figure 6-2 (a) Reverse leakage current of packaged InAs APDs with 75 μm diameter at room temperature (solid lines) and 77 K (dashed lines). Data from TO-5 packages (black for D1 and red for D2) are higher than those from on-wafer measurements (blue line). (b) Capacitance-Voltage curve from on-wafer measurements at 77 K.

6.3 X-ray response

In the X-ray measurement setup, a TO-5 package containing the InAs APD was mounted onto the cold plate of a liquid nitrogen dewar to cool the APD down to ~ 77 K. A ^{55}Fe radioisotope with ~ 40 MBq activity was the irradiation source. The measurement setup used is described in section 3.5. Spectra obtained with different shaping time

constants were compared, as shown in Figure 6-3. Shaping time constant of 0.5 μs gave the narrowest peak so was selected for subsequent X-ray measurements. The acquisition time was 360 seconds for all measurements.

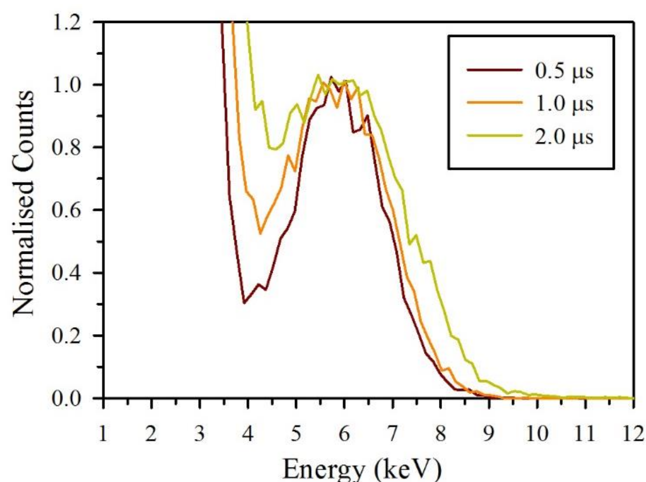

Figure 6-3 Energy spectra collected using D2 with different shaping time constants.

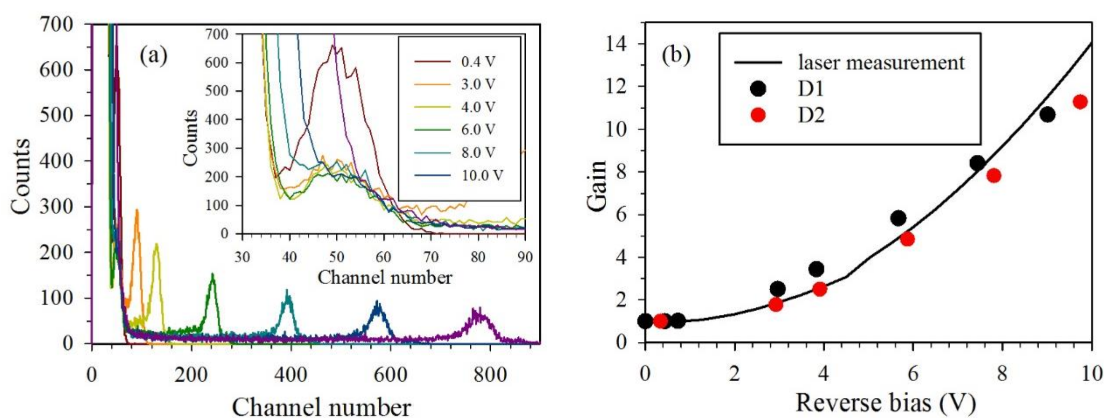

Figure 6-4 (a) Spectra in channel numbers collected using APD D2 cooled to 77K, at reverse bias voltages from 0.4 to 10.0 V. Inset: same data from channels 30 to 90. (b) Avalanche gain obtained from X-ray spectra of the InAs APDs at 77 K, in agreement with that from 1550 nm laser measurements.

Figure 6-4(a) shows the ^{55}Fe spectra collected using the cooled APD D2, reverse biased at different voltages. The 5.9 keV energy peaks can be observed in all spectra. The peak position at a bias voltage of 0.4 V (channel 50) was assigned as the unity gain peak, because the peak position did not vary from 0 to 0.6 V reverse bias (data not shown here). As reverse bias voltage is increased beyond 0.6 V, the energy peak shifts to higher channel number, moving away from the noise peak, which is expected for an APD. Inset of Figure 6-4(a) shows the unity gain peak (channel 50) in the spectra at 3.0, 4.0 and 6.0 V reverse bias voltages. As reverse bias increased beyond 6 V, it was increasingly

difficult to resolve the unity gain peak from the growing noise peak (attributed to increasing leakage current shown in Figure 6-2(a)).

For spectra at reverse bias voltages of 3.0, 4.0 and 6.0 V, the peak at channel 50 can be attributed to the fraction of incident X-ray photons absorbed in the InAs n-layer. These correspond to pure hole injection and the charge would experience an avalanche gain of M_h. For InAs APDs, M_h remains at unity for the entire range of reverse bias considered for this work [19]. Thus these unity gain peaks are expected to be present in the spectra for all reverse bias voltages. X-rays absorbed solely in the InAs p-layer will undergo a gain of M_e, which gives rise to the shifted main peak. Absorption of X-ray photons within the InAs i-layer will give rise to an avalanche gain of M_{mix}, whose values range between unity and M_e, which accounts for the majority of the events between the M_h and M_e peaks, Figure 6-4(a). Photon absorption in this region is clearly undesirable since it widens the main M_e peak, degrading the energy resolution.

Ratio of the channel number of shifted peaks to the unity gain channel number (50) gives M_e as a function of reverse bias, as shown in Figure 6-4(b). The results are compared to M_e data obtained using conventional photomultiplication measurements (photocurrent measurement with a 1550 nm laser as photon source) on a device from the same sample. The two sets of data are in agreement, confirming that the shifted peaks were indeed due to avalanche gain.

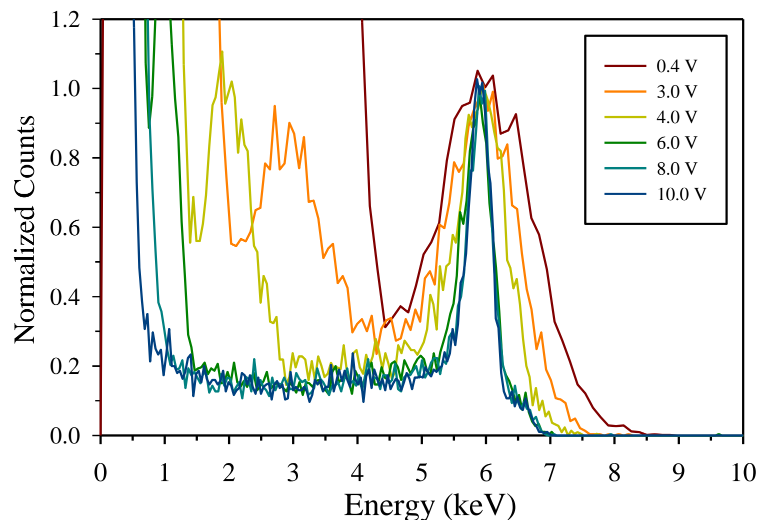

Figure 6-5 Energy spectra collected using the APD D2 cooled to 77 K, at reverse bias voltages from 0.4 to 10.0 V.

With the noise peak (channel number 11) and 5.9 keV peak (channel number varies due to varying M_e) as references, the spectra in Figure 6-4(a) were also converted from channel numbers into energy. The resultant normalised spectra for different reverse bias voltages are compared in Figure 6-5. As reverse bias voltage increases, the energy peak becomes narrower, with better energy resolution. Meanwhile, the influence of noise tail is diminishing due to the positive effect of avalanche gain, achieving an overall increased signal to noise ratio. Note that for different bias voltages the calibrated spectra have different bin size in energy (spectrum at higher bias has smaller bin size) making the spectra at higher bias seem artificially noisier than those at lower bias. To overcome this artefact, data for different bias voltages were further processed to have identical bin size to energy resolution ratio (6%).

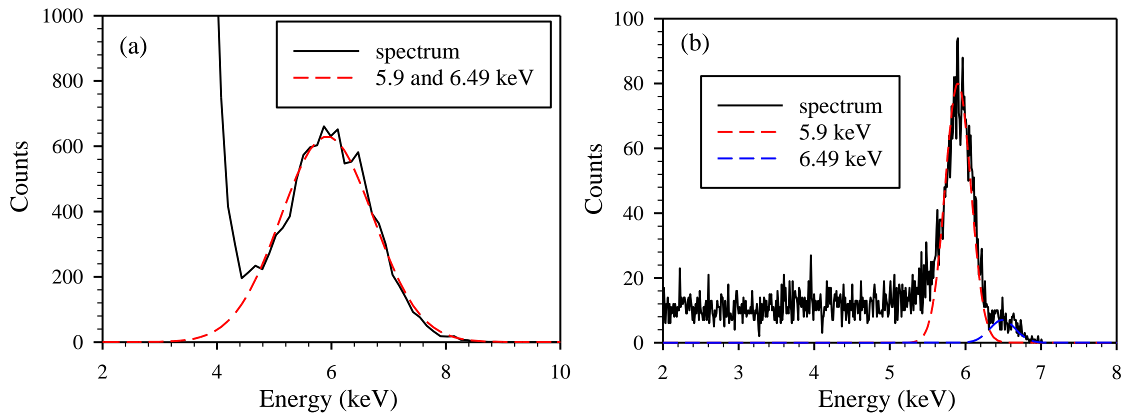

Figure 6-6 Gaussian fitting for spectra obtained from APD D2 biased at (a) 0.4 V and (b) 10.0 V.

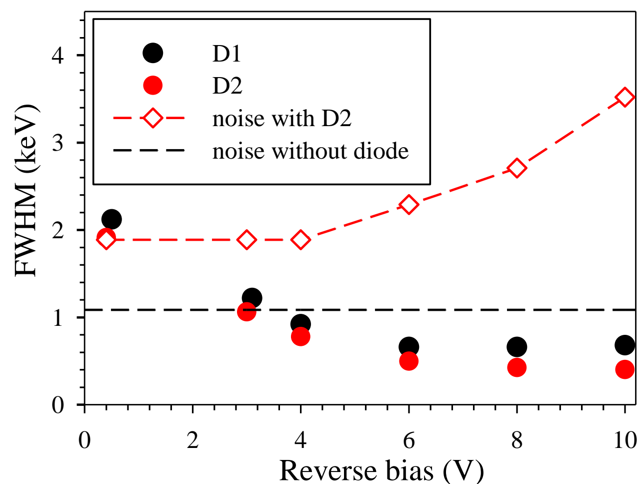

Figure 6-7 Energy resolution (FWHM) versus reverse bias from ^{55}Fe spectra measured with APDs D1 and D2. Noise value obtained with and without detector are also shown.

Gaussian fitting to data in Figure 6-5 yields *FWHM* values for the 5.9 keV peaks in each spectra (examples of Gaussian fitting shown in Figure 6-6). The deduced *FWHM* versus reverse bias of the InAs APDs is shown in Figure 6-7. For APD D1, *FWHM* reduces from 2.12 keV at 0.5 V to a minimum of 660 eV at 6 V. APD D2 exhibits even smaller *FWHM*, a minimum of 401 eV at 10 V, which is significantly smaller than the value of 950 eV from ref. [18]. The decreasing *FWHM* with reverse bias observed from figure 6 is attributed to increasing *M* that reduces the effect of electronic noise, which is one of the dominant noise sources at small reverse bias. Reduction in *FWHM* with reverse bias is less significant at higher reverse bias, or even reversed in the case of APD D1, which is most likely caused by the increasing APD dark current, which grew in significance as a noise source (as seen in Figure 6-2(a) and discussed later in section 6.4). The better energy resolution of D2 (compared to D1) was attributed to its lower leakage current at the operating temperature, as shown in Figure 6-2(a).

6.4 Noise analysis

To assess in detail the significance of electronic noise to the measured energy resolution, measurements were conducted to assess the noise of the X-ray detection experimental setup used. To facilitate the noise measurements, a few modifications were made to the setup. The X-ray source was absent and square wave signals (from a pulse generator) were fed into a test capacitor (0.5 pF) within the preamplifier. The InAs APD (D2) remained connected to the input of the preamplifier, so that the noise contributions from detector leakage current and capacitance were included in the noise measurements. Data were also taken without the detector to allow assessment of the influence of leakage current of the setup noise.

The noise spectra obtained with or without APD D2 at different reverse bias voltages, calibrated using the same references used for the 0.4 V data in figure 5, are compared in Figure 6-8. Unsurprisingly, it shows peaks widened with reverse bias (beyond 4.0 V), since leakage current continues to increase but capacitance remains relatively constant beyond 4.0 V. Then the *FWHM* values associated with these peaks, again obtained through Gaussian peak fitting, are plotted in Figure 6-7 for comparison with the values from X-ray peaks.

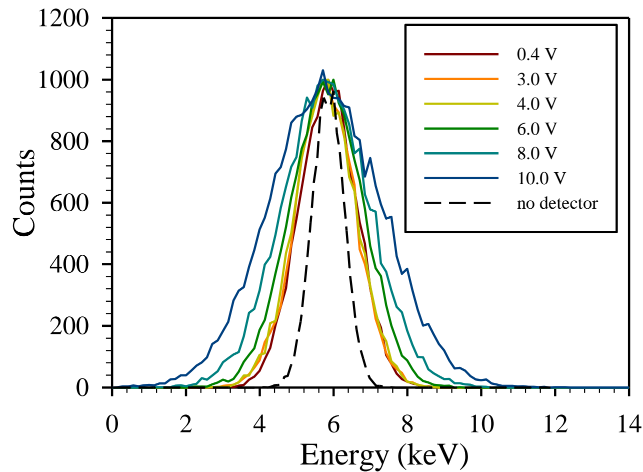

Figure 6-8 Energy spectra from noise measurements obtained with APD D2 at different reverse bias voltages. Noise spectrum taken without the detector is also shown.

The advantage of having avalanche gain without excessive leakage current is illustrated clearly in the comparison in Figure 6-7. At 0.4 V (no avalanche gain), the small difference between the *FWHM* values from X-ray peaks and noise measurements are likely to be caused by fluctuations in the number of EHP created and incomplete collection of carriers created by photon absorption in the partially depleted InAs i-layer. *FWHM* from the X-ray peak reduces quickly with reverse bias up to 4 V, above which *FWHM* from noise starts to increase due to increased leakage current. Despite this, the APD's avalanche gain continues to significantly reduce the detrimental effect of electronics noise (3.52 keV at 10 V), achieving an overall energy resolution of 401 eV.

6.5 Comparison of InAs p-i-n and n-i-p diodes

In addition to the InAs APDs with p-i-n structure presented above, measurements were also carried out on an InAs APD with n-i-p structure (D3) to allow straightforward comparison, which offer valuable insights. Table 6-1 summarises the basic characteristics of the APD D1 and D3 at 10 V reverse bias at 77 K. They have identical InAs i-layer thickness as designed and similar dark current. However the actual depletion region is wider (calculated from capacitance data shown in Figure 6-9) in APD D1 than in APD D3, due to differences in unintentional doping in the InAs i-layers. Also, the structure of APD D3 does not have doping grading in the p-layer.

Table 6-1 Characteristics of the packaged InAs APDs with p-i-n or n-i-p structure at 10 V reverse bias and 77 K.

	APD D1	APD D3
Wafer number	SF0810	MR3234
Main layer thickness (μm)	3.5/6.0/1.0 (p/i/n)	2.0/6.0/2.0 (n/i/p)
Device diameter (μm)	75	103.5
Dark current (nA)	1.9	1.2
On-wafer device capacitance (pF)	0.18	0.45
Depletion width (μm)	7.7	3.4
FWHM (keV) at 5.9 keV	0.68	1.06

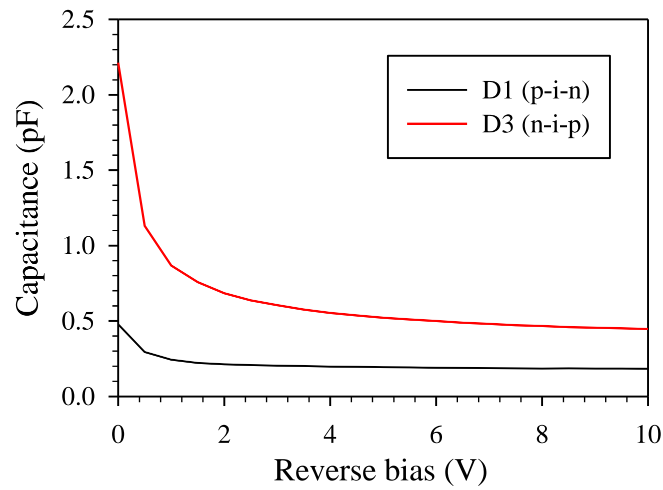

Figure 6-9 Capacitance-Voltage curve of APD D1 and D3 from on-wafer measurement at 77 K.

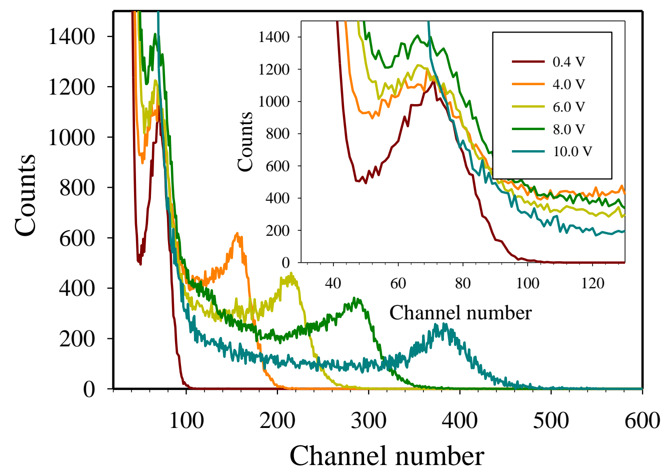

Figure 6-10 Spectra in channel numbers collected using APD D3 cooled to 77 K, at reverse bias voltages from 0.4 to 10 V. Inset: same data from channels 30 to 130.

X-ray spectra were obtained from APD D3 using the same setup and conditions used for APD D1 and D2, as shown in Figure 6-10. The resultant *FWHM* versus reverse bias data are included in Figure 6-11 and they are clearly larger than those from APD D1 for all reverse bias voltages. This is due to APD D3 producing a lower avalanche gain than APD D1 for a given reverse bias voltage (as shown in Figure 6-12), which were deduced from X-ray spectra.

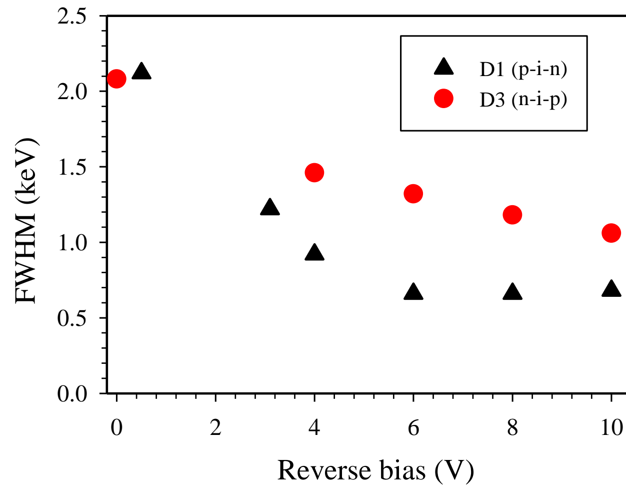

Figure 6-11 Energy resolution (FWHM) at different bias voltages from the APDs D1 (triangle) and D3 (circle).

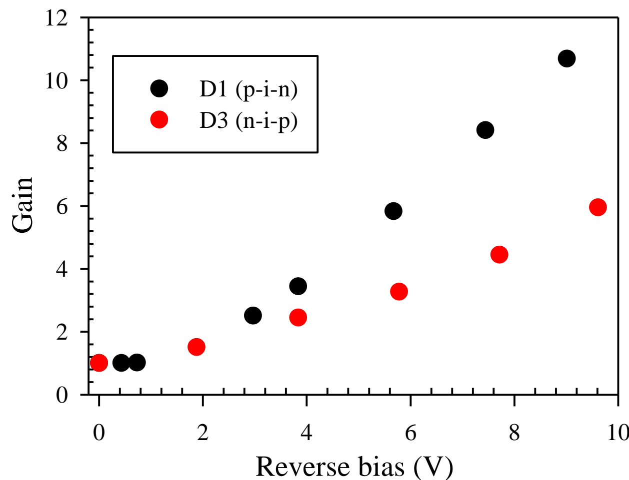

Figure 6-12 Avalanche gain deduced from X-ray spectra of the APD D1 (black) and D3 (red) structures.

Despite the identical i-InAs layer, their avalanche gains for a given reverse bias do differ, owing to different depletion widths. The avalanche gain for APD D1 is found to be ~ 5.8 at 6 V, which gives the smallest *FWHM* in Figure 6-11.

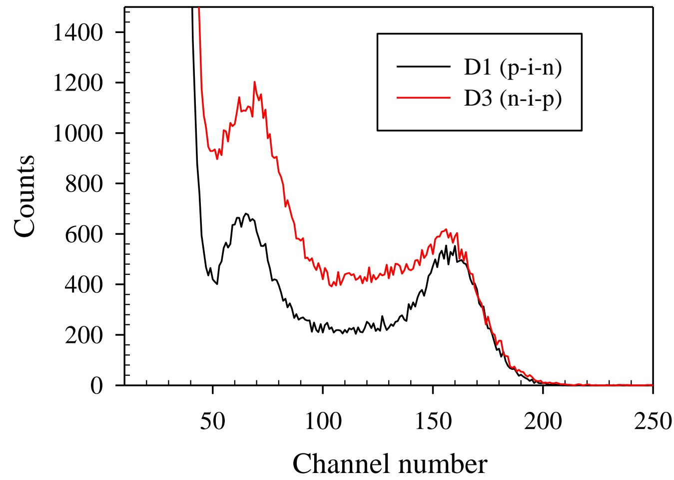

Figure 6-13 Spectra from APD D1 (black) and D3 (red) at 77 K reverse-biased at 3.1 and 4.0 V, respectively.

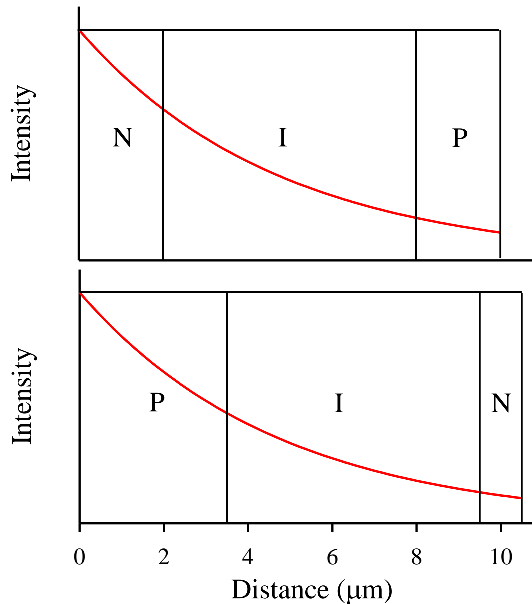

Figure 6-14 Comparison of the absorption profile in InAs APD D3 (top) and D1 (bottom). The red curve following equation $I_0 \exp(-\varphi x)$, where I_0 is the initial intensity of the incident X-ray photons, φ is the attenuation coefficient and x is the distance.

With the knowledge of M, it is then possible to ensure similar avalanche gains (~ 3) for APD D1 and D3 by selecting the appropriate reverse bias conditions (3.1 and 4.0 V, respectively), as shown in the spectra plotted in channel numbers in Figure 6-13. Both APD D1 and D3 exhibits energy peaks around channel 153. Due to a larger optically sensitive area in APD D3 than D1, the data for the former showed higher counts for all channel numbers. Nonetheless, the APD D1 exhibits (1) better peak-to-valley ratio for the peak related to M_e (X-ray absorption in the InAs p-layer) and (2) significantly reduced

magnitude for the peak related to M_h (X-ray absorption in the InAs n-layer), compared to APD D3. These improvements result from better APD design in D1, because less photon absorption now takes place in the i- and n-layer in the p-i-n structure compared with p-layer, as depicted in Figure 6-14.

6.6 Summary

InAs APDs with a p-i-n structure have been fabricated and demonstrated to detect soft X-rays. An energy resolution as small as 401 eV *FWHM* at 5.9 keV (with an avalanche gain of 11) has been achieved, significantly smaller than previously reported value (950 eV). This is mainly due to their higher avalanche gain which greatly improved the signal-to-noise ratio and energy resolution. A comparison of InAs APDs with p-i-n and n-i-p structures experimentally confirmed that InAs APD with p-i-n structure has better peak-to-valley ratio for M_e peak and lower amplitude for M_h peak, which result from less dominant photon absorption in i- and n-layer compared to the p-layer in the p-i-n structure.

Although the InAs APD with p-i-n structure shows significantly improved X-ray performances, the measured energy resolution is still much larger than the Fano-limited energy resolution. Noise analysis revealed that the energy resolution achieved in this work was largely limited by the APD leakage current and measurement system noise. Hence further improvement should focus on reducing electronic noise and leakage current of the diode. In addition, more APD-specific modifications such as minimising X-ray photon absorption within the InAs avalanche layer are required.

6.7 References

[1] P. A. Russell and R. James, "Determination of Toxic Elements in Liquid Hazardous Waste Using Hogh-resolution Energy-dispersive X-ray Fluorescence Spectrometry," *Journal of Analytical Atomic Spectrometry,* vol. 12, pp. 25-32, 1997.

[2] F. L. Melquiades and C. R. Appoloni, "Application of XRF and field portable XRF for environmental analysis," *Journal of Radioanalytical and Nuclear Chemistry,* vol. 262, pp. 533-541, 2004.

[3] J. Börjesson and S. Mattsson, "Medical applications of X-ray fluorescence for trace element research," *Powder Diffraction,* vol. 22, pp. 130-137, 2007.

[4] P. T. Palmer, R. Jacobs, P. E. Baker, K. Ferguson, and S. Webber, "Use of Field-Portable XRF Analyzers for Rapid Screening of Toxic Elements in FDA-Regulated Products," *Journal of Agricultural and Food Chemistry,* vol. 57, pp. 2605-2613, 2009.

[5] Amptek, *xr-100sdd-silicon-drift-detector*. Available: http://www.amptek.com/products/xr-100sdd-silicon-drift-detector/

[6] M. N. Mazziotta, "Electron–hole pair creation energy and Fano factor temperature dependence in silicon," *Nuclear Instruments and Methods in Physics Research Section A: Accelerators, Spectrometers, Detectors and Associated Equipment,* vol. 584, pp. 436-439, 2008.

[7] Ioffe Institute, " *Indium Antomonide*." Available: http://www.ioffe.rssi.ru/SVA/NSM/Semicond/InSb/

[8] Ioffe Institute, "*Indium Arsenide*." Available: http://www.ioffe.ru/SVA/NSM/Semicond/InAs/

[9] S. Adachi, "*Properties of Group-IV, III-V and II-VI Semiconductors,*" John Wiley & Sons, 2005.

[10] I. Kanno, S. Hishiki, O. Sugiura, R. Xiang, T. Nakamura, and M. Katagiri, "InSb cryogenic radiation detectors," *Nuclear Instruments and Methods in Physics Research Section A: Accelerators, Spectrometers, Detectors and Associated Equipment,* vol. 568, pp. 416-420, 2006.

[11] Y. Sato, Y. Morita, T. Harai, and I. Kanno, "Photopeak detection by an InSb radiation detector made of liquid phase epitaxially grown crystals," *Nuclear Instruments and Methods in Physics Research Section A: Accelerators, Spectrometers, Detectors and Associated Equipment,* vol. 621, pp. 383-386.

[12] Y. Sato, Y. Morita, and I. Kanno, "Performance estimation of InSb compound semiconductor detectors as a function of active area using alpha particles," *Nuclear Instruments and Methods in Physics Research Section A: Accelerators, Spectrometers, Detectors and Associated Equipment,* vol. 737, pp. 1-4, 2014.

[13] A. Säynätjoki, P. Kostamo, J. Sormunen, J. Riikonen, A. Lankinen, H. Lipsanen*, et al.*, "InAs pixel matrix detectors fabricated by diffusion of Zn in a metal-organic vapour-phase epitaxy reactor," *Nuclear Instruments and Methods in Physics Research Section A: Accelerators, Spectrometers, Detectors and Associated Equipment,* vol. 563, pp. 24-26, 2006.

[14] Y. Yatsu, Y. Kuramoto, J. Kataoka, J. Kotoku, T. Saito, T. Ikagawa*, et al.*, "Study of avalanche photodiodes for soft X-ray detection below 20 keV," *Nuclear Instruments and Methods in Physics Research Section A: Accelerators, Spectrometers, Detectors and Associated Equipment,* vol. 564, pp. 134-143, 2006.

[15] J. E. Lees, A. M. Barnett, D. J. Bassford, J. S. Ng, C. H. Tan, N. Babazadeh*, et al.*, "Development of high temperature AlGaAs soft X-ray photon counting detectors," *Journal of Instrumentation,* vol. 6, p. C12007, 2011.

[16] R. B. Gomes, C. H. Tan, X. Meng, J. P. R. David, and J. S. Ng, "GaAs/$Al_{0.8}Ga_{0.2}As$ avalanche photodiodes for soft X-ray spectroscopy," *Journal of Instrumentation,* vol. 9, p. P03014, 2014.

[17] C. H. Tan, R. B. Gomes, J. P. R. David, A. M. Barnett, D. J. Bassford, J. E. Lees*, et al.*, "Avalanche Gain and Energy Resolution of Semiconductor X-ray Detectors," *Electron Devices, IEEE Transactions on,* vol. 58, pp. 1696-1701, 2011.

[18] R. B. Gomes, C. H. Tan, P. J. Ker, J. P. R. David, and J. S. Ng, "InAs avalanche photodiodes for X-ray detection," *Journal of Instrumentation,* vol. 6, p. P12005, 2011.

[19] A. R. J. Marshall, C. H. Tan, M. J. Steer, and J. P. R. David, "Electron dominated impact ionization and avalanche gain characteristics in InAs photodiodes," *Applied Physics Letters,* vol. 93, p. 111107, 2008.

[20] P. J. Ker, A. R. J. Marshall, A. B. Krysa, J. P. R. David, and T. Chee Hing, "Temperature Dependence of Leakage Current in InAs Avalanche Photodiodes," *Quantum Electronics, IEEE Journal of,* vol. 47, pp. 1123-1128, 2011.

7 GaAs mesa diodes for X-ray photon counting

7.1 Introduction

GaAs is the most investigated III-V material for direct X-ray detection since it has several promising properties. It has moderately large band gap (1.42 eV) which ensures low dark current at room temperature. Meanwhile, its bandgap is similar to that of Si resulting in a relatively low Fano-limited energy resolution of 129 eV (*FWHM*) at 5.9 keV. This energy resolution is calculated using EHP creation energy and Fano factor from [1]. In addition GaAs has high attenuation coefficients, which offers high detection efficiency, due to its high atomic number (Ga = 31 and As = 33) and crystal density (5.3176 g/cm^3).

Simulation [2] and experimental results [3, 4] have shown that as X-ray detectors, well-designed APDs could improve the signal-to-noise ratio and energy resolution with little added noise from avalanche gain fluctuation. The improvement originates from the APD's avalanche gain. In order to minimise the noise from avalanche gain, pure injection of carrier with higher impact ionisation coefficient is required. This can be achieved by utilising SAMAPD structure.

A GaAs-based SAMAPD for X-ray detection uses a GaAs absorption layer and a wide bandgap avalanche layer. Several wide bandgap semiconductor alloys with well-characterised impact ionisation properties, such as AlGaAs [5, 6], InGaP [7] and AlInP [8], can be grown lattice matched to GaAs. GaAs is chosen as the absorption layer because it has higher attenuation coefficient than its lattice-matched materials to achieve higher detection efficiency. In addition its narrower bandgap (compared with avalanche layer) could result in lower Fano noise. For the avalanche layer, wide bandgap materials are preferred since they enables very thin structure which gives better X-ray energy resolution and lower excess noise, while maintaining acceptably low tunnelling current.

Results in [4] have shown that the X-ray performances of GaAs/AlGaAs SAMAPD is limited by the thin absorption layer (i.e. lower detection efficiency, higher capacitance and unwanted secondary peak). Prior to fabricating a SAMAPD with thicker GaAs absorption region it is necessary to optimise the dark current characteristic of thick GaAs diodes first. Moreover, in X-ray imaging arrays with a mesa structure for the pixel, part

or all of the thick undoped GaAs absorption layer between pixels must be etched away, leading to a large surface area that will likely cause significant leakage current. Large variation in the leakage current from pixel to pixel is also highly undesirable as it leads to poor image quality or requires extensive signal processing. Hence it is vital to optimise the fabrication procedures to minimise (i) surface leakage current of thick GaAs mesa diodes, and (ii) variation in leakage current from diode to diode. These are the main contribution of this work, whose application lies in portable medical X-ray detectors [9].

The leakage currents of GaAs X-ray diodes with mesa structures have been reported [10-14]. Although [10] mentioned that etch depth greatly influence the magnitude of leakage current of diodes, very limited information on the wet chemical etchants (type and solution ratio) or dry etching gases (gases' flow rates and sample's temperature) used in etching their GaAs diodes was given in [10-14]. There is no evidence in [10-14] that their GaAs diodes exhibited bulk-only leakage currents.

The very thick (>100 μm) epitaxially grown GaAs p-i-n diodes of [10] and [11] were produced using wet chemical partial etching without passivation for the mesa. They exhibited dark current density of between 300 nA/cm^2 to 500 μA/cm^2. Slightly lower dark current density at 100 nA/cm^2 was achieved in [13]. Later, Kostamo et al. fabricated a GaAs p-i-n diode array using dry etching and passivated the etched diodes with dielectric materials, which yielded dark current density between 40 and 400 mA/cm^2 [12]. These values are much higher than the dark current density of 5.6 nA/cm^2 reported by Erd et al. [14], whose array consisted of 32×32 GaAs p-i-n diodes with partially-etched mesa (p layer removed between pixels) and guard rings.

In this chapter, the influence of wet chemical etchant solutions and etch depths on the dark currents of GaAs diodes are investigated and discussed. The X-ray response of the fabricated diodes from a ^{55}Fe source is also presented.

7.2 Device structures

The GaAs homojunction p-i-n wafer was grown on a 3-inch n-type conducting GaAs substrate (350 μm thick) by metal organic chemical vapour deposition (MOCVD) by wafer grower Dr. Ben Stevens. The structure, as summarised in Table 7-1, consists of a

510 nm highly doped p^+ GaAs layer, a 7 µm intrinsic layer and a 1 µm n^+ GaAs layer. The p- and n-type dopants used were C and Si respectively.

A series of five samples, namely samples A, B, C, D, and E, was fabricated from the wafer (carried out by other group members). First, Ti/Au (20/200 nm) were deposited onto the samples, which were then annealed in a rapid thermal annealer at 420 °C for 60 s to form ohmic p- and n-contacts. Chemical etching was then used to create circular mesas with diameters, *d*, of 400, 200, 100 and 50 µm. The five samples differ in the chemical etchant used and/or the etch depth (as measured from the top of the wafer), as summarised in Table 7-2. No surface passivation was used in the samples, in order to avoid possible variation in leakage currents due to the passivation material/process used, which will unnecessarily complicate analyses of leakage currents. Surface passivation optimisation for thick mesa is beyond the scope of this work.

Table 7-1 Structure details of the GaAs p-i-n wafer.

Material	Thickness (nm)	Type	Doping density (cm^{-3})
GaAs	10	p^+ (C)	1×10^{19}
GaAs	500	p^+ (C)	2×10^{18}
GaAs	7000	i	undoped
GaAs	1000	n^+ (Si)	2×10^{18}
GaAs substrate	---	n^+	---

Table 7-2 Summary of the five samples.

<table>
<tr><th rowspan="2">Sample</th><th rowspan="2">Etch Depth (nm)</th><th rowspan="2">Remarks</th><th colspan="2">Mean leakage current density (A/cm^2)</th><th>Median of leakage current density (A/cm^2)</th></tr>
<tr><th>d = 400 µm</th><th>d = 200 µm</th><th>All diameters</th></tr>
<tr><td>A</td><td>8300</td><td>Fully etched</td><td>2×10^{-4}</td><td>2×10^{-4}</td><td>2×10^{-4}</td></tr>
<tr><td>B</td><td>8300</td><td>Fully etched</td><td>4×10^{-7}</td><td>5×10^{-3}</td><td>1×10^{-7}</td></tr>
<tr><td>C</td><td>1000</td><td rowspan="3">Partially etched</td><td>4×10^{-8}</td><td>2×10^{-7}</td><td>1×10^{-7}</td></tr>
<tr><td>D</td><td>2000</td><td>2×10^{-8}</td><td>9×10^{-8}</td><td>6×10^{-8}</td></tr>
<tr><td>E</td><td>2500</td><td>8×10^{-8}</td><td>5×10^{-7}</td><td>2×10^{-7}</td></tr>
</table>

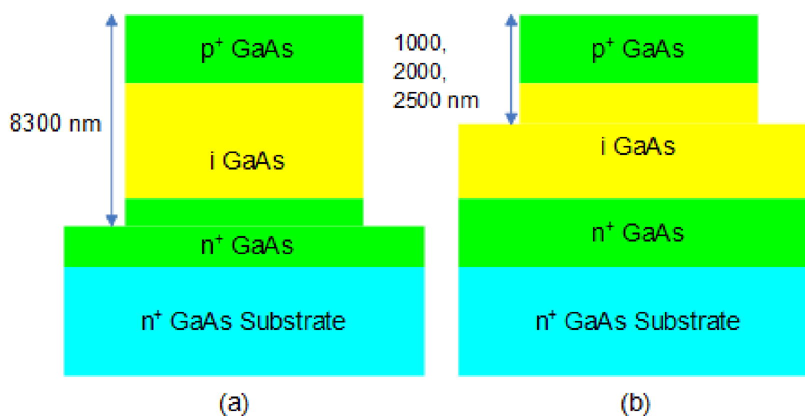

Figure 7-1 GaAs p-i-n diodes with (a) fully, or (b) partially etched circular mesas.

While the mesas in all samples were created using a solution of phosphoric acid : hydrogen peroxide : deionised water (H_3PO_4:H_2O_2:H_2O with ratio of 1:1:1) to achieve the intended etch depths, samples B to E had an additional finishing etch using a solution of sulphuric acid : hydrogen peroxide : deionised water (H_2SO_4: H_2O_2:H_2O with ratio of 1:8:80) for 10 s. Diodes in samples A and B have been fully etched and diodes in sample C, D, and E have been partially etched, as shown in Figure 7-1(a) and Figure 7-1(b), respectively. No substrate removal was carried out.

The sulphuric acid-based finishing etch was included in this study because it was found to improve reverse leakage currents of mesa diodes made of InAs [15]. Note that relying on sulphuric acid-based solution for deep etching is generally avoided as it is known to produce anisotropic etch profiles [16], which affected the circular geometry (to avoid surface leakage current and premature edge breakdown) in the diodes in preliminary etching trials. The ratios for the phosphoric acid-based etchant were chosen to achieve a sufficiently high yet controllable etch rate, following etching trials with a few other ratios.

On-wafer measurements of Current-Voltage (I-V) and Capacitance-Voltage (C-V) characteristics were performed to select promising devices to be packaged for subsequent X-ray measurements. An I-V setup with a Keithley 236 source-measure-unit was used to measure leakage currents ranging from 0.1 pA to 10 mA. The samples were measured at room temperature and in a dark environment to minimise photocurrent generated by stray light. Most of the I-V data were obtained from $d = 200$ and 400 μm diodes because these sizes are more relevant to the targeted application. C–V measurements were carried out

using a HP 4275A Multi- Frequency LCR Meter with a sinusoidal test signal of 60 mV rms magnitude and 1 MHz frequency. The data allow determination of the minimum reverse bias required to fully deplete the i-GaAs layer.

7.3 Results

7.3.1 C-V results

Typical C-V data for d = 400 μm diodes are shown in Figure 7-2(a) which also includes the depletion width versus V deduced from the data. Very similar C-V data for same-sized diodes from the different samples, when V > 10 V, have been found. For example, at reverse bias of 15 V, capacitance values of 400 μm diameter diodes were between 1.99 and 2.15 pF, within the tolerance of the measurement setup. This similarity indicates negligible unwanted lateral depletion in the diodes and hence complete isolation of the diodes.

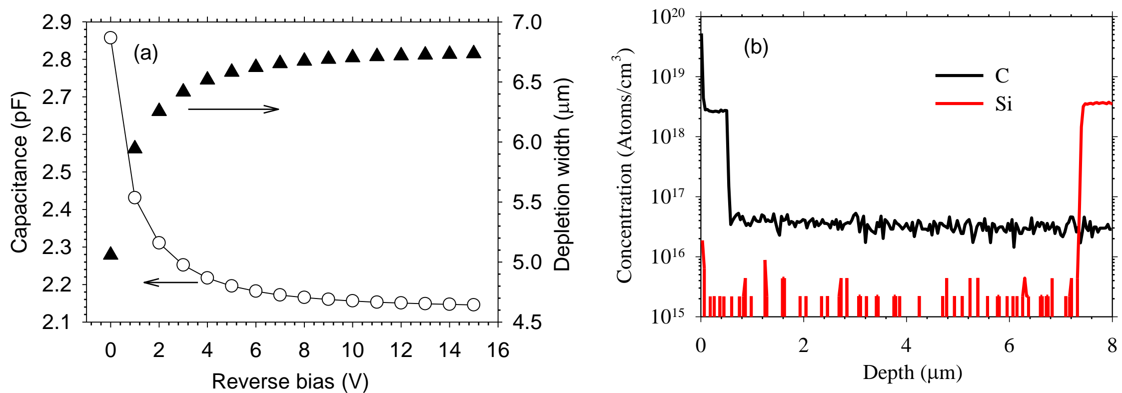

Figure 7-2 (a) Typical C-V data (right axis, circles) and deduced depletion width (right axis, triangles) of a d = 400 μm p-i-n diodes. (b) Secondary Ion Mass Spectroscopy data showing the p (carbon) and n (silicon) doping profiles of the GaAs p-i-n wafer.

Observing Figure 7-2(a), analyses of the C-V data also revealed that the i-GaAs layer thickness is ~ 6.7 μm, slightly thinner than the intended value of 7.0 μm. The deviation was confirmed by data from Secondary Ion Mass Spectroscopy, as shown in Figure 7-2(b), carried out elsewhere on the wafer. The thinner than intended i-GaAs layer is likely to be due to a combination of slight uncertainty in growth rate and dopant diffusion from the highly-doped p- or n-layer into the i-layer, which had taken place during the epitaxial growth. Note that as the instrument background of this measurement is high for

carbon (~ 2×10^{16} atom/cm^3), exact extent of carbon diffusion from the p-layer into the i-layer could not be accurately determined.

7.3.2 Dark current distribution

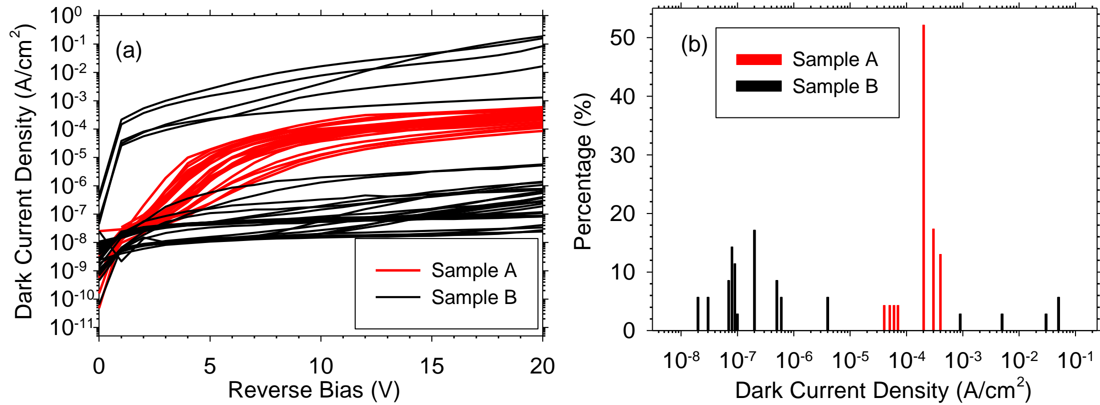

Figure 7-3 (a) Dark current density versus reverse bias, and (b) distribution of dark current density at 15 V for samples A and B, which have fully etched mesas. There were 23 and 12 diodes with diameters of 200 μm and 400 μm diodes, respectively.

To observe if the finishing etch had any noticeable effect on the leakage current, leakage current density of the two samples with fully etched mesas are compared in Figure 7-3(a). Data of 35 diodes (23 of d = 200 μm and 12 of d = 400 μm) are shown for each sample. Mean dark current values for diodes with d = 200 or 400 μm are also shown in Table 7-2. It has been found that sample A exhibited moderately uniform but high leakage current density, whereas sample B generally had lower leakage current density (10 to 100 nA/cm^2) although some diodes were very poor (1 to 10 mA/cm^2). In Figure 7-3(b), the distribution of leakage current density at 15 V for samples A and B are compared. Although sample B had a wider distribution than sample A, ~ 46 % of the diodes tested in sample B had leakage current density < 0.1 μA/cm^2, with some having current densities as low as 20 nA/cm^2. Hence the finishing etch appears to reduce leakage currents in diodes with fully etched mesas. Note that as the current does not scale with diode area, the measured current was dominated by surface leakage current component.

Since samples C, D, and E all had a finishing etch for their partially-etched mesas with different etch depths, they can be studied to observe effects of etch depth on the leakage current density and its distribution. Figure 7-4(a) and Figure 7-4(b) compare their leakage current densities, and distributions of leakage current, based on data of 12 diodes

(8 of d = 200 µm and 4 of d = 400 µm) from each sample. Mean dark current values for diodes with d = 200 or 400 µm are also shown in Table 7-2. Among these three samples, sample D exhibited the lowest leakage current densities, with 75% of the diodes tested having dark current density < 100 nA/cm^2 and a very low mean dark current density of 20 nA/cm^2 for d = 400 µm diodes. This compares favourably to mean leakage current densities of samples C and E, at 40 and 80 nA/cm2, respectively (for d = 400 µm diodes).

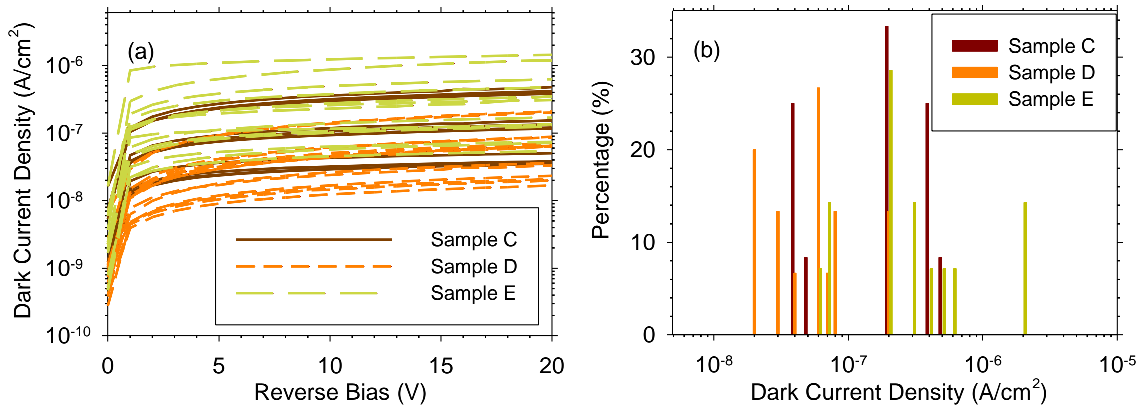

Figure 7-4 (a) Dark current density versus reverse bias, and (b) distribution of dark current density at 15 V for samples C, D, and E, which have partially etched mesas. There were 8 and 4 diodes with diameters of 200 µm and 400 µm diodes, respectively.

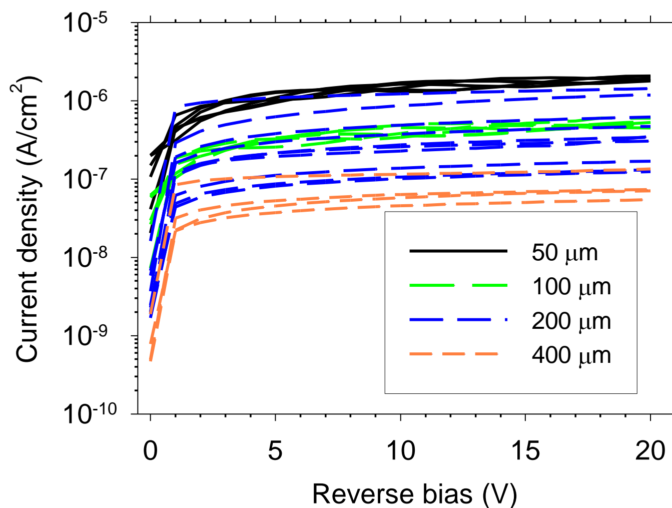

Figure 7-5 Dark current density versus reverse bias for 6, 6, 8, and 4 diodes with diameters of 50, 100, 200, and 400 µm, respectively, from sample E.

For a given sample, comparisons of leakage current density from different sized diodes were made and the data from sample E are shown as an example in Figure 7-5. As the diode's diameter and hence junction area decreased, the leakage current density

increased, indicating that sidewall-related leakage current became increasingly significant compared to the bulk-related leakage current.

Results from diodes with fully etched mesas showed that using only a solution H_3PO_4: H_2O_2: H_2O for etching produces high surface leakage currents in the resultant diodes. Adding a finishing etch using a solution of H_2SO_4: H_2O_2: H_2O can substantially lower the surface leakage currents although the uniformity is still not satisfactory. The variation of dark currents of fully etched diodes on sample B is undesirable for a detector array since it would lead to a large proportion of non-useable pixels. This variation may be caused by variation in surface states on the sidewalls of the mesas, which may be reduced if mesa passivation optimised for GaAs X-ray diodes is available.

The partially etched diodes suffer from this problem at a much lower extent, because the mesa sidewalls are much shorter, resulting in significantly smaller exposed area on the mesa sidewalls. The mean dark current density of sample D at 20 nA/cm^2 (for d = 400 μm diodes) is much lower than those from refs [10-13], but is slightly higher than one of the lowest dark current densities in the literature, 5.6 nA/cm^2 at 50 V at room temperature [14]. The very low dark current density in [14] might be due to the use of guard rings, which can help to suppress surface leakage currents. Nevertheless these results demonstrated that, by adopting appropriate chemical etchants (H_3PO_4: H_2O_2: H_2O followed by H_2SO_4: H_2O_2: H_2O) and etch depth, low leakage currents with good uniformity can be achieved for progress towards detector array.

Although each of the three samples with partially etched diodes show reasonably uniform dark currents, the mean dark currents from the three samples do differ in magnitude. While this observation is consistent with previous works [10-12], there has been no discussion on this in the literature. Hence it is worthwhile analysing the data for partially etched diodes further. Sample C had an etch depth of 1000 nm for a wafer designed to have 510 nm of p-type layer. This would have removed all p-type material between the diodes, thus achieving good level of isolation between the diodes. However, a variation in the etch depth across the sample and dopant diffusion from the p-layer into the i-layer may mean having conducting path along some remaining thin p-type material between the diodes. This will compromise isolation between the diodes and cause additional leakage currents. Therefore a more reliable etch depth would be one that is deeper than the p-type layer thickness by some margins.

For sample E, its higher leakage current density (compared to that of sample D) is probably due to the advantage of reduced surface damage in partially etch diode being lost as the etch depth increases to 2500 nm.

7.3.3 X-ray spectrum

For preliminary evaluation of the diodes' performance when imaging high energy X-ray photons, packaged GaAs p-i-n diodes were individually tested with a ^{55}Fe source. The measurement was carried out using the setup described in section 3.5. The shaping time constant was 2 μs. The system was kept at room temperature.

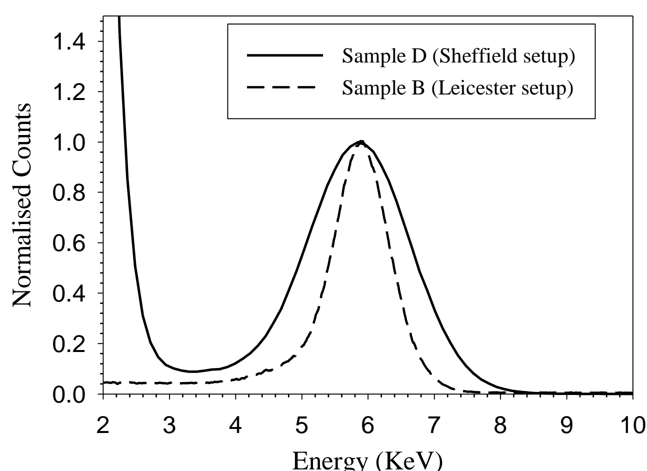

Figure 7-6 A ^{55}Fe X-ray spectrum accumulated with a 400 μm diameter diode from sample D is shown in solid line. Spectrum from a 400 μm diameter diode from sample B obtained using setup in Leicester University is shown in dash line.

Figure 7-6 shows a ^{55}Fe X-ray spectrum accumulated with a 400 μm diameter diode from sample D. The diode was reverse biased at 15 V (depletion width of 6.7 μm), to maintain a low leakage current of 0.95 pA. Using Beer-Lambert Law and assuming that the active layer was limited to the i-layer of the device, it was calculated that the probability of photoelectric interactions taking place within the depleted region (width = 6.7 μm) of the diode at 5.9 keV is 42 %, as shown in Figure 7-7. The spectral resolution, as given by the *FWHM* of the combined 5.9 keV and 6.49 keV peaks is 1.84 keV. A diode with the same size (400 μm diameter) and similar dark current has been tested using a setup in Leicester University. The spectrum, also plotted in Figure 7-6, shows an energy resolution of 1 keV. This better *FWHM* is mainly due to the lower system noise in the setup of Leicester University (~ 800 eV), compared to the ~ 1.1 keV for the Sheffield setup (see Figure 6-7).

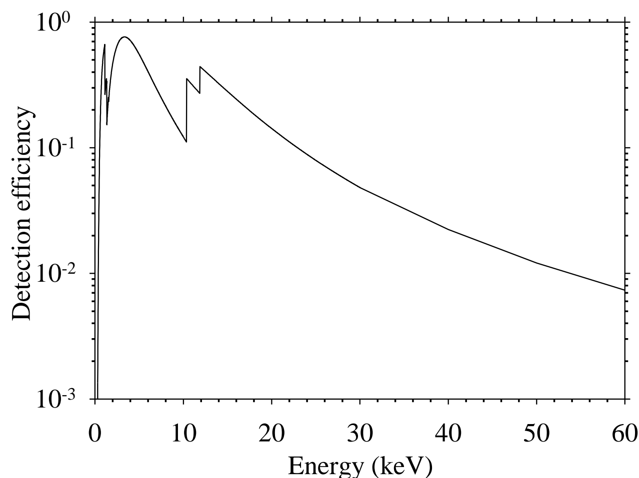

Figure 7-7 Calculated probability of photoelectric interactions taking place within the depleted region (width = 6.7 μm) of the diode versus X-ray photon energy.

In this X-ray measurement, the measured *FWHM* is far from the Fano limited case of 129 eV at 5.9 keV at room temperature and the best experimental reports (266 eV *FWHM* at 5.9 keV [17]). The noise beyond the Fano limit reported here is due to a combination of electronic noise (including parallel white, series white, dielectric, and 1/f noise) from both the preamplifier [18] and detector, and also possibly charge trapping noise [19]. Full shaping time noise analysis of these noise sources and the contributions to the achievable energy resolution is planned for future work. If the reported photodiodes are to be practical options for use in high energy resolution X-ray spectroscopy in the future, the achievable energy resolution must be improved by reducing these noise contributions. However, the detectors reported here are part of early development for imaging arrays, where the energy resolution requirements are more modest.

7.4 Summary

GaAs p-i-n mesa diodes have been fabricated using different wet chemical etching solutions and etch depths. It has been shown that the surface leakage current of diodes with mesa structures can be reduced by adopting appropriate chemical etchants and partially etched mesa. Partially etched diodes with different etch depths have also been studied. The best partially etched sample which has etch depth of 2000 nm showed uniformly low dark currents, with a low mean value of 20 nA/cm^2.

The fabricated GaAs diodes have been characterised using a ^{55}Fe radioisotope source. The presented X-ray results show that the devices reported are capable of photon

counting soft X-ray spectroscopy with a 1 keV spectral resolution at room temperature. Further improvements in the noise performance of the X-ray spectroscopy setup used in this work are required.

7.5 References

[1] G. Bertuccio and D. Maiocchi, "Electron-hole pair generation energy in gallium arsenide by x and γ photons," *Journal of Applied Physics,* vol. 92, pp. 1248-1255, 2002.

[2] C. H. Tan, R. B. Gomes, J. P. R. David, A. M. Barnett, D. J. Bassford, J. E. Lees*, et al.*, "Avalanche Gain and Energy Resolution of Semiconductor X-ray Detectors," *Electron Devices, IEEE Transactions on,* vol. 58, pp. 1696-1701, 2011.

[3] R. B. Gomes, C. H. Tan, P. J. Ker, J. P. R. David, and J. S. Ng, "InAs avalanche photodiodes for X-ray detection," *Journal of Instrumentation,* vol. 6, p. P12005, 2011.

[4] R. B. Gomes, C. H. Tan, X. Meng, J. P. R. David, and J. S. Ng, "GaAs/$Al_{0.8}Ga_{0.2}As$ avalanche photodiodes for soft X-ray spectroscopy," *Journal of Instrumentation,* vol. 9, p. P03014, 2014.

[5] C. H. Tan, J. P. R. David, S. A. Plimmer, G. J. Rees, R. C. Tozer, and R. Grey, "Low multiplication noise thin $Al_{0.6}Ga_{0.4}As$ avalanche photodiodes," *Electron Devices, IEEE Transactions on,* vol. 48, pp. 1310-1317, 2001.

[6] B. K. Ng, J. P. R. David, R. C. Tozer, M. Hopkinson, G. Hill, and G. J. Rees, "Excess noise characteristics of $Al_{0.8}Ga_{0.2}As$ avalanche photodiodes," *Photonics Technology Letters, IEEE,* vol. 14, pp. 522-524, 2002.

[7] C. H. Tan, R. Ghin, J. P. R. David, G. J. Rees, and M. Hopkinson, "The effect of dead space on gain and excess noise in $In_{0.48}Ga_{0.52}P$ $p^{+}in^{+}$ diodes," *Semiconductor Science and Technology,* vol. 18, p. 803, 2003.

[8] J. S. L. Ong, J. S. Ng, A. B. Krysa, and J. P. R. David, "Impact Ionization Coefficients in $Al_{0.52}In_{0.48}P$," *Electron Device Letters, IEEE,* vol. 32, pp. 1528-1530, 2011.

[9] E. N. Ardashev, S. A. Gorokhov, M. K. Polkovnikov, I. S. Lobanov, and A. P. Vorobiev, "A portable X-ray apparatus with GaAs linear array," *Nuclear Instruments and Methods in Physics Research Section A: Accelerators, Spectrometers, Detectors and Associated Equipment,* vol. 648, Supplement 1, pp. S8-S11, 2011.

[10] H. Samic, G. C. Sun, V. Donchev, N. X. Nghia, M. Gandouzi, M. Zazoui*, et al.*, "Characterization of thick epitaxial GaAs layers for X-ray detection," *Nuclear Instruments and Methods in Physics Research Section A: Accelerators, Spectrometers, Detectors and Associated Equipment,* vol. 487, pp. 107-112, 2002.

[11] G. C. Sun, M. Lenoir, E. Breelle, H. Samic, J. C. Bourgoin, H. El-Abbassi*, et al.*, "X-ray detector with thick epitaxial GaAs grown by chemical reaction," *Nuclear Science, IEEE Transactions on,* vol. 50, pp. 1036-1038, 2003.

[12] P. Kostamo, S. Nenonen, S. Vähänen, L. Tlustos, C. Fröjdh, M. Campbell*, et al.*, "GaAs Medipix2 hybrid pixel detector," *Nuclear Instruments and Methods in Physics Research Section A: Accelerators, Spectrometers, Detectors and Associated Equipment,* vol. 591, pp. 174-177, 2008.

[13] G. I. Ayzenshtat, V. P. Germogenov, S. M. Guschin, L. S. Okaevich, O. G. Shmakov, O. P. Tolbanov*, et al.*, "X-ray and γ-ray detectors based on GaAs epitaxial structures," *Nuclear Instruments and Methods in Physics Research Section A: Accelerators, Spectrometers, Detectors and Associated Equipment,* vol. 531, pp. 97-102, 2004.

[14] C. Erd, A. Owens, G. Brammertz, M. Bavdaz, A. Peacock, V. Lämsä*, et al.*, "Hard X-ray test and evaluation of a prototype 32×32 pixel gallium–arsenide array," *Nuclear Instruments and Methods*

in Physics Research Section A: Accelerators, Spectrometers, Detectors and Associated Equipment, vol. 487, pp. 78-89, 2002.

[15] A. R. J. Marshall, "The InAs electron avalanche photodiode and the influence of thin avalanche photodiodes on receiver sensitivity," University of Sheffield, 2009.

[16] A. Baca and C. Ashby, "*Fabrication of GaAs Devices*," The Institution of Engineering and Technology, 2005.

[17] A. Owens, M. Bavdaz, A. Peacock, A. Poelaert, H. Andersson, S. Nenonen*, et al.*, "Hard X-ray spectroscopy using small format GaAs arrays," *Nuclear Instruments and Methods in Physics Research Section A: Accelerators, Spectrometers, Detectors and Associated Equipment,* vol. 466, pp. 168-173, 2001.

[18] A. M. Barnett, J. E. Lees, D. J. Bassford, and J. S. Ng, "A varied shaping time noise analysis of $Al_{0.8}Ga_{0.2}As$ and GaAs soft X-ray photodiodes coupled to a low-noise charge sensitive preamplifier," *Nuclear Instruments and Methods in Physics Research Section A: Accelerators, Spectrometers, Detectors and Associated Equipment,* vol. 673, pp. 10-15, 2012.

[19] A. Owens and A. Peacock, "Compound semiconductor radiation detectors," *Nuclear Instruments and Methods in Physics Research Section A: Accelerators, Spectrometers, Detectors and Associated Equipment,* vol. 531, pp. 18-37, 2004.

8 Conclusions and future works

8.1 Conclusions

For most photon counting applications in NIR range, SPADs, a variant of APDs, remain the detector of choice. This is primarily due to the fact that NIR SPADs operate within the temperature range achievable by multi-stage thermoelectric cooler compared to its main competitor, SSPDs, which is normally operated down to several Kelvins. The vast majority of NIR SPADs being used and/or developed have a planar structure similar to those of fibre-optic telecommunication InGaAs/InP APDs, that use an InGaAs absorption layer and an InP multiplication layer. Within the past decade, significant improvements in SPAD design, quenching and readout circuits have been made. Despite these improvements, the performances of the InGaAs/InP SPADs are still largely limited by the material quality. For example, defects in InP layer will result in severe trap-assisted tunnelling and afterpulsing effects, especially at low temperature. However, most of the previous efforts were on the optimisation of electronic circuit to improve the SPAD performances. It is worth considering if other semiconductor materials have greater potential as the avalanche layer of SPADs at 1550 nm wavelength. In this thesis, NIR SPADs using InAlAs, instead of InP, have been designed, fabricated and characterised.

Firstly, an experiment setup for photon counting performance characterisation was established. This setup was used to characterise the InGaAs/InAlAs SPADs described in chapter 4 and another improved one detailed in chapter 5. In chapter 4, mesa structure InGaAs/InAlAs SPADs were designed and fabricated. Linear-mode characterisations, such as I-V, C-V and photocurrent, were performed. Due to better temperature stability of avalanche breakdown in InAlAs, breakdown voltage of a 25 μm diameter SPAD varied by less than 0.2 V over the 30 K temperature range studied, which corresponds to a temperature coefficient of breakdown voltage less than 7 mV/K. When operated in gated mode, the SPAD demonstrated an *SPDE* of 10% and 21% at 290 K and 260 K, respectively. It is worth mentioning that in the temperature range studied the bias voltage has not been adjusted according to temperature change, which is practically impossible for InGaAs/InP SPAD due to their poorer temperature stability. However, the measured *DCR* result was high and hardly reduced when the SPAD was cooled. Estimation of the

electric field profile of the SPAD reveals that electric field in InAlAs layer at the highest total bias voltage is so high that significant BTB tunnelling current is present and this is believed to be the source of the high *DCR*.

In order to achieve lower *DCR* and higher *SPDE*, the design of InGaAs/InAlAs SPAD was modified. In chapter 5, SPADs with thicker avalanche layer and thicker absorption layer (i.e. 1.0 and 1.7 µm compared with 0.2 and 0.6 µm in the previous generation) were fabricated and characterised. With 1.7 µm thick absorption layer, external quantum efficiency of ~ 56% was obtained. The highest measured *SPDE* was 36% which could be further improved by utilising anti-reflection coating. For temperatures ranging from 250 to 294 K, the measured *DCR* was no longer limited by BTB tunnelling current in InAlAs. This was confirmed by activation energy results (~ 0.3 eV) at this temperature range. However, tunnelling-related current remains a problem at very high overbias voltage. This could be solved by further increasing the avalanche layer thickness.

In this thesis, the experimental investigation into InAs X-ray detectors was also presented. Without any avalanche gain, the InAs diodes (with p-i-n structure) show an energy resolution of ~ 2 keV. This poor energy resolution is largely caused by high electronic noise and diode’s high leakage current. As avalanche gain increases, the energy peak shifts to higher channel number giving a better signal-to-noise ratio. The measured *FWHM* decreases with avalanche gain, and the best energy resolution achieved is 401 eV at gain of 11. However, increase of leakage current with bias voltage also leads to higher noise compromising the positive effect of avalanche gain.

A comparison was also made to illustrate the advantages of InAs APDs with p-i-n structure over those with n-i-p structure. Results show that with the same avalanche gain InAs APD with p-i-n structure presents spectrum with better peak-to-valley ratio for M_e peak and lower amplitude for M_h peak. This is due to the less photon absorption in i- and n-layer of the p-i-n structure. Reduction in system noise and diode’s leakage current are necessary for further improvements.

Lastly, optimised fabrication techniques to obtain GaAs mesa p-i-n diodes with uniformly low leakage current for X-ray photon counting is presented. Influence of both different chemical etching solutions and etch depths on diodes’ leakage current were investigated. The leakage current results show that a combination of main etching

solution (H_3PO_4:H_2O_2:H_2O = 1:1:1) and finishing etching solution (H_2SO_4: H_2O_2:H_2O = 1:8:80) can significantly reduce the leakage current. Partially etched diodes with different etch depths have also been studied. The best sample, partially etched sample which has etch depth of 2000 nm, exhibited uniformly low leakage currents, with a low mean value of 20 nA/cm^2. Using the diodes, a room temperature energy resolution of 1 keV *FWHM* at 5.9 keV has been measured. Further improvements in the energy resolution could be achieved by reducing the system noise of the measurement setup.

8.2 Future work

Chapter 5 demonstrated that InGaAs/InAlAs SPADs have better temperature stability than InGaAs/InP SPADs. Their *SPDE* value are approaching the best InGaAs/InP SPADs although the *DCR* is still much higher. Further modifications on the SPAD structure design and characterisation setup (quenching and readout circuits) are needed to further improve the SPAD performances.

It has been shown that high *DCR* from tunnelling-related mechanism is still limiting the SPAD performance, especially at low temperature and high over bias voltage. In order to reduce the tunnelling current, electric field in both avalanche and absorption layer needs to be lowered. Thicker InAlAs layer could further reduce the breakdown electric field hence any field-related carrier generation. *DCR* from InAlAs PIN diodes with different intrinsic layer are worth investigating. This will give valuable insights of the *DCR* contribution from avalanche layer with different thickness. The comparison of their *DCR* should also cover afterpulsing effect, since thicker avalanche layer is expected to suffer from more severe afterpulsing effect [1]. Apart from the thickness of avalanche layer, its background doping also affect the electric field. For instance, for two InAlAs PIN diodes with the same i-layer thickness, the one with higher background doping will have higher peak electric field at breakdown voltage. To reduce the electric field in absorption layer, charge sheet thickness and/or doping need to be increased. Another advantage of keeping electric field in absorption layer low is to lower the field-enhanced generation current which is a main source of dark current especially in an InGaAs layer with high defect density [2, 3].

The quantum efficiency and *SPDE* could be improved by applying anti-reflection coating on the top of mesa diodes. This will be expected to increase the *SPDE* by 30%. Another

approach to increase the *SPDE* is to deposit a layer of gold contact at the bottom of substrate. This gold layer will help increase the photon absorption by reflecting unabsorbed photon back to the absorption layer increasing the *SPDE* [4].

The quenching method used in this work relies on the falling edge of AC bias pulse. This method work is not suitable for applications requiring a long on time (e.g. unknown photon arrival time). Hence future development should focus on incorporating a fast quenching circuit (i.e. CQC [5]) into the existing setup. Following the work described in section 3.4.4, the modified CQC circuit should be used in future SPAD characterisation to achieve fast quenching, accurate AC bias monitoring and better transient cancellation. In addition, the dummy capacitor could even be replaced by a SPAD device (from the same sample piece as the DUT) operated below breakdown voltage to provide better transient cancellation.

Capability in timing characterisation needs to be added to the current setup. I have built a basic timing characterisation setup using a time to amplitude convertor and MCA. However, the preliminary result from devices in section 4.1 obtained using this setup was poor (~ 1ns). Further efforts are required to locate the cause(s) of poor timing resolution and improve the system timing performance.

For the X-ray detection work, although avalanche gain can greatly reduce the effect of electronic noise, the lowest *FWHM* measured was still largely limited by noise from the preamplifier. A full noise analysis (i.e. *FWHM* versus shaping time) is required to assess the noise contribution from different noise components (i.e. noise of the input FET, detector's leakage current and capacitance, capacitance of FET, dielectric noise) [6]. The noise analysis result will give us a useful guide in which noise sources need to be reduced.

InAs APD with p-i-n structure demonstrated a significantly better energy resolution than previous reported results. In order to achieve Fano-limited energy resolution, several research directions are proposed. In term of APD structure, a thicker p^+ layer is necessary to improve the detector's spectral performance. This will reduce the photon absorption in i-layer and n^+-layer which will broaden the signal peak and cause the unity gain peak, respectively. Off course, this method is based on the fact that minority carrier in p^+ layer (electron) has sufficiently long diffusion length [7] to travel to depleted region.

Another area to be investigated is the optimisation of packaging process. Figure 6-2(a) shows that packaged InAs APDs have higher leakage current than the on-wafer device at both room temperature and 77 K, indicating a degradation caused by the packaging process (e.g. epoxy curing and wire bonding). Moreover, in terms of device fabrication, diode's surface leakage current can be potentially mitigated by fabricating planar InAs APDs. This advantage will be more obvious at low temperature since surface leakage of mesa diodes becomes more dominant as temperature decreases. Therefore, X-ray detection with InAs planar APD will aid in improving energy resolution.

Fabrication process of GaAs mesa diode has been optimised leading to diodes with uniformly low dark currents. This enables the fabrication of array format GaAs diodes suitable for X-ray imaging. So linear or two dimensional GaAs detector array should be fabricated and characterised for the development into room temperature portable X-ray imaging array.

8.3 References

[1] F. Acerbi, M. Anti, A. Tosi, and F. Zappa, "Design Criteria for InGaAs/InP Single-Photon Avalanche Diode," *Photonics Journal, IEEE,* vol. 5, pp. 6800209-6800209, 2013.

[2] S. Verghese, J. P. Donnelly, E. K. Duerr, K. A. McIntosh, D. C. Chapman, C. J. Vineis*, et al.*, "Arrays of InP-based Avalanche Photodiodes for Photon Counting," *Selected Topics in Quantum Electronics, IEEE Journal of,* vol. 13, pp. 870-886, 2007.

[3] S. Cova, M. Ghioni, A. Lacaita, C. Samori, and F. Zappa, "Avalanche photodiodes and quenching circuits for single-photon detection," *Applied Optics,* vol. 35, pp. 1956-1976, 1996.

[4] M. A. Itzler, X. Jiang, M. Entwistle, K. Slomkowski, A. Tosi, F. Acerbi*, et al.*, "Advances in InGaAsP-based avalanche diode single photon detectors," *Journal of Modern Optics,* vol. 58, pp. 174-200, 2011.

[5] S. J. Dimler, J. S. Ng, R. C. Tozer, G. J. Rees, and J. P. R. David, "Capacitive Quenching Measurement Circuit for Geiger-Mode Avalanche Photodiodes," *Selected Topics in Quantum Electronics, IEEE Journal of,* vol. 13, pp. 919-925, 2007.

[6] G. Bertuccio, R. Casiraghi, D. Maiocchi, A. Owens, M. Bavdaz, A. Peacock*, et al.*, "Noise analysis of gallium arsenide pixel X-ray detectors coupled to ultra-low noise electronics," *Nuclear Science, IEEE Transactions on,* vol. 50, pp. 723-728, 2003.

[7] M. J. Kane, G. Braithwaite, M. T. Emeny, D. Lee, T. Martin, and D. R. Wright, "Bulk and surface recombination in InAs/AlAs0.16Sb0.84 3.45 μm light emitting diodes," *Applied Physics Letters,* vol. 76, pp. 943-945, 2000.

Appendix A: single photon counting measurement

1. Load the sample and set to the desired temperature.
    - Load the sample into the chamber of Janis probe station. Start evacuating the chamber with the pump and continue pumping until the pressure reaches around 2×10^{-5}.
    - Cool down the sample to desired temperature. Turn on the temperature controller to stabilise the temperature.
2. Aligning the fibre to the SPAD
    - Connect the Agilent 1550 nm CW laser to the multimode fibre of the Janis probe station through a FC/PC to SMA optical adapter.
    - Bias the diode with Keithley 236 SMU and do a DC sweep.
    - Shine the laser on the optical window of the diode and keep adjusting the position of the fibre until maximum photocurrent is obtained.
    - Disconnect the fibre from the CW laser and switch it to the Picosecond pulsed laser.
3. Electrical connections in the setup
    - Connect the Keighley 2400 SMU to the DC input of the Picosecond Bias Tee.
    - Use the "trigger out" signal of Agilent 81101A pulse generator to trigger the Avtech ultra-fast pulser. Attenuate the output of the pulser using a variable electrical attenuator. Adjust the pulse width and amplitude of the AC pulse by checking it on the oscilloscope. Connect the desired AC pulse to the AC input of the bias tee.
    - Connect the DC+AC output of the bias tee to one of the probe arm of which probe tip has probed on the cathode terminal of the SPAD. The other probe arm of which probe tip has probed the anode terminal is fed into the discriminator through a 50 ohms feed-through load termination.
    - The "monitor output" on the discriminator can be connected to the oscilloscope to monitor the input signal of the discriminator. The NIM output signal is fed into the Canberra 512 Dual Timer/Counter to count the number of avalanche pulses.
    - In case that transient pulses due to rising edge of AC pulse are larger than the avalanche pulses, a differential amplifier is needed. A power splitter is

connected to the output of the bias tee. One signal branch goes into the probe station as mentioned above. The other one is connected to a variable dummy capacitor which is used to generate transient pulses used to cancel out those in the diode branch. Signal from diode and dummy capacitor are connected to the "+" and "-" input of the differential amplifier. Output from the differential amplifier is then connected to the discriminator. The following procedures are the same as the case without differential amplifier.

4. Optical connections in the setup
    - Turn on the pulse laser and let it be warmed up for ~ 20 mins.
    - Adjust the pulse width and amplitude of output of the Agilent pulse generator to meet the TTL standard and use it to trigger the PiLas Picosecond pulsed laser. Set the delay time to be around 260 ns. This delay time is the time interval from "trigger out" to "pulse out". Later in the measurement delay time need to be checked since the actual delay time caused by the optical fibre or coaxial cable might not be the same.
    - Attenuate the pulsed laser with the variable Exfo FVA-3100 optical attenuator. Select the desired attenuation to attenuate the laser to single photon level.
5. Dark counting and photon counting
    - Make the lab as dark as possible (e.g. turn off the light, cover all the displays and LEDs).
    - Bias the diode with a DC voltage which is 1 V below the breakdown voltage. Apply an AC voltage with an amplitude lower than 1 V and slowly increase the voltage until avalanche pulses emerges.
    - Reduce the DC voltage to make sure the total bias voltage is lower than the breakdown voltage. Then adjust the threshold voltage on the discriminator to a value just higher than the transient pulses. Then increase the DC voltage back to the original value and start to count the number of avalanche pulse (dark count).
    - Switch the pulsed laser on and measure the total number of avalanche pulse (total count).
    - Adjust the AC voltage to carry out *DCR* and *TCR* measurement at different over bias voltages.
6. Measurement at different temperatures

- Change the setting on temperature controller to heat or cool the sample to desired temperatures and perform the same procedures in step 5.

Appendix B: X-ray spectroscopy measurement

1. Load the radioisotope source and TO-5 header to the dewar
    - Take out the radioisotope source from the shielded box using the handling tong. Place it into the source holder and seal it (high energy source, i.e. ^{241}Am, will need to be covered by lead sheets).
    - Remove the cap of the TO-5 header and clamp it to the cold finger in the chamber. Solder the header to the wires connected to the SMA connector. The detector is around 5mm away from the source.
2. Pump down and cool down the dewar
    - Install the vacuum valve operator (VOM-1) and tighten the gland seal nut.
    - Screw in the valve operator stem into the valve insert (~ 10 turns in clockwise direction) and pull out the insert from the valve.
    - Pump down the system using the rotary pump until the pressure of 10^{-4} Torr is achieved.
    - Pour some liquid nitrogen through a funnel into the dewar. Do not rush to pour liquid nitrogen since the boiling liquid nitrogen may splash and cause frostbite injury. Fill the dewar gradually or lift the funnel to let the gas comes out.
    - Cover the filling port with the cap. Wait for around 25 minutes to let the temperature in the dewar stabilise at 77 K. If the duaration time of your measurement is longer than 2 hours remember to refill the dewar. Keep the cap on the filling port to prevent air and moisture.
3. Connect the SMA connector from the dewar to the detector input of the Amptek preamplifier. Short cable is preferred since longer cable will increase the parasitic capacitance and electronic noise.
4. Connect the bias supply to the bias input of the preamplifier.
5. Connect the energy output of the preamplifier to the input of the shaping amplifier whose output is fed to the MCA which is controlled by a PC. The busy output of the shaping amplifier is connected the BUSY of the MCA for dead time correction.
6. The test input of the preamplifier is used for system test (i.e. noise measurement).
7. MCB properties setting
    - Under the ADC tab, the conversion gain can be entered in powers of 2 (i.e. 1024, 4096). Conversion gain sets the maximum channel number of the spectrum.

Larger conversion gain will give more accurate spectrum at the price of longer accumulation time.

- The upper and lower discriminator are used to set a level of the lowest and highest amplitude pulse to be stored respectively. Lower discrimination level is suggested to set above the noise floor to increase the useful throughput.
- Under the Preset tab, the collection time can be preset by four means namely real time, live time, ROI peak and ROI integral. You need to enable one of them by entering a count number. When the count number reaches the preset value the MCA detector will stop counting automatically. Check the preset limit on the right side of the maestro window whether it shows the value you entered. If none of them is enabled the detector will continue counting until it is manually stopped.

8. Start the acquisition. Adjust the gain on the shaping amplifier to ensure that the desired spectrum area is fully displayed.
9. After the collection of the spectrum is finished pour the remaining liquid nitrogen back into the storage dewar. Turn off the pump and remove the valve operator from the dewar.
10. Calibrate the spectrum.
    - Select a region of interest (ROI) by pressing the left button of the mouse and dragging it to the other side until the rectangular covers the region you are interested in. Right click the mouse and select mark ROI.
    - Place the marker on the ROI. Click Calibrate under the Calculate menu. On the prompt window, type into the energy value corresponding to the peak of the ROI. If warning prompt you need to enter the energy for the marker channel manually.
    - Repeat the above steps to calibrate the second peak. Click destroy calibration to reset the calibration if you need.
    - Enter the unit for the calibrated channels (i.e. keV).
    - If two peaks are entered, a linear calibration will be performed. More than two peaks can be entered to perform a quadratic fitting for more a more accurate calibration.
    - Save the calibrated spectrum in ASCII file (.CHN) format. The calibration data is saved at the end of the file in form of (c, b and a). These three coefficient can

be used to convert the channel number x to energy in keV by using equation ax^2+bx+c.

11. Energy resolution calculation. Plot out the energy spectrum using the saved data. Normalise the maximum count number of the peak you are interested in to one and do a Gaussian fitting to determine the energy resolution.

Appendix C: X-ray noise measurement using test pulser

In the noise measurement, the detector must be connected to the Test input of the preamplifier to include the noise contribution from both its leakage current and capacitance. It can be seen from Figure C.1(a) that connecting the detector broadens the energy peak leading to worse energy resolution.

1. Couple the pulser to the Test input of the A250CF preamplifier through a test capacitor of 0.5 pF.
2. Set up the pulser to generate a square wave with rise/fall time less than 20 ns and proper amplitude (depending on the simulated energy value). Note that *FWHM* of the simulated energy peak is independent with the amplitude of square pulses (i.e. simulated energy). Figure C.1(b) shows that the input square pulses with different amplitudes give the same broadness in channel number (*FWHM* = 14).
3. Connect the preamplifier Energy Output (*E*) to the post amplifier with proper shaping time.
4. Connect the post amplifier output to the MCA input.
5. Obtain the spectrum of two energy peaks formed by two test pulses with different known amplitudes.
6. Calibrate the MCA using the two energy peaks.
7. Export the spectrum data as an ASCII file. The peak resolution can be determined by doing Gaussian fitting to the spectrum data in Sigmaplot.

Example:

To simulate the generated charges by a photon with energy of 60 keV in Si detector, the amplitude of the pulse should be $V = Q/C_{test}$, where Q is the generated charges and C_{test} is the capacitance of the test capacitor.

The generated charges can be calculated as $Q = \frac{60keV}{\varepsilon} q = 2.63 \times 10^{-15} C$, where ε is the EHP creation energy (3.65 keV) in silicon. If the test capacitor has a capacitance of 0.5 pF, the required amplitude of the pulse is 2.63×10^{-15} C/0.5 pF = 5.3 mV.

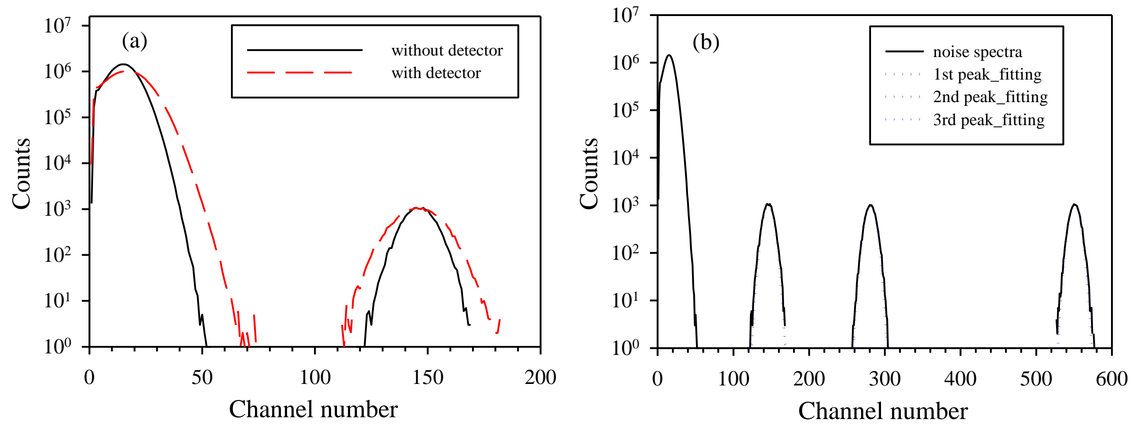

Figure C.1. (a) Comparison of noise spectra obtained with (solid line) and without (dash line) detector. (b) Noise spectra obtained using input signals with different amplitudes (detector not connected).